

Florida Institute of Technology

Scholarship Repository @ Florida Tech

Theses and Dissertations

5-2024

A Statistical Fetch Model for Water Wave Glint Correction Using WorldView-3 Imagery

Amanda Jade Quintanilla

Florida Institute of Technology, aquintanilla2021@my.fit.edu

Follow this and additional works at: <https://repository.fit.edu/etd>



Part of the [Oceanography Commons](#)

Recommended Citation

Quintanilla, Amanda Jade, "A Statistical Fetch Model for Water Wave Glint Correction Using WorldView-3 Imagery" (2024). *Theses and Dissertations*. 1407.

<https://repository.fit.edu/etd/1407>

This Thesis is brought to you for free and open access by Scholarship Repository @ Florida Tech. It has been accepted for inclusion in Theses and Dissertations by an authorized administrator of Scholarship Repository @ Florida Tech. For more information, please contact kheifner@fit.edu.

A Statistical Fetch Model for Water Wave Glint Correction Using WorldView-3 Imagery

by
Amanda Jade Quintanilla

A thesis submitted to the College of Engineering
and Science at
Florida Institute of Technology
in partial fulfillment of the requirements
for the degree of

Master of Science
in
Earth Remote Sensing

Melbourne, Florida
May, 2024

We the undersigned committee hereby approve the attached thesis,
“A Statistical Fetch Model for Water Wave Glint Correction Using WorldView-3
Imagery”

by
Amanda Jade Quintanilla

Charles R. Bostater, Ph.D.
Associate Professor
Ocean Engineering and Marine Science
Major Advisor

Ronnal Reichard, Ph.D.
Professor
Ocean Engineering and Marine Science

Donald Platt, Ph.D.
Associate Professor
Aerospace, Physics, and Space Sciences

Richard B. Aronson, Ph.D.
Professor and Department Head
Ocean Engineering and Marine Science

Abstract

A Statistical Fetch Model for Water Wave Glint Correction Using WorldView-3 Imagery

Author: Amanda Quintanilla

Advisor: Charles R. Bostater, Ph.D.

Sun glint in satellite imagery of the water surface contaminates the upwelling signal received by a detector. Many models exist that attempt to correct for this wave facet effect and phenomena. In this work a model for sun glint correction is created using the comparison of image transects between two nearly simultaneously collected images of the same area, although with differing sensor geometry. One image utilized in this research is almost entirely glint free while the other is contaminated by water wave facet glint. Although many models for removing sun glint exist based on various techniques, none are completely accurate, and there is always a need to improve our understanding of this phenomena and to decontaminate the sun glint pixels. The model developed in this research is based on the statistical properties of the images related to azimuth angles, fetch distances, wind speed and direction, and other factors in attempt to test a new mathematical model for sun glint removal.

Table of Contents

Abstract.....	iii
List of Figures.....	vi
List of Tables.....	xii
List of Symbols.....	xiii
List of Abbreviations.....	xiv
List of Equations.....	xvi
Acknowledgement.....	xviii
Dedication.....	xix
1. Introduction.....	1
1.1 General.....	1
1.2 Sun Glint.....	1
1.3 Research Goals and Outcomes.....	4
2. Background.....	6
2.1 Remote Sensing of Spectral Signatures of Water Bodies.....	6
2.2 Existing Sun Glint Correction Methods.....	11
2.3 Background on Sensor Image Processing and Sensor Geometry.....	19
2.4 WorldView-3 Imagery.....	23
2.5 WorldView-3 Imagery Used for the Research.....	25
2.6 Building a Glint Model.....	34
2.7 Logistic Growth Curve Model for Estimating Sun Glint Reflectance.....	39
3. Methods.....	45
3.1 Processing WV-3 Multispectral Reflectance Imagery in Fetch Limited Waters.....	45
3.2 Creating Image Transects to Build Model.....	47
3.3 Linearization of Logistic Growth Model.....	80
3.4 Parameters for Creating Model.....	82
3.5 Methods for testing model correction accuracy.....	88
3.6 Comparison to Hedley Glint Correction Method.....	90
4. Results.....	98

4.1 Model Parameter Results	98
4.2 Hedley Comparison Results	132
5. Summary and Recommendations	144
5.1 Summary of Work Done	144
5.2 Recommendations	144
References	146
Appendix A	150
Performing Radiometric Calibration on Raw Imagery in ENVI.....	150
Appendix B	157
Performing Nonlinear Regression Using Systat.....	157

List of Figures

Figure 1.1: In this figure, A is due to light scattered in the atmosphere that reaches the detector, B is due to light scattered in the atmosphere that reaches the sea surface and then reflects to the detector (sky glint), C is due to light reflected from whitecaps (bright white foam from breaking waves), D is light from the sun that directly reflects off the sea surface to the detector, and E is light from the sun that is transmitted through the atmosphere and sea surface and then emitted back out towards the detector (Kay 2009).3

Figure 2.1: Five bottom type spectral signatures modeled for a 10-meter depth of pure water. Showing water surface irradiance on the y axis and wavelength on the x axis. Different bottom types can be seen to produce unique characteristics in water surface spectral reflectance signature.....8

Figure 2.2: The geometry of a common push broom scanner from Cao et. Al (Cao 2019).21

Figure 2.3: Possible WorldView-3 collection paths from the DigitalGlobe information sheet on WV-3 (DigitalGlobe, 2017).24

Figure 2.4: Multispectral glint contaminated image in ENVI, using Red (660 nm), Green (545 nm), and Blue (480 nm) bands. Image taken at 16:01:02.5516 UTC on 8/28/2014.27

Figure 2.5: Multispectral glint free image in ENVI, using Red (660 nm), Green (545 nm), and Blue (480 nm) bands. Image taken at 16:02:05.310569 UTC on 8/28/2014. ...28

Figure 2.9: Satellite orbit positioning at the approximate time the glint contaminated image was taken. Image produced using the STK software.29

Figure 2.10: Satellite orbit positioning at the approximate time the non-glint contaminated image was taken. Image produced using the STK software.30

Figure 2.12: Georeferenced WorldView-3 image overlaid to land features on the map of the Melbourne, Florida area with roads using ArcGIS Pro. The extent of the imagery used can be visualized using this georeferenced point of view. Approximate satellite track indicated by red arrow.32

Figure 2.13: Example of reflectance values across the two images along with glint residuals compared for reference. Pixels were taken from the red band (660 nm), from a section of a transect away from the shore on the Indian River Lagoon side of the image.33

Figure 2.14: Shows how sun zenith angle, sun azimuth angle, sensor zenith angle, sensor azimuth angle contribute to glint probability. Water surface slope is influenced by wind and fetch properties (Kay, 2009).35

Figure 2.15: Differential uneven heating of the Earth by incoming sunlight (Nugent, 2022).37

Figure 2.16: Earth winds and cells shown with the effects of rotation (right) and without (left) (Nugent, 2022).	38
Figure 2.17: Logistic growth curves based on the generalized logistic growth curve equation, showing the influence of alpha, beta, and gamma terms (Tsoularis, 2002).	41
Figure 2.18: Logistic growth curves based on the generalized logistic growth curve equation, showing the influence of alpha, beta, and gamma terms. Shows population size by growth rate (Tsoularis, 2002).	42
Figure 3.1: Difference in pixel values when converted from DN to Radiance and Reflectance.	46
Figure 3.2: First transect created to view effects of fetch distance shown by the red line, created using ENVI. Shown using the multispectral glint image using the red (660 nm), green (545 nm), and blue bands (480 nm). Image taken at 16:01:02.5516 UTC on 8/28/2014.	48
Figure 3.3: Starting point of the first transect in the glint free image (left) and the glint contaminated image (right). Transects in each image are taken using the same precise pixel coordinates.	49
Figure 3.4: Transect 1 from the multispectral glint contaminated image as shown in Figure 3.2. Image taken on 8/28/2014 at 16:01:02.5516 UTC using the red band (660 nm). X-axis starting value represents the beginning of transect 1 on the lagoon side shore as seen in Figure 3.3.	50
Figure 3.5: Transect 1 from the multispectral glint contaminated image as shown in Figure 3.2. Image taken on 8/28/2014 at 16:01:02.5516 UTC using the green band (545 nm). X-axis starting value represents the beginning of transect 1 on the lagoon side shore as seen in Figure 3.3.	51
Figure 3.6: Transect 1 from the multispectral glint contaminated image as shown in Figure 3.2. Image taken on 8/28/2014 at 16:01:02.5516 UTC using the blue band (480 nm). X-axis starting value represents the beginning of transect 1 on the lagoon side shore as seen in Figure 3.3.	52
Figure 3.7: Transect 1 from the multispectral glint free image as shown in Figure 3.2. Image taken on 8/28/2014 at 16:02:05.310569 UTC using the red band (660 nm). X-axis starting value represents the beginning of transect 1 on the lagoon side shore as seen in Figure 3.3.	53
Figure 3.8: Transect 1 from the multispectral glint free image as shown in Figure 3.2. Image taken on 8/28/2014 at 16:02:05.310569 UTC using the green band (545 nm). X-axis starting value represents the beginning of transect 1 on the lagoon side shore as seen in Figure 3.3.	54
Figure 3.9: Transect 1 from the multispectral glint free image as shown in Figure 3.2. Image taken on 8/28/2014 at 16:02:05.310569 UTC using the blue band (480 nm). X-axis starting value represents the beginning of transect 1 on the lagoon side shore as seen in Figure 3.3.	55

Figure 3.10: First transect (glint contaminated image) panchromatic band shown by the red line within the box. This image was taken on 8/28/2014 at 16:01:02.5516 UTC with a spectral bandwidth of 450-800 nm on the lagoon side shore.56

Figure 3.11: Starting point of transect 1 on the lagoon side shore in the glint free panchromatic image (left) and glint contaminated panchromatic image (right) as seen in Figure 3.10. A linear visual enhancement was applied to the glint image to better visualize the land and water and compare to the glint free image.57

Figure 3.12: Transect 1 from the panchromatic glint contaminated image as shown in Figure 3.10. Image taken on 8/28/2014 at 16:01:02.5516 UTC. X-axis starting value represents the beginning of transect 1 on the lagoon side shore as seen in Figure 3.11.58

Figure 3.13: Transect 1 from the panchromatic glint free image as shown in Figure 3.10. Image taken on 8/28/2014 at 16:02:05.310569 UTC. X-axis starting value represents the beginning of transect 1 on the lagoon side shore as seen in Figure 3.11.59

Figure 3.14: Transect 2 in the multispectral glint contaminated image shown inside the red box. This image was taken on 8/28/2014 at 16:01:02.5516 UTC, shown using the red (660 nm), green (545 nm), and blue (480 nm) bands.60

Figure 3.15: Transect 2 in the multispectral glint free image shown inside the red box. This image was taken on 8/28/2014 at 16:02:05.310569 UTC, shown using the red (660 nm), green (545 nm), and blue (480 nm) bands.61

Figure 3.16: Transect 2 from the multispectral glint contaminated image as shown in Figure 3.14. Image taken on 8/28/2014 at 16:01:02.5516 UTC using the red band (660 nm). X-axis starting value represents the beginning of transect 2 on the lagoon side shore.62

Figure 3.17: Transect 2 from the multispectral glint contaminated image as shown in Figure 3.14. Image taken on 8/28/2014 at 16:01:02.5516 UTC using the green band (545 nm). X-axis starting value represents the beginning of transect 2 on the lagoon side shore.63

Figure 3.19: Transect 2 from the multispectral glint contaminated image as shown in Figure 3.14. Image taken on 8/28/2014 at 16:01:02.5516 UTC using the blue band (480 nm). X-axis starting value represents the beginning of transect 2 on the lagoon side shore.64

Figure 3.19: Transect 2 from the multispectral glint free image as shown in Figure 3.14. Image taken on 8/28/2014 at 16:02:05.310569 UTC using the red band (660 nm). X-axis starting value represents the beginning of transect 2 on the lagoon side shore.65

Figure 3.20: Transect 2 from the multispectral glint free image as shown in Figure 3.14. Image taken on 8/28/2014 at 16:02:05.310569 UTC using the green band (545 nm). X-axis starting value represents the beginning of transect 2 on the lagoon side shore.66

Figure 3.21: Transect 2 from the multispectral glint free image as shown in Figure 3.14. Image taken on 8/28/2014 at 16:02:05.310569 UTC using the blue band (480 nm). X-axis starting value represents the beginning of transect 2 on the lagoon side shore.	67
Figure 3.22: Transect 2 panchromatic band glint contaminated image transect shown by red box.....	68
Figure 3.23: Transect 2 panchromatic glint free image transect shown by red box.	69
Figure 3.24: Transect 2 from the panchromatic glint contaminated image as shown in Figure 3.22. Image taken on 8/28/2014 at 16:01:02.5516 UTC. X-axis starting value represents the beginning of transect 2 on the lagoon side shore.	70
Figure 3.25: Transect 2 from the panchromatic glint free image as shown in Figure 3.23. Image taken on 8/28/2014 at 16:02:05.310569 UTC. X-axis starting value represents the beginning of transect 2 on the lagoon side shore.	71
Figure 3.26: Transect 3 multispectral glint image shown in the red box.	72
Figure 3.27: Transect 3 multispectral glint-free image shown in the red box.	73
Figure 3.28: Transect 3 from the multispectral glint image as shown in Figure 3.26. Image taken on 8/28/2014 at 16:01:02.5516 UTC. X-axis starting value represents the beginning of transect 3 on the lagoon side shore.	74
Figure 3.29: Transect 3 from the multispectral glint free image as shown in Figure 3.26. Image taken on 8/28/2014 at 16:02:05.310569 UTC. X-axis starting value represents the beginning of transect 3 on the lagoon side shore.	75
Figure 3.30: Transect 3 panchromatic glint image shown in the red box.	76
Figure 3.31: Transect 3 panchromatic non-glint image shown in the red box.....	77
Figure 3.32: Transect 3 from the panchromatic glint image as shown in Figure 3.30. Image taken on 8/28/2014 at 16:01:02.5516 UTC. X-axis starting value represents the beginning of transect 3 on the lagoon side shore.	78
Figure 3.33: Transect 3 from the panchromatic glint image as shown in Figure 3.31. Image taken on 8/28/2014 at 16:02:05.310569 UTC. X-axis starting value represents the beginning of transect 3 on the lagoon side shore.	79
Figure 3.34: Wind speeds and directions for August 28, 2014 at approximately 11:53 am EST (15:53 UTC) from the wunderground historical weather data website. Blue box indicates the hour in which the WorldView-3 imagery was taken.	84
Figure 3.35: Glint contaminated image showing the region of interest used for Hedley correction in the red box.	93
Figure 3.36: Glint free image showing region of interest used for Hedley correction for reference.	94
Figure 3.37: Area within the red boxes of figures 10 and 11 (region of interest) shown for reference. It is evident that this is an area of relatively deeper open water, very homogenous in the glint free image (left) but showing a varying amount of glint in the glint contaminated image (right).	95

Figure 4.1: First transect multispectral blue band residuals (glint image minus non-glint image) linearized. The nonlinear regression estimate model was run using equation 4.1. An estimated value of .978 for c was used; a and r were estimated by the model. This estimated c value was obtained through trial and error.99

Figure 4.2: First transect residual reflectance compared to the modeled residual reflectance created using coefficients estimated from Systat.103

Figure 4.3: First transect glint and non-glint image reflectance compared to the model corrected reflectance values.104

Figure 4.4: Second transect multispectral blue band residuals (glint image minus non-glint image) linearized. The nonlinear regression estimate model was run using equation 4.1. An estimated value of .978 for c was used; a and r were estimated by the model.....106

Figure 4.5: Second transect residual reflectance compared to model predicted residual reflectance values.109

Figure 4.6: Second transect glint and non-glint reflectance compared to the model corrected reflectance values.110

Figure 4.7: Glint image and non-glint image residuals plotted with model predicted residual reflectance values.112

Figure 4.8: Model corrected reflectance values compared to the glint and non-glint reflectance.113

Figure 4.9: Additional transect correction shown compared to glint and non-glint transects.115

Figure 4.10: Additional transect model predicted residual reflectance values of glint and non-glint image compared to the actual values.....116

Figure 4.11: The area of the image used for the region of interest (ROI) subset in the glint image. The region within the red box is shown zoomed in. The ROI is made up of all pixels within the green box.122

Figure 4.12: A side by side comparison of the ROI used for the non-glint image (left), the glint image (middle), and the model corrected image (right).123

Figure 4.13: Location of the transect across ROI used (red line visible below the crosshairs).124

Figure 4.14: ROI visual correction transect reflectances compared to glint and non-glint image transect.....125

Figure 4.15: Random sample of 25 pixels from the ROI selected, showing corrected reflectance value with the glint and non-glint pixels corresponding.128

Figure 4.16: Distributions of reflectance values in the transect through the ROI for both images and the corrected image.131

Figure 4.17: Multispectral region of interest ENVI windows displayed using original reflectance values (left) and Hedley corrected reflectance values (right). A visible difference is not very pronounced.....133

Figure 4.18: A section of the region of interest reflectance values of the original green band (glint contaminated image) and corresponding reflectance values for the Hedley corrected pixels, no scaling factor introduced.....134

Figure 4.19: A section of the region of interest reflectance values of the original red band (glint contaminated image) and corresponding reflectance values for the Hedley corrected pixels, no scaling factor introduced.....135

Figure 4.20: A section of the region of interest reflectance values of the original blue band (glint contaminated image) and corresponding reflectance values for the Hedley corrected pixels, no scaling factor introduced.....136

Figure 4.21: A section of the region of interest reflectance values of the original blue band (glint contaminated image) and corresponding reflectance values for the Hedley corrected pixels, a 100% increase scaling factor introduced.138

Figure 4.22: A section of the region of interest reflectance values of the original green band (glint contaminated image) and corresponding reflectance values for the Hedley corrected pixels, a 100% increase scaling factor introduced.139

Figure 4.23: A section of the region of interest reflectance values of the original red band (glint contaminated image) and corresponding reflectance values for the Hedley corrected pixels, a 100% increase scaling factor introduced.140

Figure 4.24: A section of the region of interest reflectance values of the glint free image (which would be the ideal corrected values) and corresponding reflectance values for the Hedley corrected pixels, a 6000% increase scaling factor introduced.142

List of Tables

Table 2.1: Comparison between all glint correction methods outlined in section 2.2.	19
Table 2.2: Viewing geometry of both images used from WorldView-3 metadata. Differences between the two are present in off nadir viewing angle, in track viewing angle, across track viewing angle, satellite azimuth, and satellite elevation angle.	31
Table 3.1: Possible values that could contribute to glint for consideration when evaluating fit equation coefficients.	86
Table 4.1: Estimated and given coefficient values for the final and most accurate iteration of the estimate model.	100
Table 4.2: Final coefficients determined by examining the fit line and glint reflectance data in Microsoft Excel.	102
Table 4.3: Second transect parameters as estimated by Systat using the nonlinear estimate model tool.	107
Table 4.4: Final coefficients determined by examining the fit line and glint reflectance data in Microsoft Excel for the second transect.	108
Table 4.5: For terms used, $\alpha 1$ refers to the non-glint image sensor azimuth angle and $\alpha 2$ refers to the glint image sensor azimuth angle (ratio).	117
Table 4.6: For terms used, ϑ refers to the wind speed in meters per second, τ refers to the time the wind was blowing in the same direction without changing, δ refers to the wind direction angle, and ω refers to the difference between the sensor azimuth angle and the wind direction angle.	118
Table 4.7: For terms used, $\theta 1$ refers to the in track viewing angle ratio between the glint and non-glint images. $\theta 2$ refers to the across track viewing angle ratio between the glint and non-glint images. $\theta 3$ refers to the off nadir viewing angle ratio between the glint and non-glint images. δ refers to the inverse of the wind direction, estimated (Eastern wind ~ 90 degrees).	119
Table 4.8: Values taken from the blue band of the glint and non-glint images. Based on the arithmetic means, the amount that was corrected on average from the glint transect using the model was 0.084. Subtracting the Non-glint mean from the glint mean yields that 0.155 should have been corrected out. Thus, a 54.19% correction value was calculated (what was removed- glint minus corrected, divided by what should have been removed- glint minus non-glint).	126
Table 4.9: Random pixel reflectance values for glint, non-glint, and the corrected ROIs. Values that are above 100 or negative reflect areas where the model over corrected glint pixels. An average correction percentage of 60.37% when outlier pixels 9, 21, and 24 were removed was calculated.	129
Table 4.10: Statistics calculated for the random sample of 25 pixels from the ROI used. Percent corrected based solely on mean values values, not averaged with every pixel as in Table 4.9.	130

List of Symbols

- α Alpha (constant value for logistic growth equation, no units)
- β Beta (constant value for logistic growth equation, no units)
- γ Gamma (constant value for logistic growth equation, no units)
- μm Micrometer (1/1,000,000 of a meter)

List of Abbreviations

ADEOS	Advanced Earth Observing Satellite I (no units)
ADEOS-2	Advanced Earth Observing Satellite II (no units)
ArcGIS	Aeronautical Reconnaissance Coverage Geographic Information Systems (no units)
AVIRIS	Airborne Visible InfraRed Imaging Spectrometer (no units)
CAVIS	Clouds, Aerosols, Vapors, Ice, and Snow (no units)
CDF	Cumulative Distribution Function (no units)
Cm	Centimeters (10^{-3} meters)
DN	Digital Number (no units)
ENVI	The Environment for Visualizing Images (no units)
ENVISAT	Environmental Satellite (no units)
GLI	Global Imager (no units)
IRL	Indian River Lagoon (no units)
Km.	Kilometers (1000 meters)
m.	meters
MERIS	The Medium Resolution Imaging Spectrometer (no units)
NASA	National Aeronautics and Space Administration (no units)
NIR	Near Infrared (no units)
Nm	Nanometers (10^{-9} meters)
OCTS	Ocean Color Temperature Sensor (no units)
PDF	Probability Density Function (no units)

Pixel	picture element (no units)
POLDER	Polarization and Directionality of the Earth's Reflectances (no units)
ROI	Region of Interest (no units)
SeaWiFS	Sea-viewing Wide Field-of-View Sensor (no units)
Sr	Steradian
STK	Systems Tool Kit (no units)
TOA	Top of Atmosphere (no units)
UTC	Universal Time Coordinated (Days, Hours, Minutes, Seconds)
W	Watts
WV-3	WorldView-3 (no units)

List of Equations

2.1

$$p(\xi, \eta) = \frac{1}{2\pi} \exp\left(-\frac{1}{2}(\xi^2 + \eta^2)\right) \left[1 + \frac{1}{2}c_{12}\xi(1 - \eta^2) + \frac{1}{6}c_{30}\xi(3 - \xi^2) + \frac{1}{24}c_{40}(3 - 6\xi^2 + \xi^4) + \frac{1}{4}c_{22}(1 - \xi^2)(1 - \eta^2) + \frac{1}{24}c_{04}(3 - 6\eta^2 + \eta^4)\right]$$

.....12

2.2 $\frac{dN}{dt} = rN\left(1 - \frac{N}{K}\right)$40

2.3 $\frac{dN}{dt} = rN^\alpha\left[1 - \left(\frac{N}{K}\right)^\beta\right]^\gamma$ 40

2.4 $\int \frac{dN}{N(1-\frac{N}{K})} = \int r dt$43

2.5 $\int \frac{1}{N} + \frac{1}{K-N} = \int r dt$43

2.6 $\ln|N| - \ln|K - N| = rt + C$43

2.7 $\ln\left|\frac{K-N}{N}\right| = -rt - C$43

2.8 $\left|\frac{K-N}{N}\right| = e^{-rt-C}$43

2.9 $N = \frac{K}{1+e^{-rt-C}}$44

3.1 $R = \frac{K}{1+e^{-rt-C}}$81

3.2	$\ln \left[\frac{K-R}{R} \right] = -rt - C$	81
3.3	$R_i' = R_i - b_i(R_{NIR} - Min_{NIR})$	91
3.4	$R_{red}' = R_{red} - 0.08143558(R_{NIR} - 0.0003)$	92
3.5	$R_{blue}' = R_{blue} - 0.09085432(R_{NIR} - 0.0003)$	92
3.6	$R_{green}' = R_{green} - 0.11694104(R_{NIR} - 0.0003)$	92
3.7	$R_{red}' = R_{red} - 0.08143558(2)(R_{NIR} - 0.0003)$	96
3.8	$R_{blue}' = R_{blue} - 0.09085432(2)(R_{NIR} - 0.0003)$	96
3.9	$R_{green}' = R_{green} - 0.11694104(2)(R_{NIR} - 0.0003)$	96
3.10	$0.032 = 0.325 - 0.11694104(x)(0.041 - 0.0003)$	97
4.1	$a + (r * c^{distance})$	98
4.2	$\ln \left[\frac{K-N}{N} \right] = a + (r * c^{distance})$	101
4.3	$N_t = \frac{K}{1 + e^{a + (r * c^{distance})}}$	101

Acknowledgement

In acknowledgement of my advisor, Dr. Charles Bostater, whose guidance was incredibly invaluable to me throughout my research. Also to my family, especially my father and sister who constantly supported and cheered me on throughout my journey completing this thesis.

Dedication

Dedicated to the memory of my mother, Julie, who although was unable to support me through this journey, would have been the proudest to see me arrive here.

1. Introduction

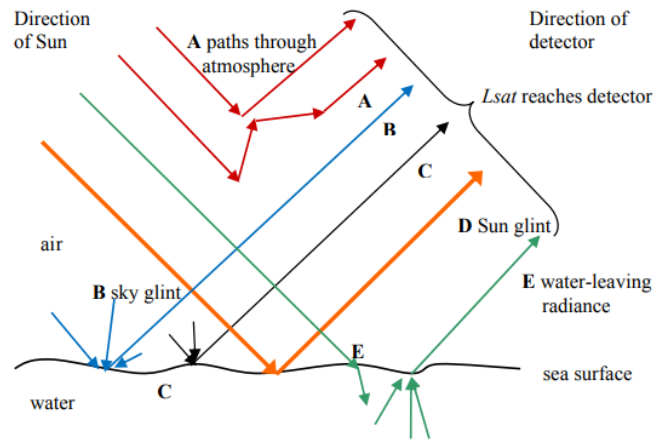
1.1 General

Remote sensing involves the collection of data on a subject acquired from a distance away from the subject. There are a multitude of subjects that cannot be properly studied as a whole unless they are observed by remotely collecting data, such as large bodies of water, large scale areas of vegetation or forests, and even other planets and celestial bodies. Obtaining and analyzing remotely sensed imagery of large bodies of water in particular is an important tool for understanding properties of the water and what lies beneath the sea surface. Properties of a water column such as the composition of the bottom substrate, concentrations of certain substances like mg/L of chlorophyll, mg/L of dissolved organic matter and suspended sediments in the water column, amongst other variables can be estimated through the study of remotely sensed imagery. One major obstacle to extracting useful information from image pixels is the presence of sun glint, which contaminates the signal being received by a sensor looking at the water surface.

1.2 Sun Glint

Sun glint is a term that refers to the occurrence of light from the sun being directly reflected off the sea surface to the detector/sensor of an instrument mostly due to wind driven waves, thus contaminating pixels in images with light that is not

being emitted from below water itself. Sun glint is subsequently a function of the state of the sea surface as well as the sun and sensor geometry at the time an image is acquired. Wind wave facets are very important factors in sun glint. Some instruments will attempt to avoid a majority of wave induced sun glint by choosing a specific flight pattern and/or direction. Figure 1.1 (Kay, 2009) shows the components of light that make up the signal received by a detector or sensor.



- **A** Single or multiple scattering in the atmosphere, by molecules or aerosols
- **B** Scattering from the atmosphere to the water surface and then reflection to the detector—often termed “sky glint”
- **C** Reflection from whitecaps on the sea surface
- **D** Specular reflection from water surface, with direct transmission through the atmosphere from the sun to the surface and from the surface to the detector—this is termed ‘sun glint’ in the context of this review.
- **E** Transmission through the atmosphere and air-water interface followed by scattering or reflection below the water surface and transmission back through the atmosphere to the detector.

Figure 1.1: In this figure, A is due to light scattered in the atmosphere that reaches the detector, B is due to light scattered in the atmosphere that reaches the sea surface and then reflects to the detector (sky glint), C is due to light reflected from whitecaps (bright white foam from breaking waves), D is light from the sun that directly reflects off the sea surface to the detector, and E is light from the sun that is transmitted through the atmosphere and sea surface and then emitted back out towards the detector (Kay, 2009).

As shown in component D of figure 1.1, sun glint is the part of the signal received by the detector that is examined and modeled in this thesis. The amount of sun glint that reaches a detector in an image with a fixed sun and sensor zenith would be dependent on the state of the sea surface reflecting the glint light, which is a product of various factors including wind speed and direction and the fetch distance and duration.

1.3 Research Goals and Outcomes

The goal of this research was to ascertain whether a reliable and applicable sea surface sun glint statistical model could be created using the “residuals” between two satellite images taken with a small time lag, wherein one of the images is largely contaminated by glint and the other is almost entirely glint free. To attain this, several goals were outlined as described below.

Model Building Goals

1. Obtain WorldView-3 Imagery from DigitalGlobe.
2. Use ENVI software to radiometrically correct imagery and to calculate water surface reflectance from the upwelling radiance.

3. Create image fetch distance transects using ENVI software.
4. Linearize the logistic growth of the reflectance due to fetch using non-linear statistical methods.
5. Use Systat to perform regression to estimate optimal coefficients from physically based mathematical models of reflectance.
6. Understand viewing geometry of both images as well as all parameters that would influence the occurrence and amount of sun glint present in a pixel.
7. Analyze coefficients in a physically based equation to help explain which glint inducing factors cause the variance of the glint.
8. Formulate a mathematical expression or model that can be applied generally to other imagery.
9. Compare other selected glint correction methods to the images the model is based on.
10. Create an assessment of the effectiveness of the model.

2. Background

2.1 Remote Sensing of Spectral Signatures of Water Bodies

As mentioned previously, remote sensing science entails the process of gathering data on a subject from a distance. Utilizing satellites or airborne sensors to remotely sense data of bodies of water allows one to collect spectral reflectance signatures of a water column and therefore study what is present in the water. The primary factors that influence the distinctive shape of a spectral signature of a column of water are the water column depth, levels of dissolved organic matter, levels of suspended sediments, level of chlorophyll, and the makeup of the bottom of the water column (e.g., sand, coral, sea grass) (Bostater and Huddleston 2000). By understanding how characteristic changes to a water column surface reflectance signature is altered due to each of these components could lead to determining, what constituents are in a given column of water and/or what is underlying the water at the water bottom. This important area of study has a variety of possible applications, such as assessing ecosystem health, monitoring water quality based on concentrations of substances (Adjovu 2023) or studying phenomena such as harmful algal blooms in water, as well as detecting submerged

vegetation or other bottom textures. Figure 2.1 shows modeled spectral signatures of pure water (no concentrations of chlorophyll, suspended sediments, or dissolved organic matter) with different bottom compositions created using python based on the two-flow model detailed in “Advancement of an optical remote sensing model to simulate the underwater light field” by Bostater et al. (Bostater, 1997). These were modeled for this research using bottom reflectance collected in clear Caribbean Sea waters (Bostater, 2000).

Reflectance of pure water at depth of 10m with different bottom

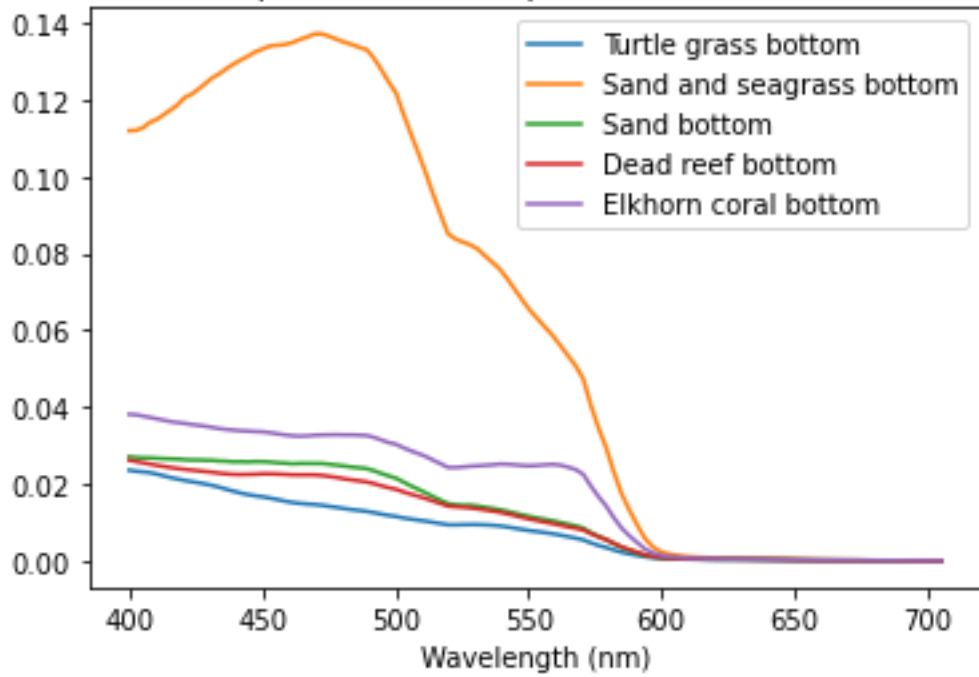


Figure 2.1: Five bottom type spectral signatures modeled for a 10 meter depth of pure water. Showing water surface irradiance on the y axis and wavelength on the x axis. Different bottom types can be seen to produce unique characteristics in water surface spectral reflectance signature.

As seen in figure 2.1, the presence of certain features can produce unique water surface reflectance spectral signatures of water columns knowing how bottom reflectance features influence the water surface. Modeling such as the above allows one to better understand and analyze spectral signatures obtained from satellite imagery. These signatures change due to the presence of sun glint due to wave facets. If a given pixel is contaminated by the presence of glint, true information about the upwelling underwater light field can be misunderstood. Thus a feature in a spectral signature due to the presence of a certain substance or bottom type may be obscured by the saturation of reflectance due to glint. When large areas of an image are contaminated by glint, it can become entirely unusable. This can create problems when conducting any sort of research using satellite imagery, as it is costly to purchase imagery and, in some cases, difficult to obtain imagery of a specified location of interest on multiple occasions. According to Landinfo Worldwide Mapping (Land Info, 2018), ordering archival imagery for WV-3 would cost \$19 per sq. km. if purchasing panchromatic and multispectral bands, with a minimum order area of 25 sq. km. and a 2 km order width. If looking to purchase imagery of a new area not within archives, costs increase even more. A bundle of panchromatic and multispectral bands would cost \$29 per sq. km. with a minimum order area of 100 sq. km. and a minimum order width of 5 km (Land Info, 2018).

For these reasons it is in a researchers best interest to ensure that sun glint can be avoided or corrected as much as possible.

2.2 Existing Sun Glint Correction Methods

Various methods are currently implemented for the removal of sun glint from satellite imagery of the sea surface. As discussed in Kay et al. (Kay, 2009), there are two major versions of glint correction commonly used on oceanic imagery depending on the resolution of the satellite and location of the imagery: using statistical models or using Near Infrared (NIR) band signal. Currently, statistical models can only moderately correct glint for larger resolution images of the open ocean at a pixel scale of approximately 100 to 1,000 meters due to their large error. Otherwise, to attempt a correction of oceanic imagery at a smaller resolution and away from open ocean conditions, typically one employs correction methods using a NIR wavelengths. These methods, however, are also generally limited to near shore imagery. But water features actually change within resolutions smaller than approximately 10 meters.

For correction methods using statistical methods, factors such as wind speed and direction and sensor and sun geometry are used to estimate the probability that the sea surface orientation will create sun glint. Following this, an estimate is made of the magnitude of sun glint in a pixel and this is subtracted from the pixel's reflectance. These methods have been applied to SeaWiFS imagery on the SeaStar spacecraft, POLDER instruments launched on several French satellites, OCTS on

the ADEOS Japanese satellite, MERIS on ENVISAT, and GLI on the Japanese ADEOS-2 satellite (Kay, 2009).

Additional statistical modeling correction methods employ statistical models of sea surface roughness after Cox and Munk (Cox, 1954). Cox and Munk created a PDF (Probability Distribution Function) of sea surface slopes based on a series of 29 aerial photos. They found that sun glint intensity data was approximately Gaussian in shape. This knowledge is used to determine the probability that the sea surface will be oriented to cause sun glint using wind speed and direction. This probability is then used to predict the amount of sun glint for a given wind vector and sun and sensor position. All of the aforementioned instruments have used a variation of the Cox and Munk model for their sun glint correction given by:

$$p(\xi, \eta) = \frac{1}{2\pi} \exp\left(-\frac{1}{2}(\xi^2 + \eta^2)\right) \left[1 + \frac{1}{2}c_{12}\xi(1 - \eta^2) + \frac{1}{6}c_{30}\xi(3 - \xi^2) + \frac{1}{24}c_{40}(3 - 6\xi^2 + \xi^4) + \frac{1}{4}c_{22}(1 - \xi^2)(1 - \eta^2) + \frac{1}{24}c_{04}(3 - 6\eta^2 + \eta^4)\right] \quad 2.1$$

Where p is the probability index, ξ is a standardized slope component in the x and crosswind directions, η is a standardized slope component in the y and downwind directions, and all instances of c are a skewness coefficients. Using Equation 2.1 obtained from laws of reflection with the wind dependent PDF slopes

that they created, Cox and Munk were able to create a model predicting the amount of sun glint present in a pixel given by:

$$mss = \sigma_w^2 + \sigma_c^2 = 0.003 + 0.00512U \pm 0.004 \quad 2.2$$

where mss is mean square slope, σ_w and σ_c are root mean square slopes of the water surface (downwind and crosswind), and U is wind speed (m/s). This gives mean square slope values used to create a distribution (PDF) that is then plugged into Equation 2.1. Various other studies have been conducted following the Cox and Munk model that introduce modifications to their model. Work by Wu et al. (Wu, 1990) worked with the same data as Cox and Munk, however they produced results with a slightly different mean square slope function. In recent years, some studies have been conducted replicating the Cox and Munk experiment with new data, such as work by Ebuchi and Kizu (Ebuchi, 2002) that used about 30 million data points from imagery to produce a model with somewhat differing results (a narrower distribution with less dependence on wind). The instruments that employ the Cox and Munk model often utilize different approaches to correct for sun glint. For example, MERIS data processing for glint removal is accomplished by creating a predicted glint reflectance for a pixel using the Cox and Munk model, then creating a ratio of this value and the actual reflectance value to obtain a glint reflectance. If the glint reflectance is too low or high, it won't be corrected,

resulting in only the pixels with a medium amount of glint being corrected.

SeaWiFS glint correction is accomplished with a differing method, where predicted glint reflectance using the Cox and Munk model is normalized for a solar radiance of 1 and no atmosphere in order to allow for an estimation of aerosol optical thickness (Kay, 2009). Most of these efforts are applied to imagery in open waters away from shorelines or ocean boundaries.

Near Infrared (NIR) data is used to estimate the radiance received due to sun glint by a sensor and then applied to visible channels. NIR wavelengths have a property where they are nearly entirely absorbed by water molecules, so one can assume that most of the light reaching the sensor in NIR wavelengths is due to atmospheric scattering and sun glint. Once atmospheric correction is performed, one assumes the remaining signal in the NIR band is entirely sun glint and this fraction of quantity is subtracted from the reflectance in the visible wavelengths. This assumes all NIR signal in a channel is due to sun glint, and that the water itself does not contribute to reflectance at these wavelengths, which holds true for the purpose of glint correction. This method can be applied to shallow waters with a much smaller resolutions compared to statistical glint removal techniques, on the order of 10 meters. Data from several well known sensors employ NIR methods, such as the IKONOS Satellite's sensor, AVIRIS flown on various NASA aircraft, and the AISA Eagle and Hawk hyperspectral sensors (Kay, 2009).

There are many variations of the NIR glint correction method used that all generally follow the same steps. One method that has been used to correct glint using NIR wavelengths is the method by Hedley, 2005. For this method, a sample area is selected and the minimum Near Infrared (NIR) reflectance in the area is determined and then one performs a linear regression between the NIR pixel values of the sample area and the visible bands corresponding pixel values. The linear regression slope is then used in an equation that produces the corrected reflectance value for a pixel, shown in equation 3.3.

Another method outlined by Lyzenga et. al, they use a covariance estimate to determine a relationship between NIR and Visible bands instead of a linear regression (Lyzenga et. al, 2006). In a method outlined by Kutser et. al, the reflectance in the Oxygen band (760 nm) is compared to reflectance values before and after the Oxygen band to estimate the amount of glint present, assuming a proportionality between the amount of glint and the depth of the Oxygen band (Kutser, 2009). In this research, the Hedley correction method is performed on the glint contaminated image to compare the subsequent results to the glint free image. Because the imagery used in this research is comprised of shallow depth waters near a coastline, it is considered appropriate to select a NIR correction method for comparison as opposed to statistical models used in open seas away from boundaries.

MERIS data has been used to test a unique method of sun glint correction as well- using a neural network. A neural network is comprised of a collection of algorithms trained to derive relationships between different phenomena, mimicking the functionality of a human brain (Mijwil, 2019). There were two methods used for this neural network test of MERIS data. The first method involved the estimation of sun glint. Using top of atmosphere (TOA) reflectances and viewing geometry, where the neural network is trained using radiative transfer equation simulations. In the second method, the reflectance contributions from a range of factors (one of which being sun glint) are estimated using an iterative mean square minimization method, a method very common to neural network training (Kay, 2009).

Previous work by Aziz, 2019 used a glint correction algorithm that corrected individual glint contaminated pixels by using that pixel's nearest neighbor pixel not contaminated by glint (Aziz, 2019). Subsequent work by Taggart, 2021 built upon Aziz's work by modifying the algorithm to search for glint free pixels in multiple directions (horizontal, vertical, diagonal) (Taggart, 2021). This method utilized a pixel reflectance threshold value to identify a glint contaminated pixel for correction. A ratio between both pixels in the NIR band is used in order to obtain the magnitude of the reflectance due to glint. This is then multiplied by the multispectral reflectance of the glint pixel in each band to obtain

a glint corrected reflectance value for a pixel. The NIR channel in WorldView-3 imagery was chosen for the reasons previously discussed (Taggart, Bostater, 2021). Various other newer methods for glint correction have been developed in recent years, such as a glint correction algorithm by Singh et al. in which satellite derived information, namely Rayleigh corrected radiance and clear water absorption, is solely used for correction. With this algorithm the more common glint correction parameters are not considered, such as wind speed and direction, viewing geometry angles, or sea surface conditions.

Name of Method	Brief Overview	Pros	Cons
Hedley	NIR method in which a linear regression between NIR and visible bands is used	-Straightforward and easily performed -Suitable for shallow waters	-Not suitable for large amounts of glint -Not suitable for deeper waters
Cox and Munk	Statistical method in which the probability the sea surface is oriented to cause glint is estimated	-Has been reproduced with results that generally agree with this model -Ideal for medium to high wind speeds and growing to fully developed wave conditions	-Based on a limited and outdated data set that is highly dependent on wave orientation and wind speed of the images used -Loses accuracy at low wind speeds and swell conditions
Nearest Neighbor	Method in which the nearest non-glint neighbor to each glint pixel is corrected using NIR values	-straightforward and easily implemented	-Not suitable for large amounts of glint -dependent on NIR signal
Neural Network (radiative transfer equations)	Method in which a neural network is trained to estimate sun glint using radiative transfer equations	-Highly comprehensive in terms of factors considered in the model -Performs on par with current MERIS correction methods	-Still requires further validation with more data sets -Limit for amount of glint it can correct still unknown
Neural Network (iterative mean square minimization)	Method in which a neural network is trained to estimate sun glint using an iterative mean square minimization method	-Successful in retrieving water color parameters and accurate water spectrum a majority of the time	-Limited by the amount of specular reflection -Aerosol load in atmosphere and intensity of sun glint lead to increased error

Kutser	Method in which the depth of the oxygen feature is used to estimate glint content of a pixel	-More accurate correction than other methods on shallow water vegetation areas	-Is only applicable for very shallow waters and only improves upon existing methods in areas of vegetation
Wu	Similar to Cox and Munk model but used a different wave mean square slope estimation function	-Provides an alternative function to Cox & Munk model	-Still uses the limited and outdated data set Cox & Munk was based on
Singh	Glint correction algorithm derived from Rayleigh corrected radiance and clear water absorption	-Does not rely on information such as wind speed or direction, viewing geometry angles, or sea surface slopes -glint estimation by pixel avoids overestimation -Good for dealing with clouds and aerosols	-If any band is greatly contaminated by glint, the algorithm does not work -Useful for retrieving ocean color information but not other information

Table 2.1: Comparison between all glint correction methods outlined in section 2.2.

2.3 Background on Sensor Image Processing and Sensor Geometry

When working with raw satellite imagery, each pixel in an image is represented by a digital count number (DN) that is recorded as upwelling radiance in a pixel. The WorldView-3 satellite is a push broom scanner, so it will scan one line on the ground at a time with a detector, perpendicular to the flight direction.

Each respective line is made of various pixels that are observed simultaneously using a linear diode average as represented in figure 2.2.

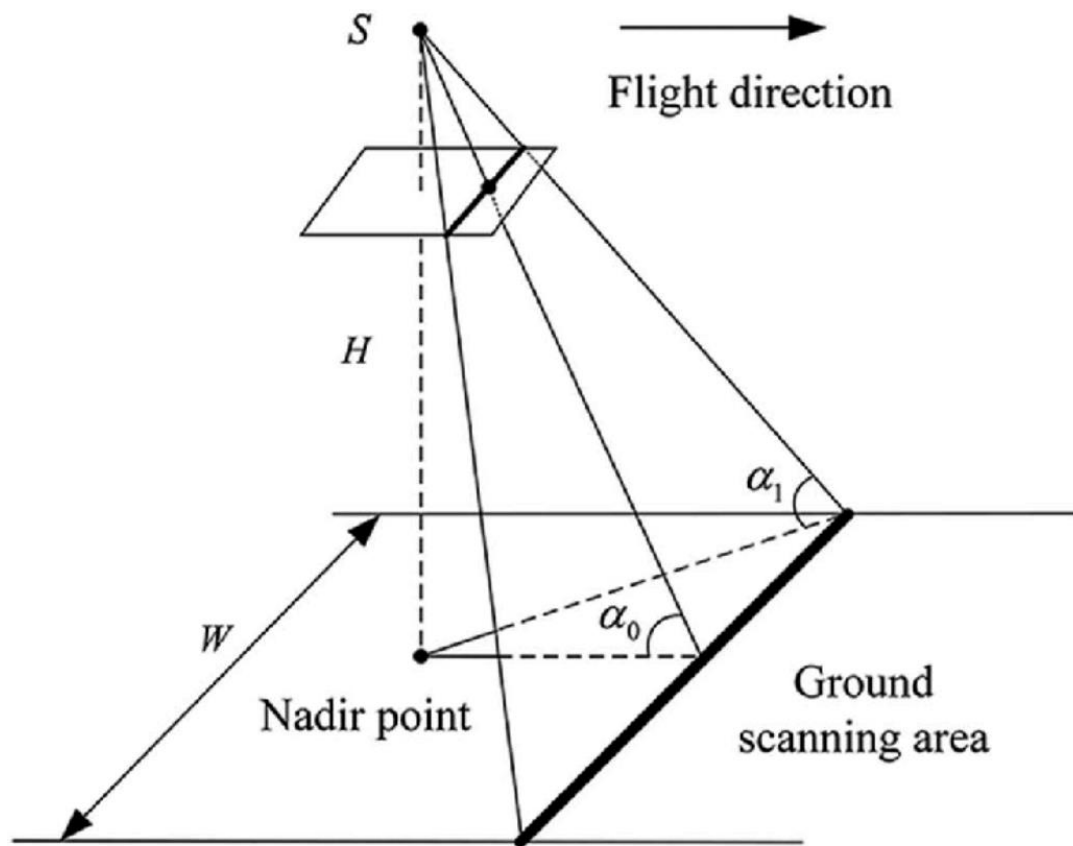


Figure 2.2: The geometry of a common push broom scanner from Cao et. Al (Cao, 2019).

In order to work with a DN image, one converts digital counts into radiance and then reflectance values. In order to convert DN pixels into pixels with radiance values, gain and offset values must be applied to the pixels. The gain and offset are provided in WV-3 metadata, and they are automatically processed into ENVI when using the “Radiometric Calibration” tools to convert DNs to Radiance. Although Radiance values will give an account of the amount of upwelling radiation in a pixel field of view, it is more common and useful to convert Radiance values to Reflectance values, to account for the downwelling irradiance at the sensor. These reflectance values are the fundamental signal in remote sensing used for analysis, when reflectance has a value of 1 would be complete saturation, and a value of 0 would indicate a pixel devoid of light when displayed on a computer (Budde, 1976). One can account for the atmosphere using a dark pixel subtraction, which entails finding the “darkest” pixel in an image and subtracting its reflectance value from all other pixels. This is done to correct for the effects of atmospheric scattering present in an image by selecting a pixel that presumably has no contributions from anything except atmospheric scattering (Chavez, 1988). This process is easily performed in the ENVI software Dark Subtraction tool for each band, using a minimum reflectance value or chosen value from a region of interest (ROI) in the image.

2.4 WorldView-3 Imagery

The WorldView-3 satellite by Maxar Technologies was deployed in 2014 to observe the Earth's surface in a circular sun-synchronous orbit, operating at an altitude of 617 km. It employs a 30-centimeter panchromatic resolution, a 1.24 meter multispectral resolution, a short-wave infrared sensor with a 4.1 meter resolution, and the CAVIS imager (clouds, aerosols, vapors, ice and snow) with 30 meter resolution. The satellite's spectral range includes a panchromatic band with a 450-800 nm bandwidth, 8 multispectral bands in visible to near infrared wavelengths each covering a range of about 100-150 nm from 400-1040 nm, 8 multibands in shortwave infrared wavelengths that each have a bandwidth of about 30-70 nm from 1195-2365 nm, and 12 CAVIS bands that correct for the features within the 405-2245 nm spectral range.

Collection scenarios

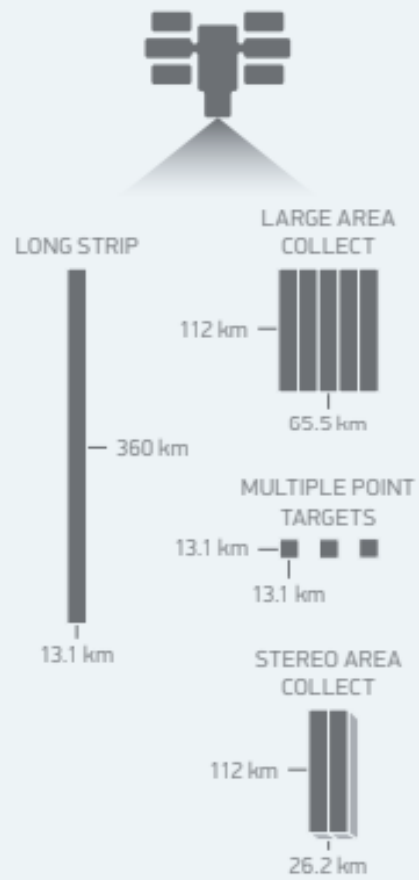


Figure 2.3: Possible WorldView-3 collection paths from the DigitalGlobe information sheet on WV-3 (DigitalGlobe, 2017).

As mentioned in the previous section, WorldView-3 is a push broom scanner with a 13.1 km swath width, as shown in figure 2.3. WorldView-3 is highly regarded for its high spatial resolution, multiple imaging capabilities such as panchromatic, multispectral, and CAVIS, relatively short average revisit time (less than 1 day), high spectral band diversity, and its ability to collect up to 680,000 square kilometers per day (DigitalGlobe, 2017).

2.5 WorldView-3 Imagery Used for the Research

For this research, two panchromatic and multispectral images were used that were taken 1 minute and 3 seconds apart. The first image, taken on 2014-08-28 at 16:01:02.552650 UTC, is largely contaminated by glint. In the second image, taken on 2014-08-28 at 16:02:05.311619 UTC, there is relatively no sun glint present. The time period between the two images is too small for the wind and wave patterns to have changed significantly. The only changes between the images were viewing geometry angles, as shown in table 2.1. Thus these sensor geometry account for the differences as far as can be determined.

Figures 2.4-2.7 show these images. In order to assess the glint present in the glint contaminated image, a residual glint image was produced by subtracting the reflectance calibrated images as shown in Figure 2.8. This residual image was calculated using the band math tool in ENVI. The difference between the two

images is termed a residual image. The residual image is a means to show the magnitude of glint at each pixel. Figures 2.9-2.11 show the position of the WV-3 satellite within its orbit, using the Systems Tool Kit software (STK).

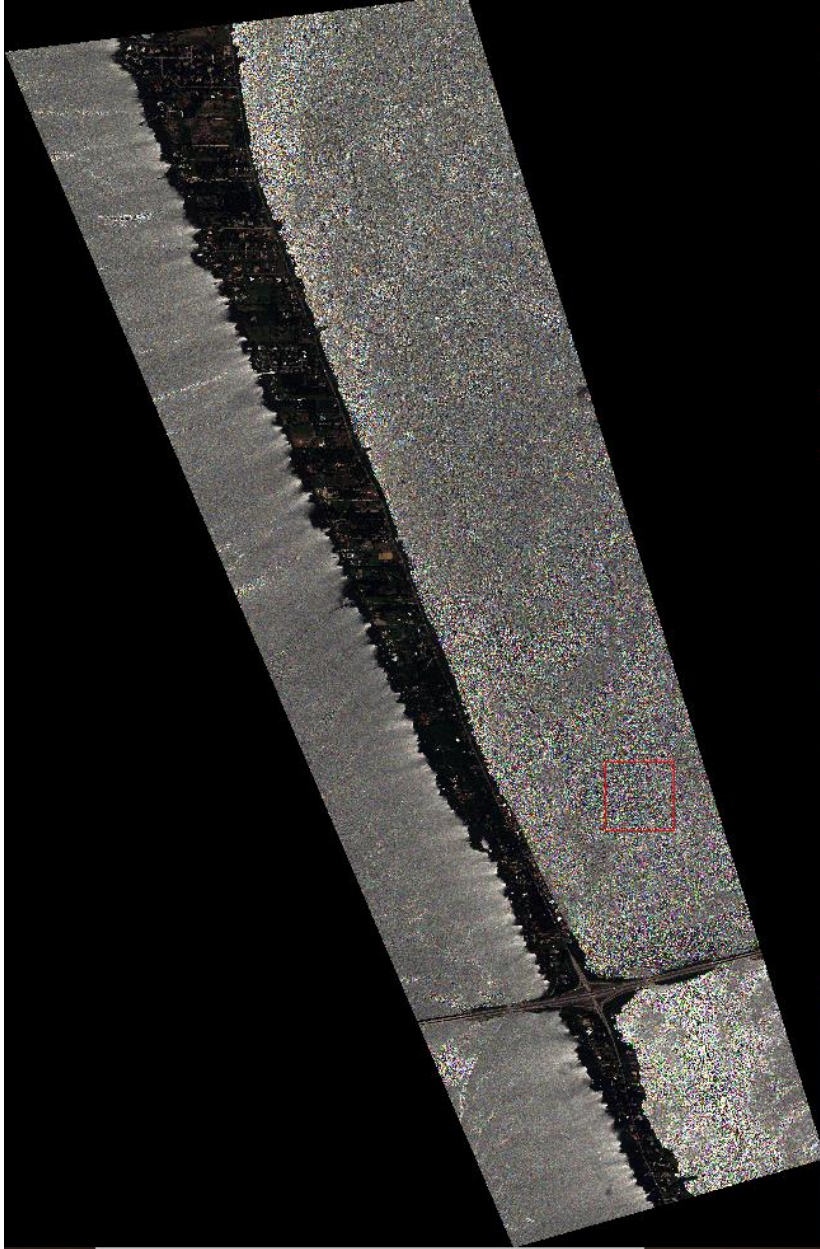


Figure 2.4: Multispectral glint contaminated image in ENVI, using Red (660 nm), Green (545 nm), and Blue (480 nm) bands. Image taken at 16:01:02.5516 UTC on 8/28/2014.



Figure 2.5: Multispectral glint free image in ENVI, using Red (660 nm), Green (545 nm), and Blue (480 nm) bands. Image taken at 16:02:05.310569 UTC on 8/28/2014.

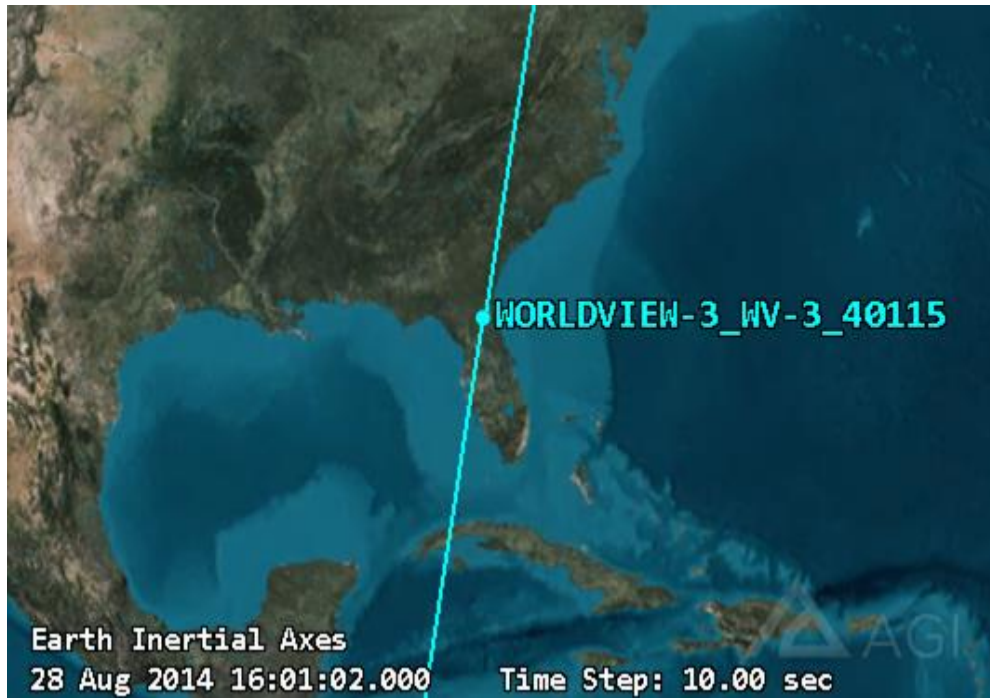


Figure 2.6: Satellite orbit positioning at the approximate time the glint contaminated image was taken. Image produced using the STK software.

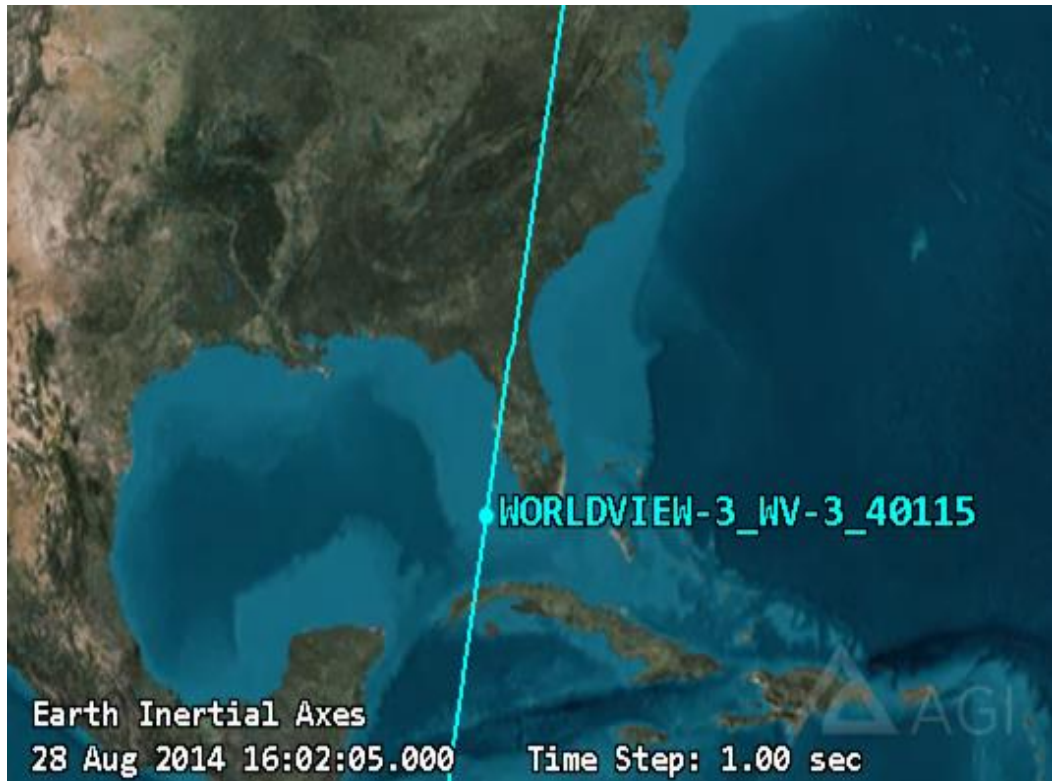


Figure 2.7: Satellite orbit positioning at the approximate time the non-glint contaminated image was taken. Image produced using the STK software.

	Glint contaminated image	Non glint contaminated image
Acquisition time	16:01:02.5516 UTC	16:02:05.310569 UTC
Off Nadir Viewing Angle	19.6°	26.6°
In Track Viewing Angle	14.9°	-22.4°
Across Track Viewing Angle	-12.8°	-14.9°
Angle of Solar Elevation	63.2°	63.3°
Satellite Azimuth	329.9°	221.5°
Satellite Elevation Angle	68.6°	60.4°
Solar Azimuth	129.5°	129.9°

Table 2.2: Viewing geometry of both images used from WorldView-3 metadata. Differences between the two are present in off nadir viewing angle, in track viewing angle, across track viewing angle, satellite azimuth, and satellite elevation angle.

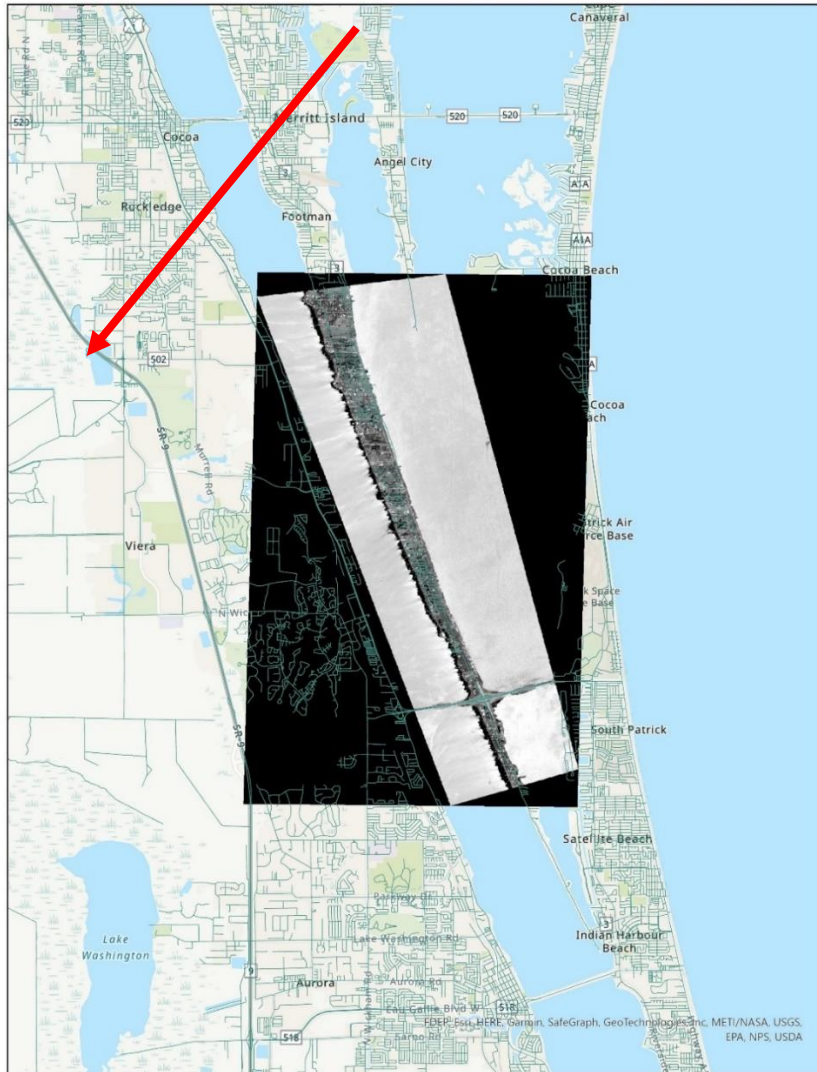


Figure 2.8: Georeferenced WorldView-3 image overlaid to land features on the map of the Melbourne, Florida area with roads using ArcGIS Pro. The extent of the imagery used can be visualized using this georeferenced point of view. Approximate satellite track indicated by red arrow.

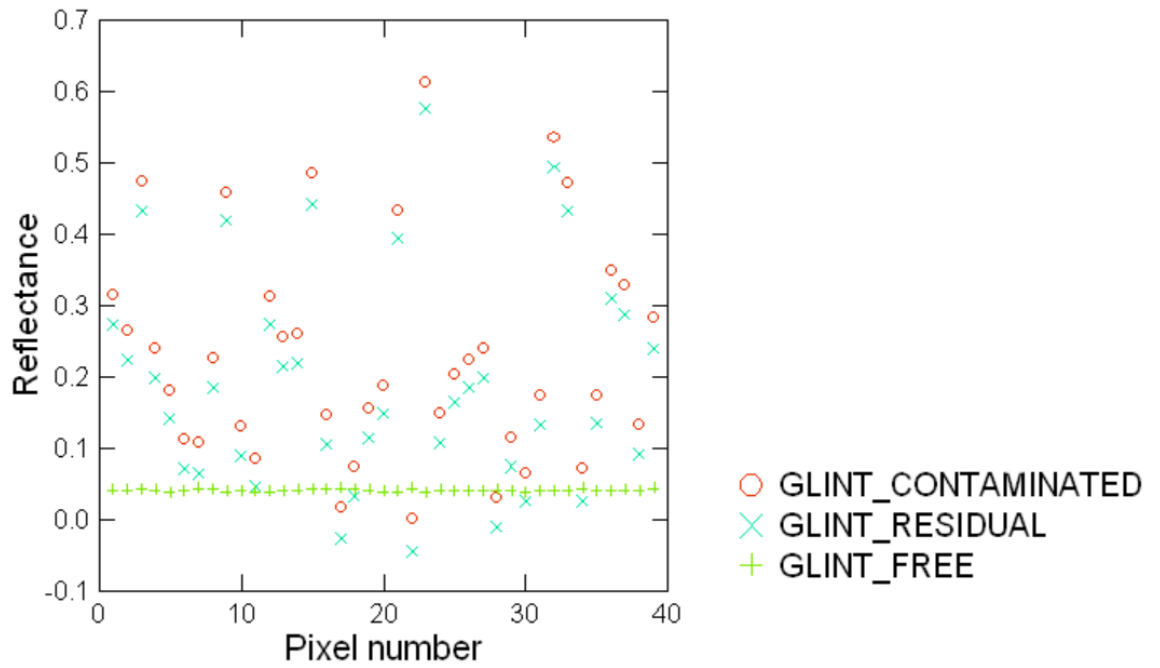


Figure 2.9: Example of reflectance values across the two images along with glint residuals compared for reference. Pixels were taken from the red band (660 nm), from a section of a transect away from the shore on the Indian River Lagoon side of the image.

2.6 Building a Glint Model

In order to build an accurate model of sun glint, one needs to correctly parameterize the factors that contribute to the existence of glint. On the sea surface, these factors are primarily the wind speed and direction, fetch distance, and azimuth and elevation angles of the sensor and sun. The prevalence of sun glint is largely influenced by the roughness of the waters surface, which is namely due to wind driven waves. The slope of a wave facet will reflect the waters surface into the satellite sensor, causing the sun glint radiance in imagery. This indicates that the wind speed and direction are extremely important to the amount of sun glint present in an image and these variables are important when considering fetch effects in semi enclosed water bodies. The geometry of the sun relative to the geometry of the sensor also plays an important role in the amount of glint reaching the detector. Because the wind blowing in a direction will increase wave slopes in the same direction, if the sun and sensor are at non-optimal angles relative to these wave slopes, the sensor could receive a large amount of sun glint. Conversely, if the sun and sensor are at optimal angles to the wave slope angles, a large amount of sun glint could be reduced, however the wave slopes and associated wind friction are random variables. Thus the wave effects can only be subtracted as mean quantities based upon the PDFs and CDFs.

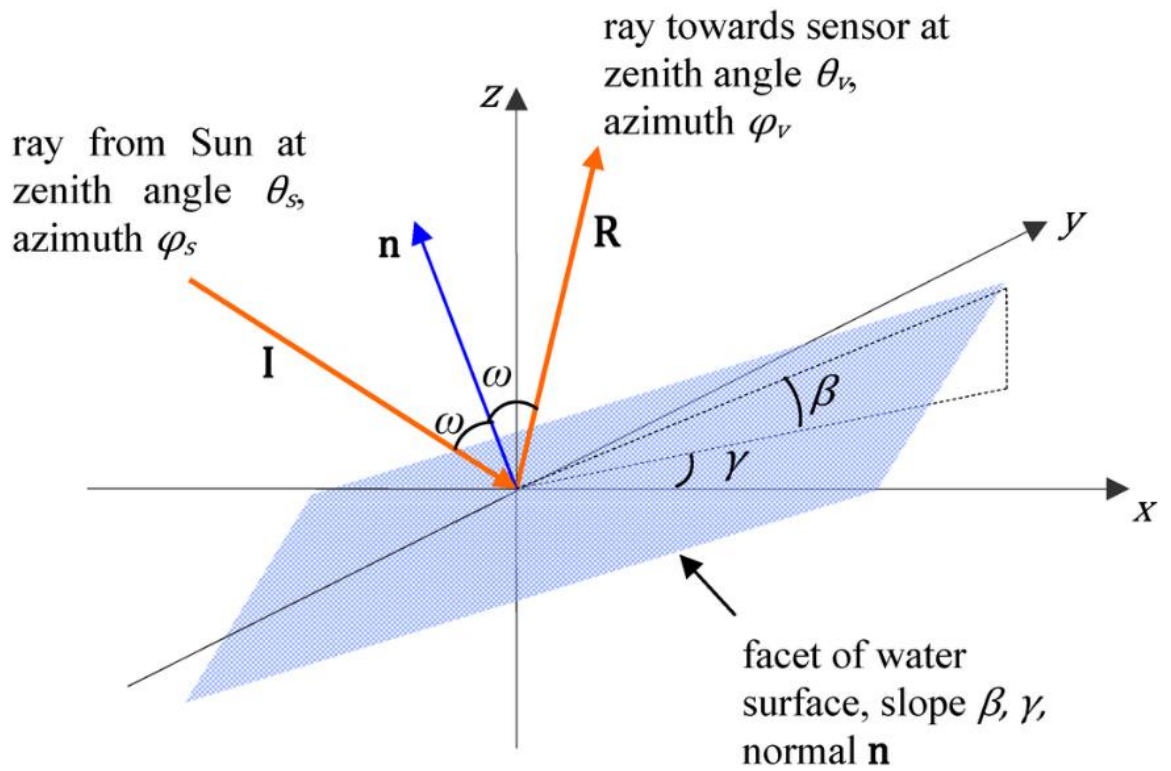


Figure 2.10: Shows how sun zenith angle, sun azimuth angle, sensor zenith angle, sensor azimuth angle contribute to glint probability. Water surface slope is influenced by wind and fetch properties (Kay, 2009).

From a global point of view, ocean wind driven currents obtain their energy from the differential heating of the Earth due to the Sun and the rotational influences of the Earth. These two forcing factors create the winds and drive circulations in the atmosphere and ocean.

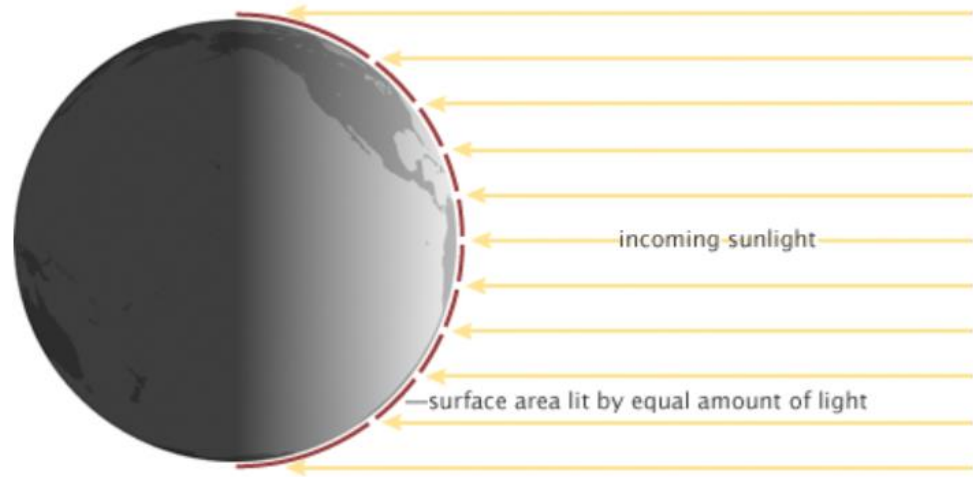


Figure 2.11: Differential uneven heating of the Earth by incoming sunlight (Nugent, 2022).

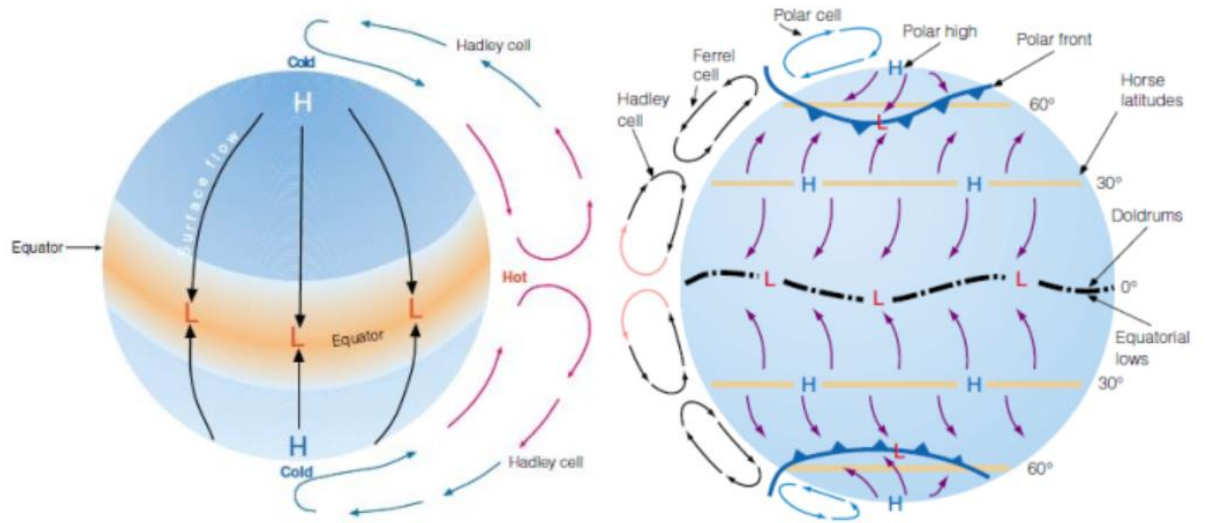


Figure 2.12: Earth winds and cells shown with the effects of rotation (right) and without (left) (Nugent, 2022).

The wind is thus the primary forcing factor in the creation of surface waves in the oceans and large water regions due to the energy to the friction flux of energy through the water.

As indicated, fetch is also an important concept that influences wind speed and wind driven waves at the water surface. The amount of energy that wind can transfer to the water surface to create waves depends on the distance over which the wind blows (fetch), as well as factors such as the amount of time the wind has been blowing in the same direction and water depth (Fagherazzi, 2009). With a larger fetch distance, larger wind driven waves will be produced, with increasing wave slopes (angles) and increasing sun glint radiance. Similarly, if the wind blows for a longer period of time uninterrupted, it will produce larger amplitude wind waves.

2.7 Logistic Growth Curve Model for Estimating Sun Glint Reflectance

The image reflectance transects created for this research follow a logistic growth curve function pattern. Logistic growth curves are characterized by their S shape, as opposed to a regular exponential growth. The logistic growth curve equation iterations in this work are derived from the Verhulst logistic equation as shown in equation 2.2 (Tsoularis, 2002).

$$\frac{dN}{dt} = rN\left(1 - \frac{N}{K}\right) \quad 2.2$$

Equation 2.2 is a version of the “generalized” logistic equation shown in equation 2.3, where α , β , and γ terms are included. These three terms are nondimensional constant values that produce varying changes to the shapes of the generalized logistic equation.

$$\frac{dN}{dt} = rN^\alpha \left[1 - \left(\frac{N}{K}\right)^\beta\right]^\gamma \quad 2.3$$

Logistic growth curves are shown with various α , β , and γ in figure 2.13 and 2.14.

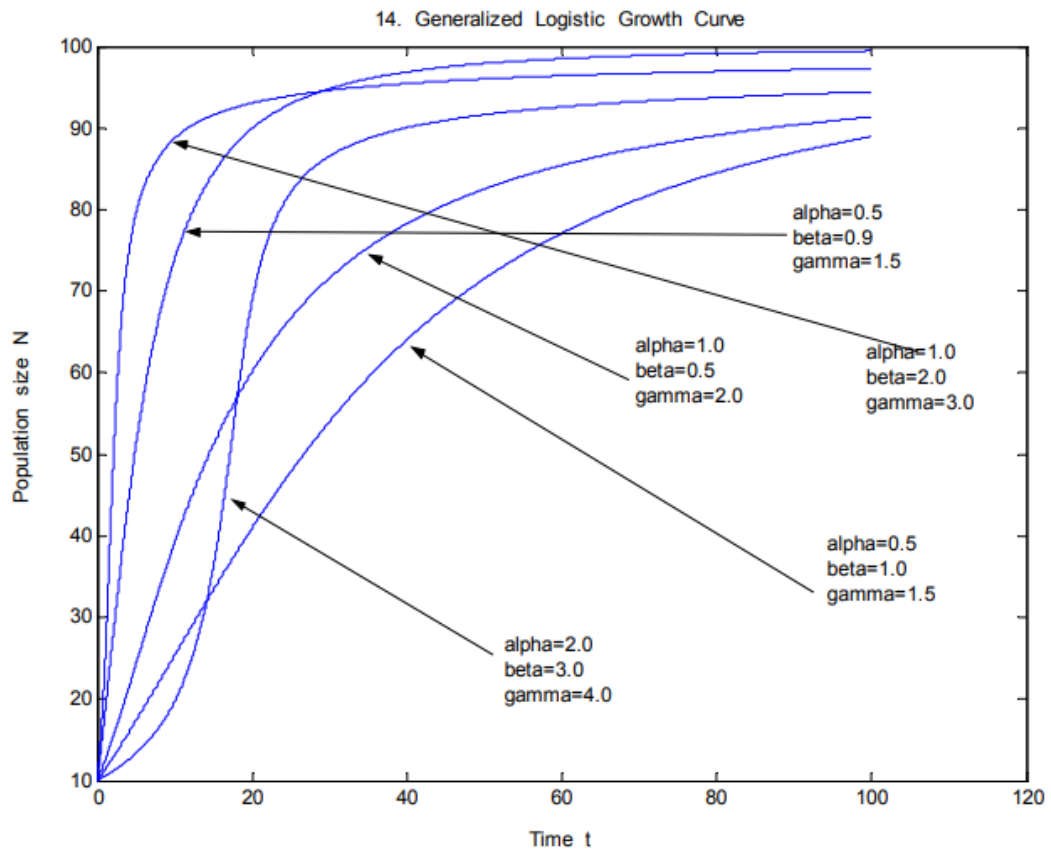


Figure 2.13: Logistic growth curves based on the generalized logistic growth curve equation, showing the influence of alpha, beta, and gamma terms (Tsoularis, 2002).

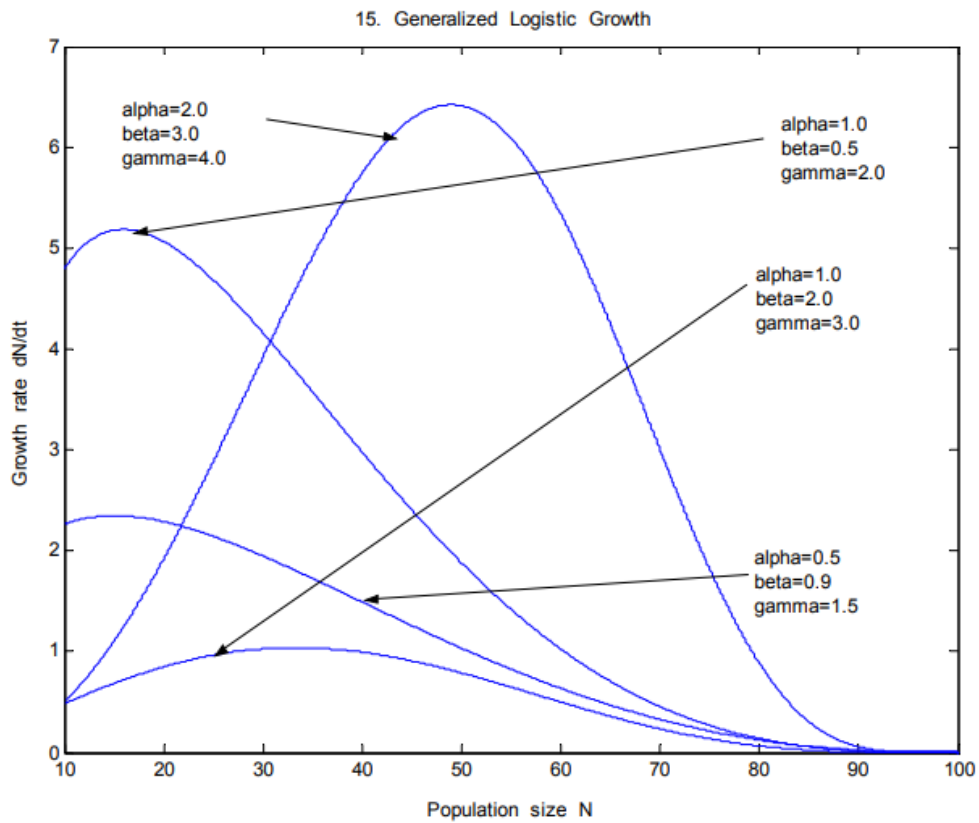


Figure 2.14: Logistic growth curves based on the generalized logistic growth curve equation, showing the influence of alpha, beta, and gamma terms. Shows population size by growth rate (Tsoularis, 2002).

In equation 2.2, the α , β , and γ terms present in the generalized equation 2.3 are all set equal to 1. Equation 2.2 can then be solved to a more useful form as seen in equations 2.4-2.9 below. By rearranging and integrating equation 2.2, equation 2.3 is produced.

$$\int \frac{dN}{N(1 - \frac{N}{K})} = \int r dt. \quad 2.4$$

Rearranging terms gives:

$$\int \frac{1}{N} + \frac{1}{K - N} = \int r dt. \quad 2.5$$

Evaluating the integrals gives:

$$\ln|N| - \ln|K - N| = rt + C, \quad 2.6$$

and rearranging gives:

$$\ln \left| \frac{K - N}{N} \right| = -rt - C. \quad 2.7$$

Applying e to both sides gives:

$$\left| \frac{K - N}{N} \right| = e^{-rt - C}, \quad 2.8$$

And rearranging again yields:

$$N = \frac{K}{1 + e^{-rt-C}}. \quad 2.9$$

Equation 2.9 is the form of the logistic equation that can be subsequently linearized as shown in section 3.4. In addition, for the logistic growth of reflectance in an image the general equation is rewritten as:

$$R = \frac{K}{1 + e^{-rt-C}}. \quad 2.10$$

Where N is replaced with R to represent reflectance. In the following methods the application of the growth of reflectance is modeled as the distance from the shoreline increases as demonstrated in Space Coast WorldView-3 imagery.

3. Methods

3.1 Processing WV-3 Multispectral Reflectance

Imagery in Fetch Limited Waters

The raw WorldView-3 images obtained from Digital Globe were processed using ENVI Classic 5.6.2 and ENVI 5.6.2. This process involves converting the pixel digital number values to radiance and then reflectance. This process is detailed in Appendix A using ENVI 5.6.2's Radiometric Calibration tool.

First, the radiometric correction is performed using the "Radiometric Calibration" tool in ENVI. This converts digital numbers to Radiance ($W/m^2 * sr * \mu m$) values using the WV-3 metadata file containing Gain and Offset information (this is a .til file with the same name as the image files). These steps were then repeated to convert to Reflectance values by selecting the Calibration Type of Reflectance instead of Radiance using the same ENVI software tool. A comparison between a pixel's DN, Radiance, and Reflectance can be seen in Figure 3.1.



Figure 3.1: Difference in pixel values when converted from DN to Radiance and Reflectance.

In the “Cursor Value” pop up box, three sections for three different files can be seen with pixel values for the red, green, and blue bands. The sections for the three files correspond to DN (bottom), Radiance (middle), and Reflectance (top). Following this procedure, ENVI’s Dark Subtraction tool was used to remove the effects of atmospheric scattering. Once the images were processed, they were opened using ENVI Classic 5.6.2 in order to utilize ENVI band math and transect tools for extracting image based reflectance along a line.

3.2 Creating Image Transects to Build Model

Transects within the images were carefully selected to provide information relating reflectance versus fetch distance. The fetch transects were limited to the lagoon side (left relative to the land) of the image due to the absence of the Banana River side’s shoreline in the imagery. Thus accurate fetch measures were taken on the Indian River Lagoon side. Figures 3.2-3.33 below show these transects in detail.

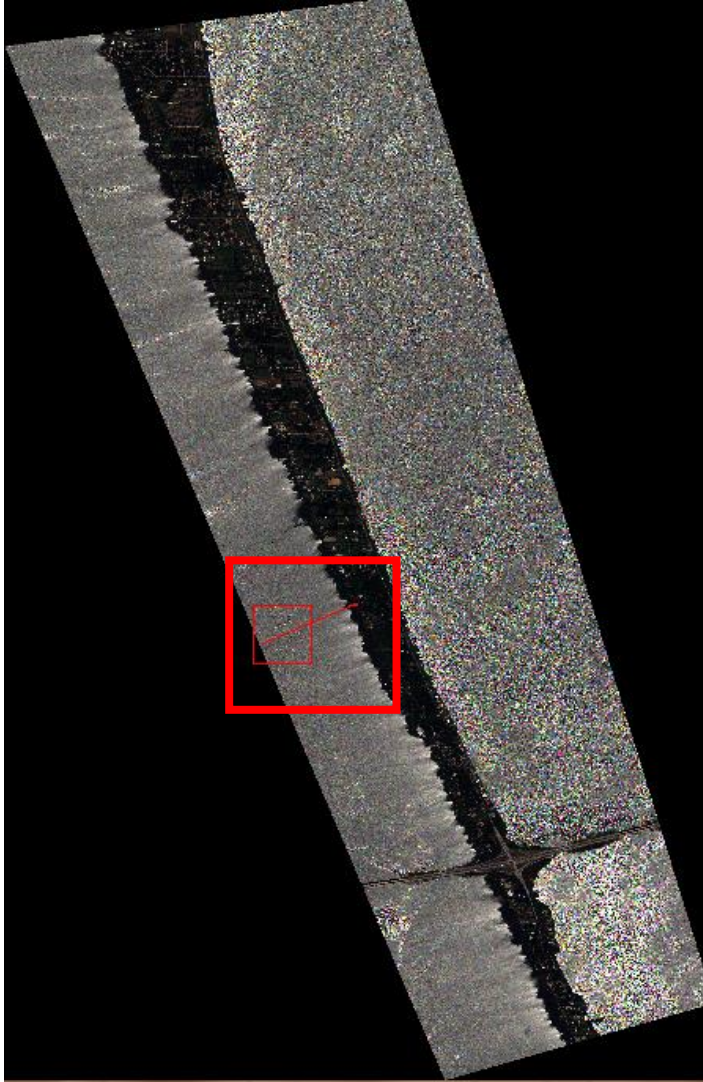


Figure 3.2: First transect created to view effects of fetch distance shown by the red line, created using ENVI. Shown using the multispectral glint image using the red (660 nm), green (545 nm), and blue bands (480 nm). Image taken at 16:01:02.5516 UTC on 8/28/2014.



Figure 3.3: Starting point of the first transect in the glint free image (left) and the glint contaminated image (right). Transects in each image are taken using the same precise pixel coordinates.

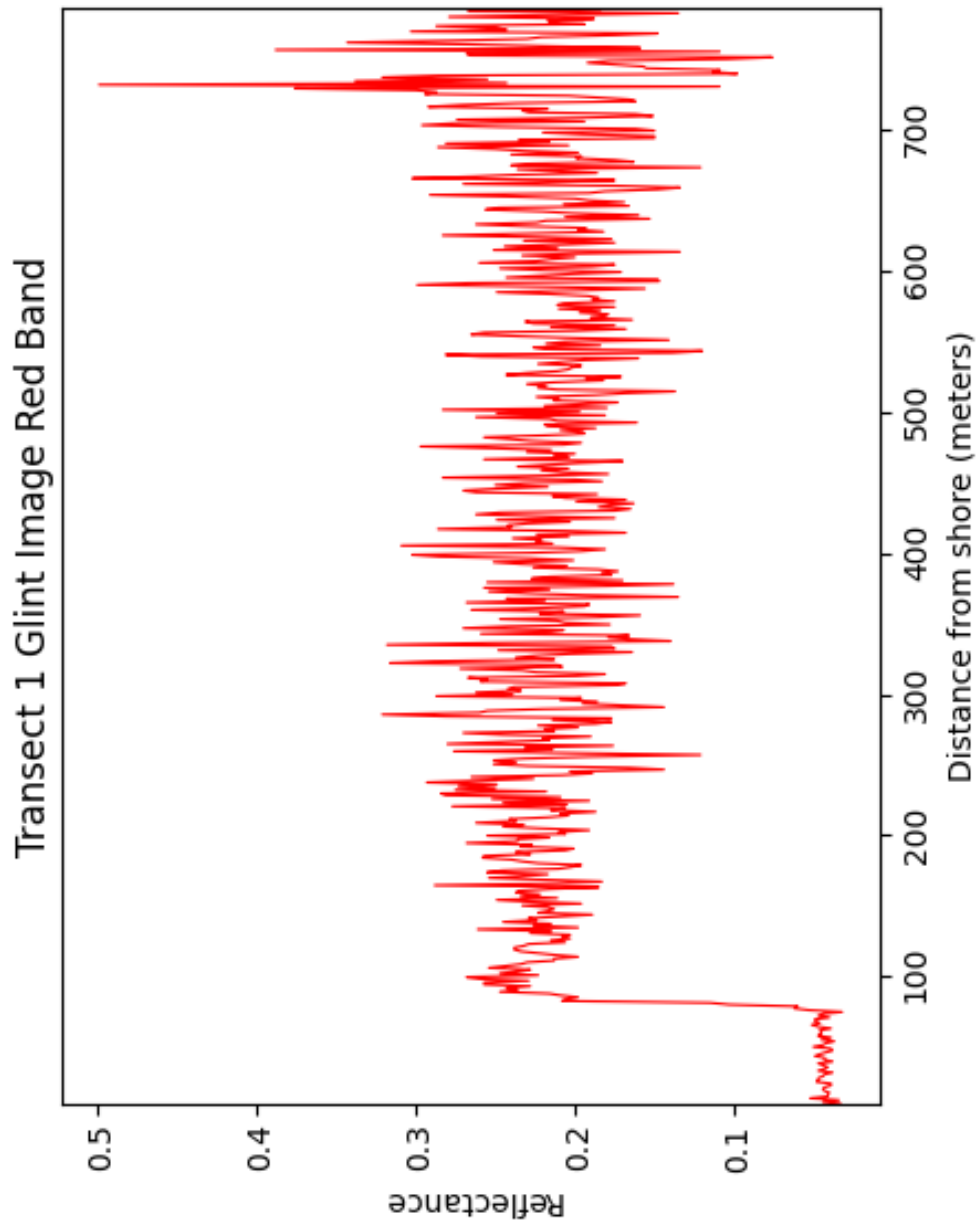


Figure 3.4: Transect 1 from the multispectral glint contaminated image as shown in Figure 3.2. Image taken on 8/28/2014 at 16:01:02.5516 UTC using the red band (660 nm). X-axis starting value represents the beginning of transect 1 on the lagoon side shore as seen in Figure 3.3.

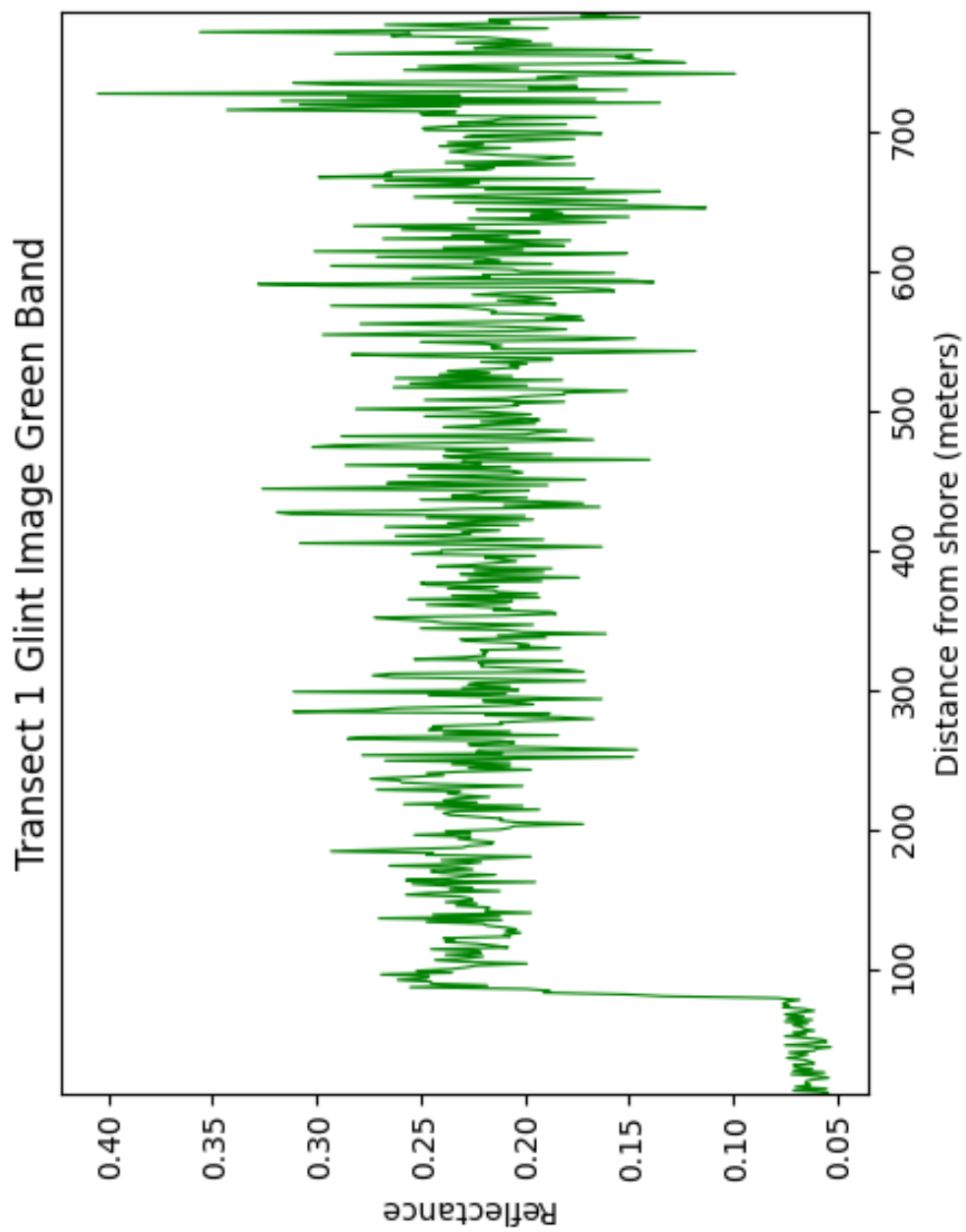


Figure 3.5: Transect 1 from the multispectral glint contaminated image as shown in Figure 3.2. Image taken on 8/28/2014 at 16:01:02.5516 UTC using the green band (545 nm). X-axis starting value represents the beginning of transect 1 on the lagoon side shore as seen in Figure 3.3.

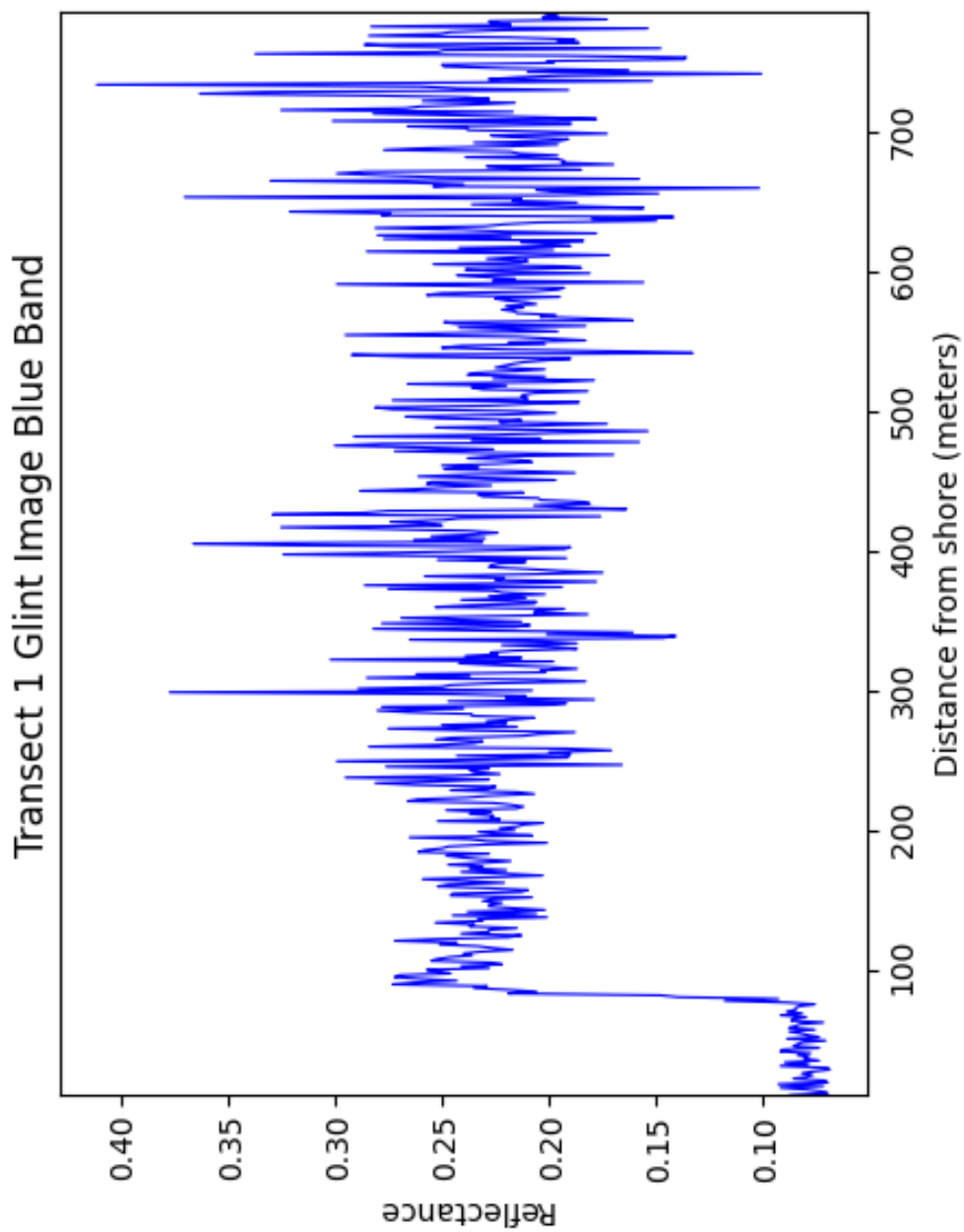


Figure 3.6: Transect 1 from the multispectral glint contaminated image as shown in Figure 3.2. Image taken on 8/28/2014 at 16:01:02.5516 UTC using the blue band (480 nm). X-axis starting value represents the beginning of transect 1 on the lagoon side shore as seen in Figure 3.3.

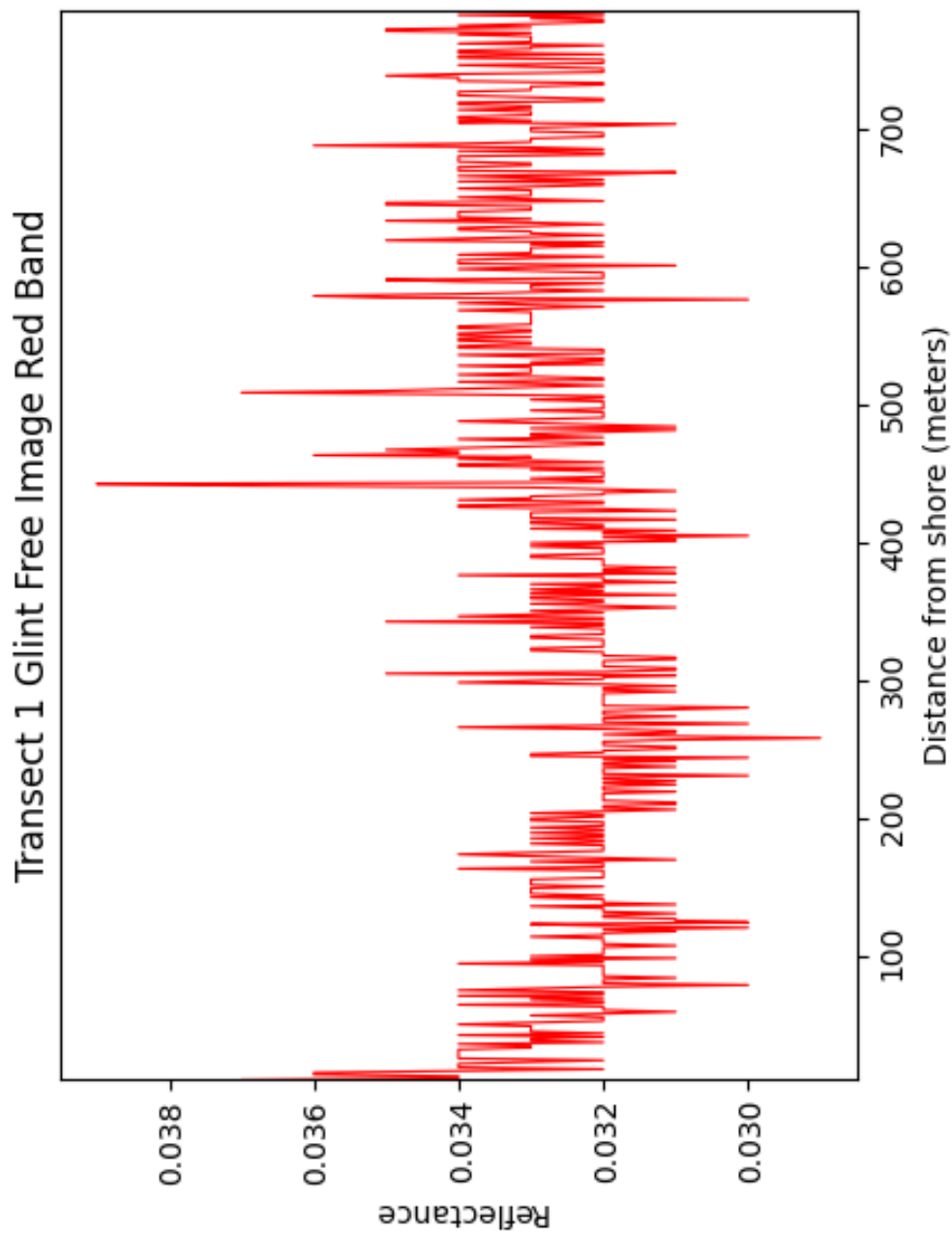


Figure 3.7: Transect 1 from the multispectral glint free image as shown in Figure 3.2. Image taken on 8/28/2014 at 16:02:05.310569 UTC using the red band (660 nm). X-axis starting value represents the beginning of transect 1 on the lagoon side shore as seen in Figure 3.3.

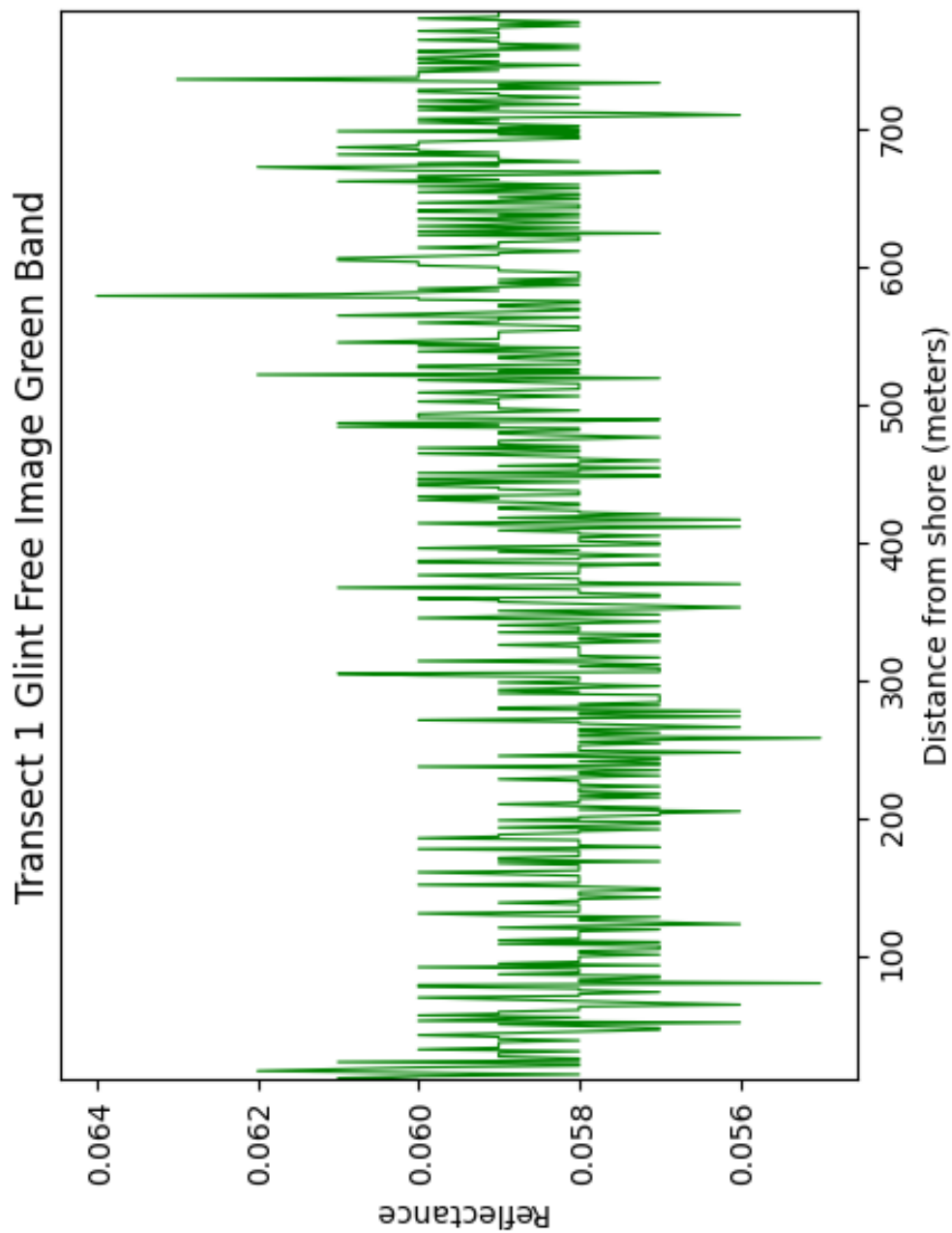


Figure 3.8: Transect 1 from the multispectral glint free image as shown in Figure 3.2. Image taken on 8/28/2014 at 16:02:05.310569 UTC using the green band (545 nm). X-axis starting value represents the beginning of transect 1 on the lagoon side shore as seen in Figure 3.3.

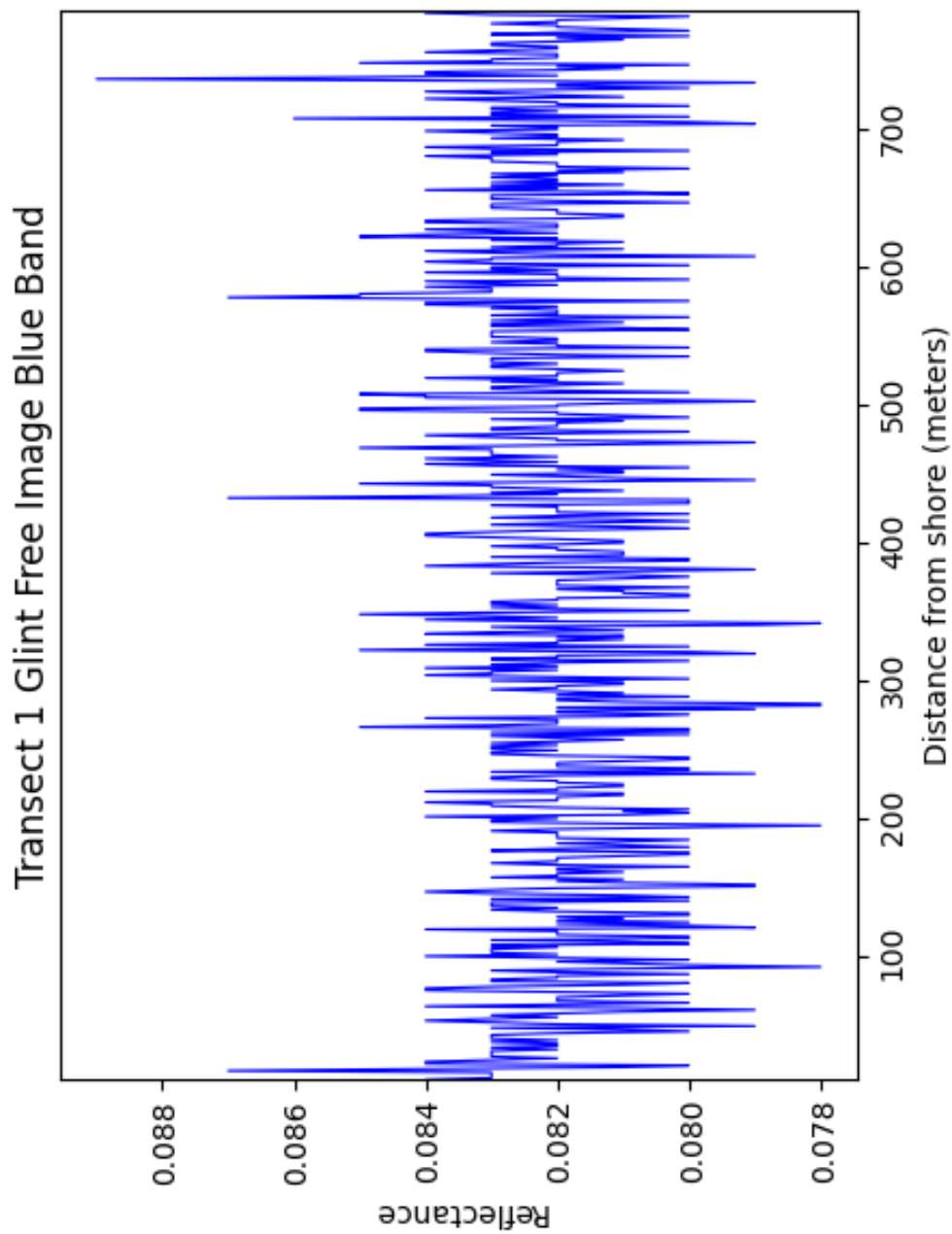


Figure 3.9: Transect 1 from the multispectral glint free image as shown in Figure 3.2. Image taken on 8/28/2014 at 16:02:05.310569 UTC using the blue band (480 nm). X-axis starting value represents the beginning of transect 1 on the lagoon side shore as seen in Figure 3.3.

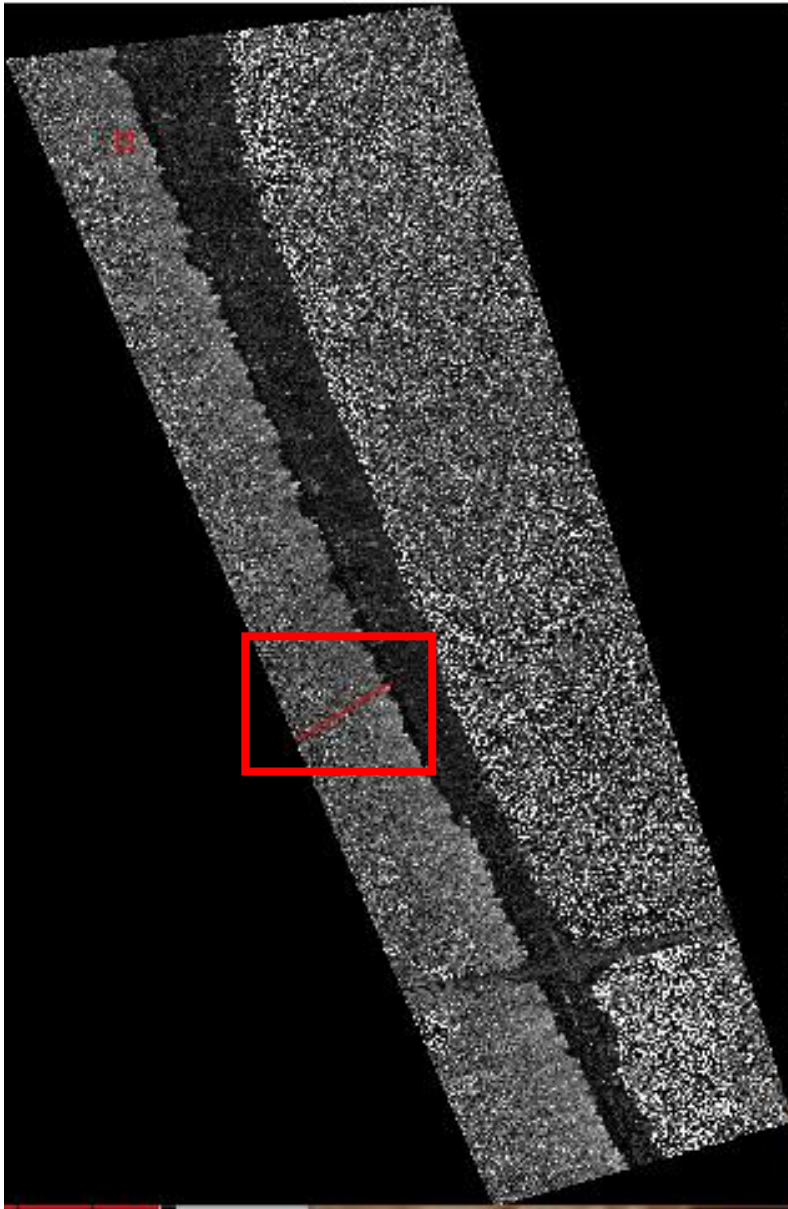


Figure 3.10: First transect (glint contaminated image) panchromatic band shown by the red line within the box. This image was taken on 8/28/2014 at 16:01:02.5516 UTC with a spectral bandwidth of 450-800 nm on the lagoon side shore.

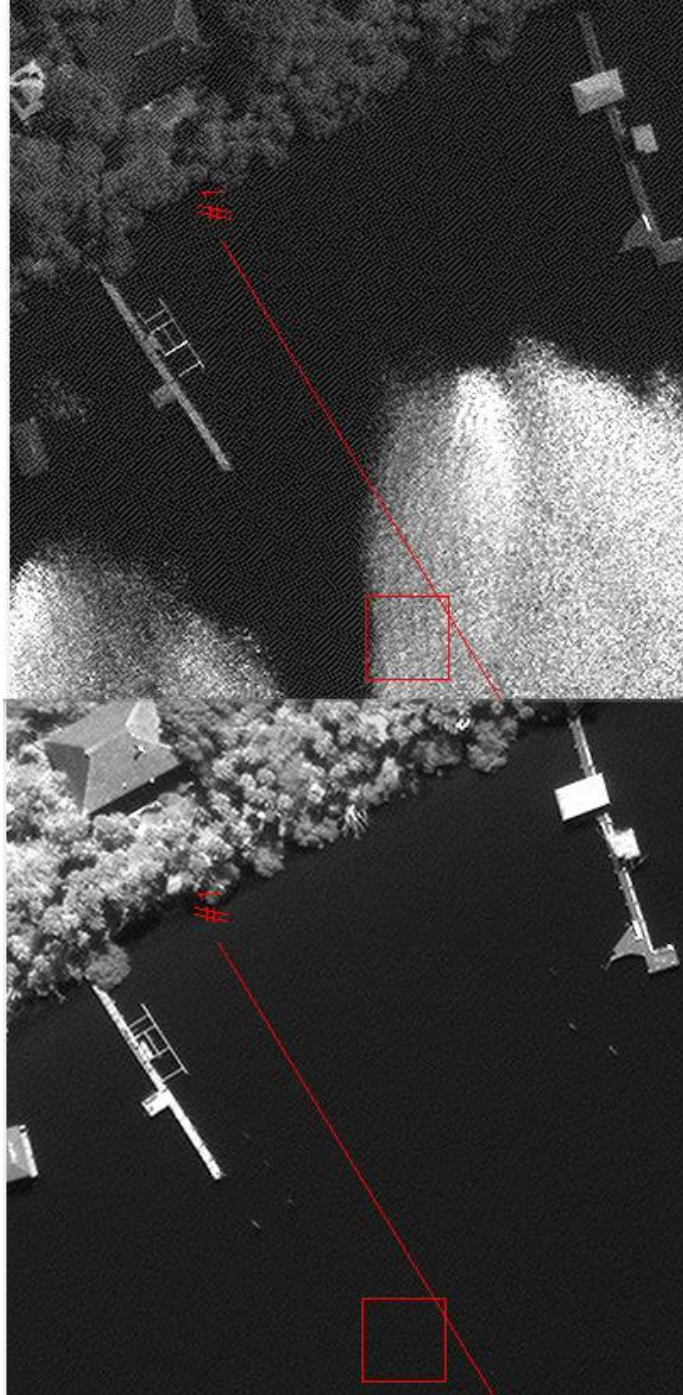


Figure 3.11: Starting point of transect 1 on the lagoon side shore in the glint free panchromatic image (left) and glint contaminated panchromatic image (right) as seen in Figure 3.10. A linear visual enhancement was applied to the glint image to better visualize the land and water and compare to the glint free image.

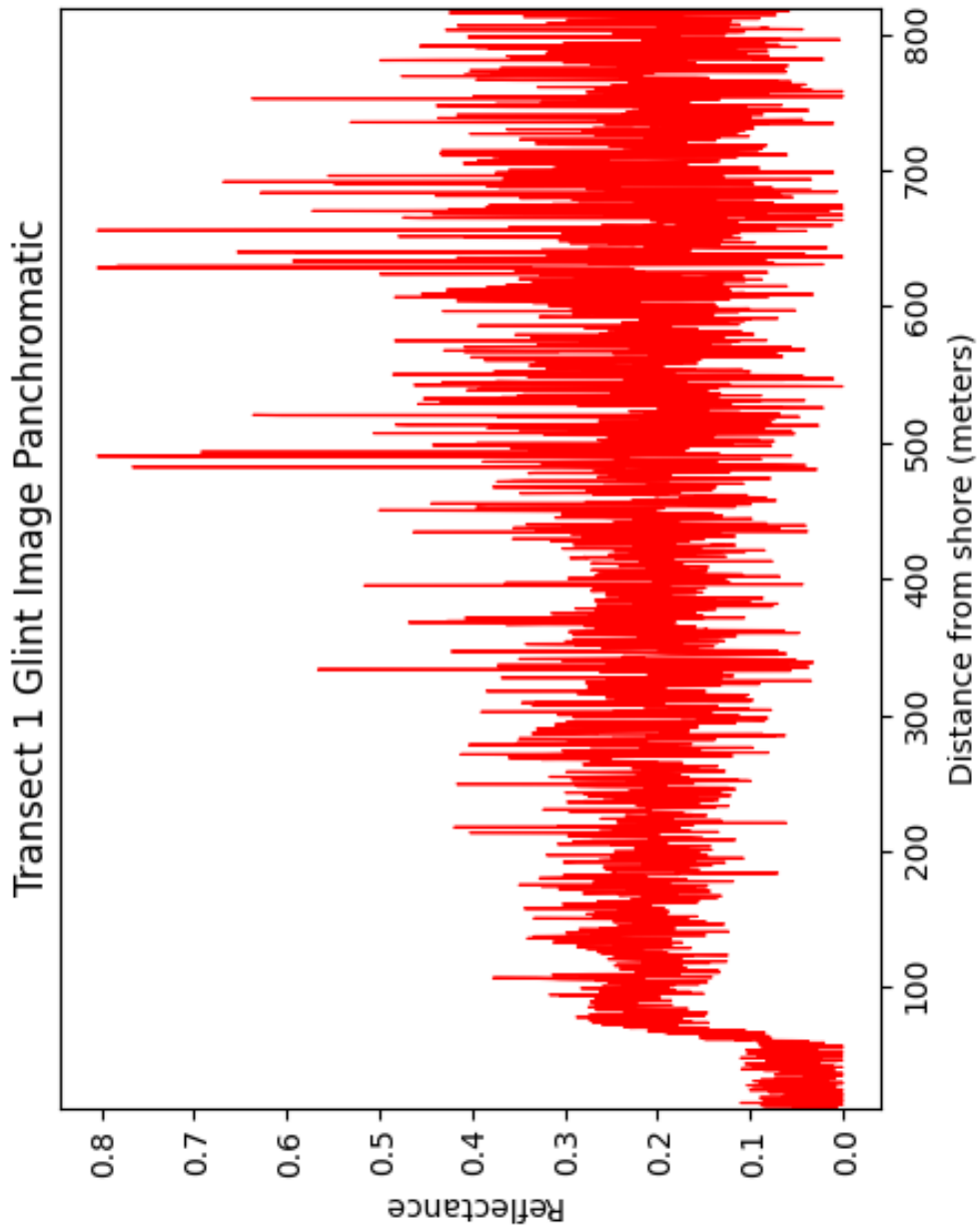


Figure 3.12: Transect 1 from the panchromatic glint contaminated image as shown in Figure 3.10. Image taken on 8/28/2014 at 16:01:02.5516 UTC. X-axis starting value represents the beginning of transect 1 on the lagoon side shore as seen in Figure 3.11.

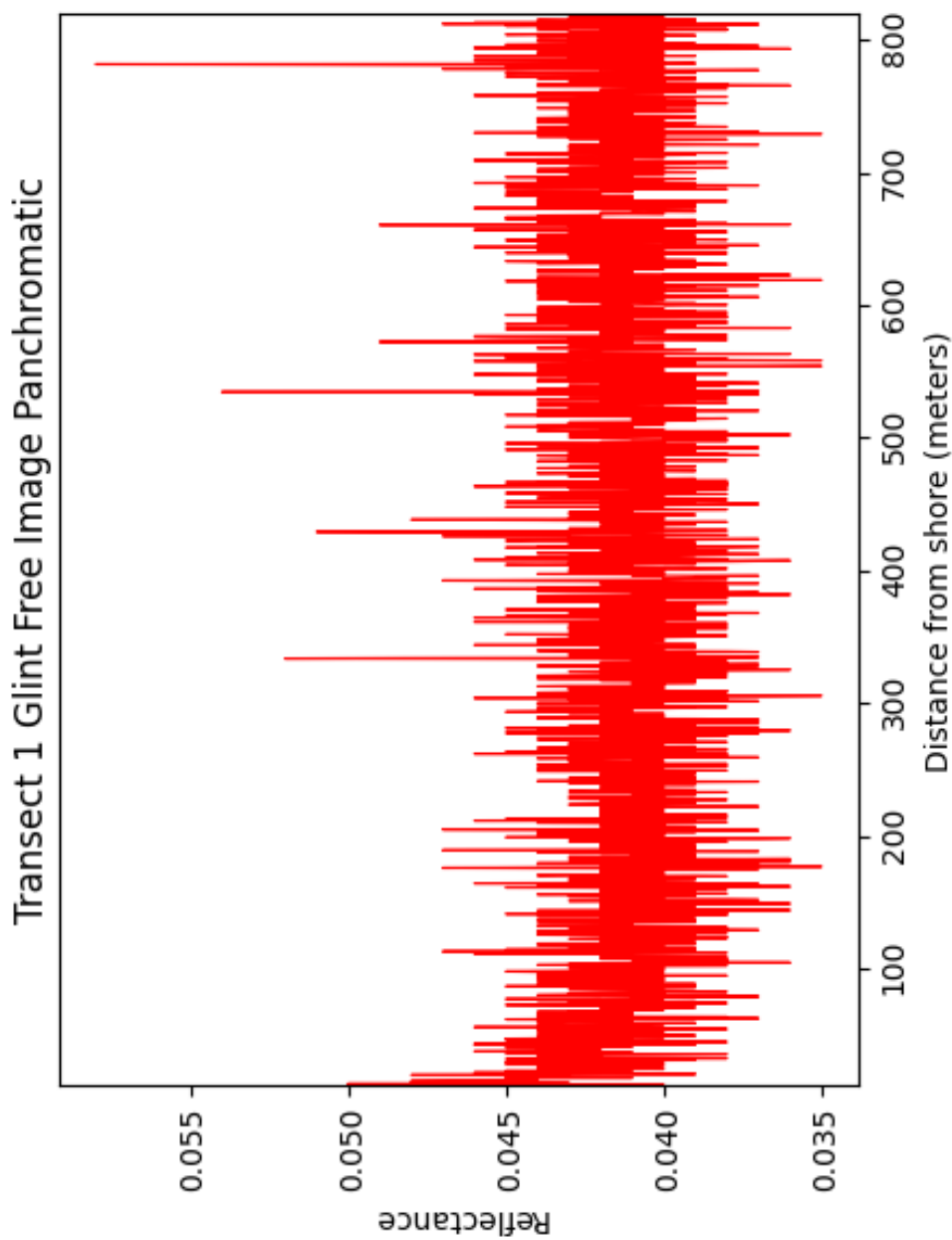


Figure 3.13: Transect 1 from the panchromatic glint free image as shown in Figure 3.10. Image taken on 8/28/2014 at 16:02:05.310569 UTC. X-axis starting value represents the beginning of transect 1 on the lagoon side shore as seen in Figure 3.11.

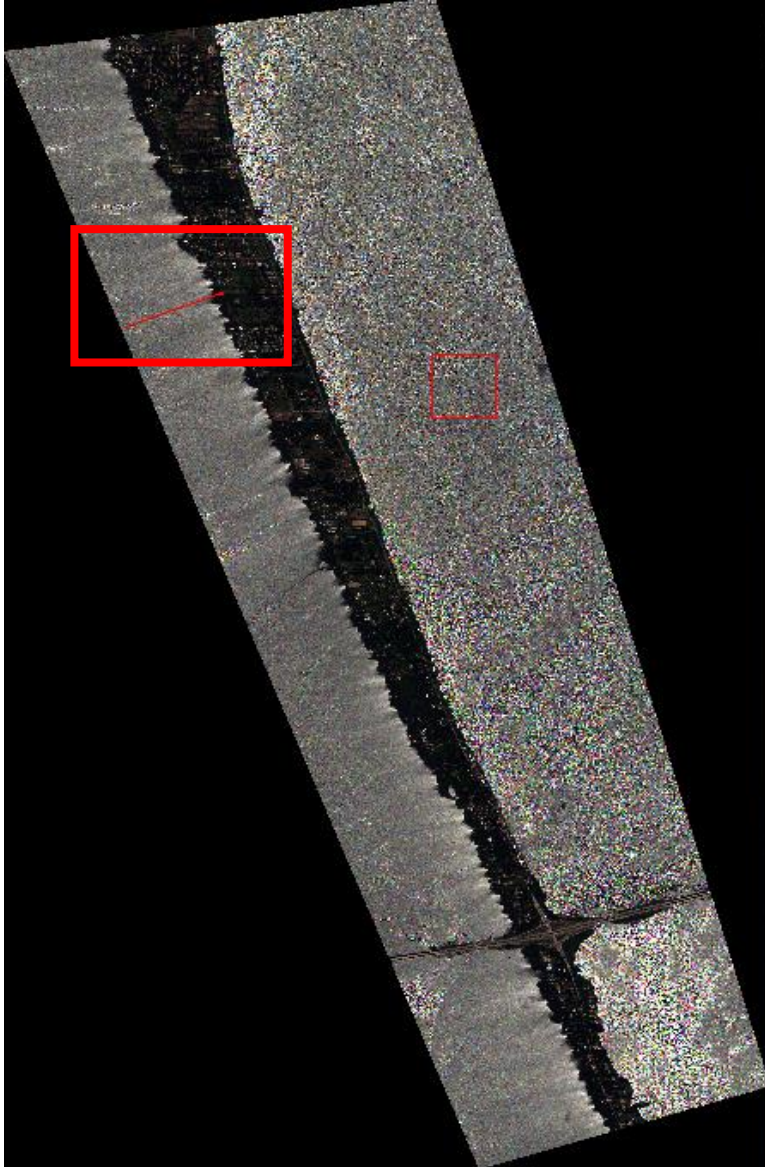


Figure 3.14: Transect 2 in the multispectral glint contaminated image shown inside the red box. This image was taken on 8/28/2014 at 16:01:02.5516 UTC, shown using the red (660 nm), green (545 nm), and blue (480 nm) bands.



Figure 3.15: Transect 2 in the multispectral glint free image shown inside the red box. This image was taken on 8/28/2014 at 16:02:05.310569 UTC, shown using the red (660 nm), green (545 nm), and blue (480 nm) bands.

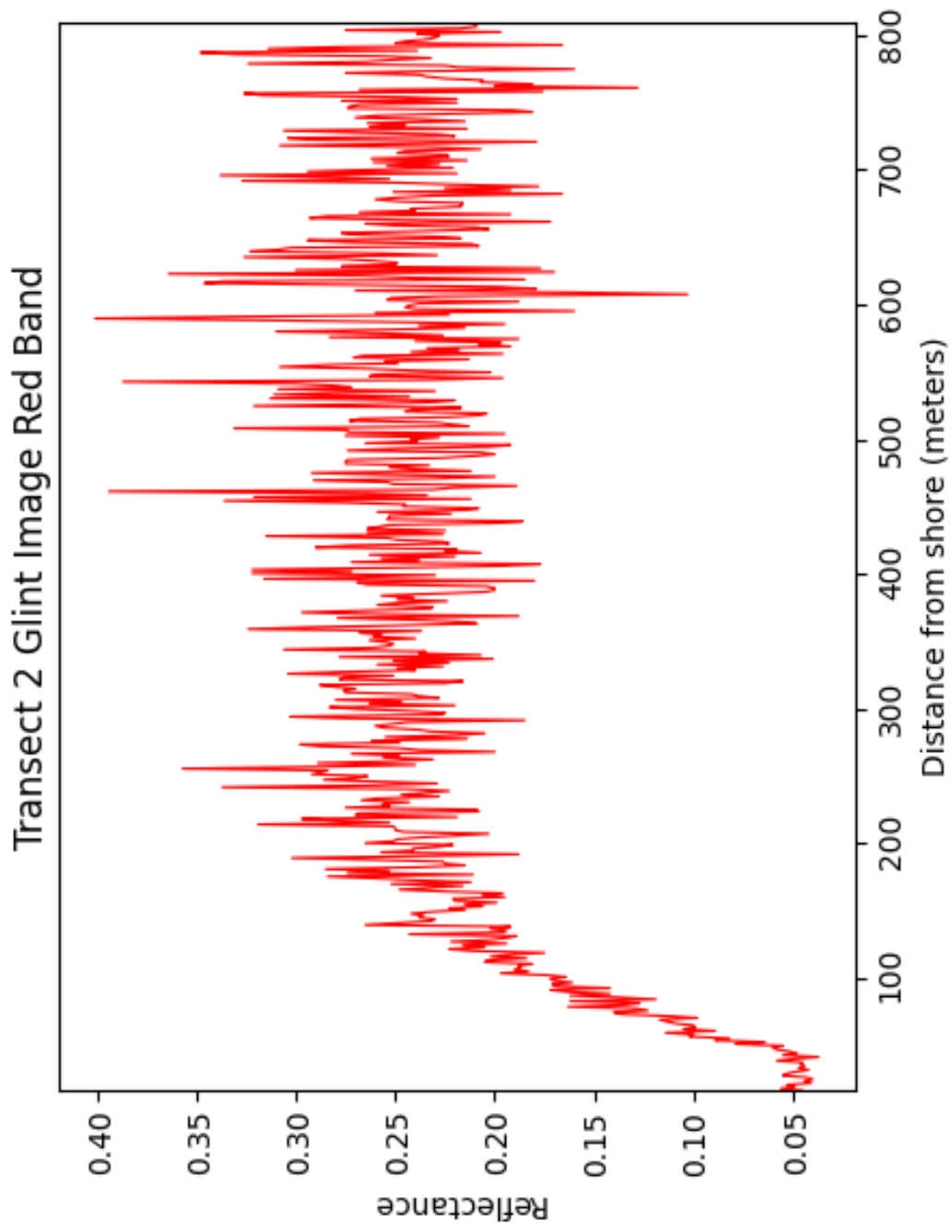


Figure 3.16: Transect 2 from the multispectral glint contaminated image as shown in Figure 3.14. Image taken on 8/28/2014 at 16:01:02.5516 UTC using the red band (660 nm). X-axis starting value represents the beginning of transect 2 on the lagoon side shore.

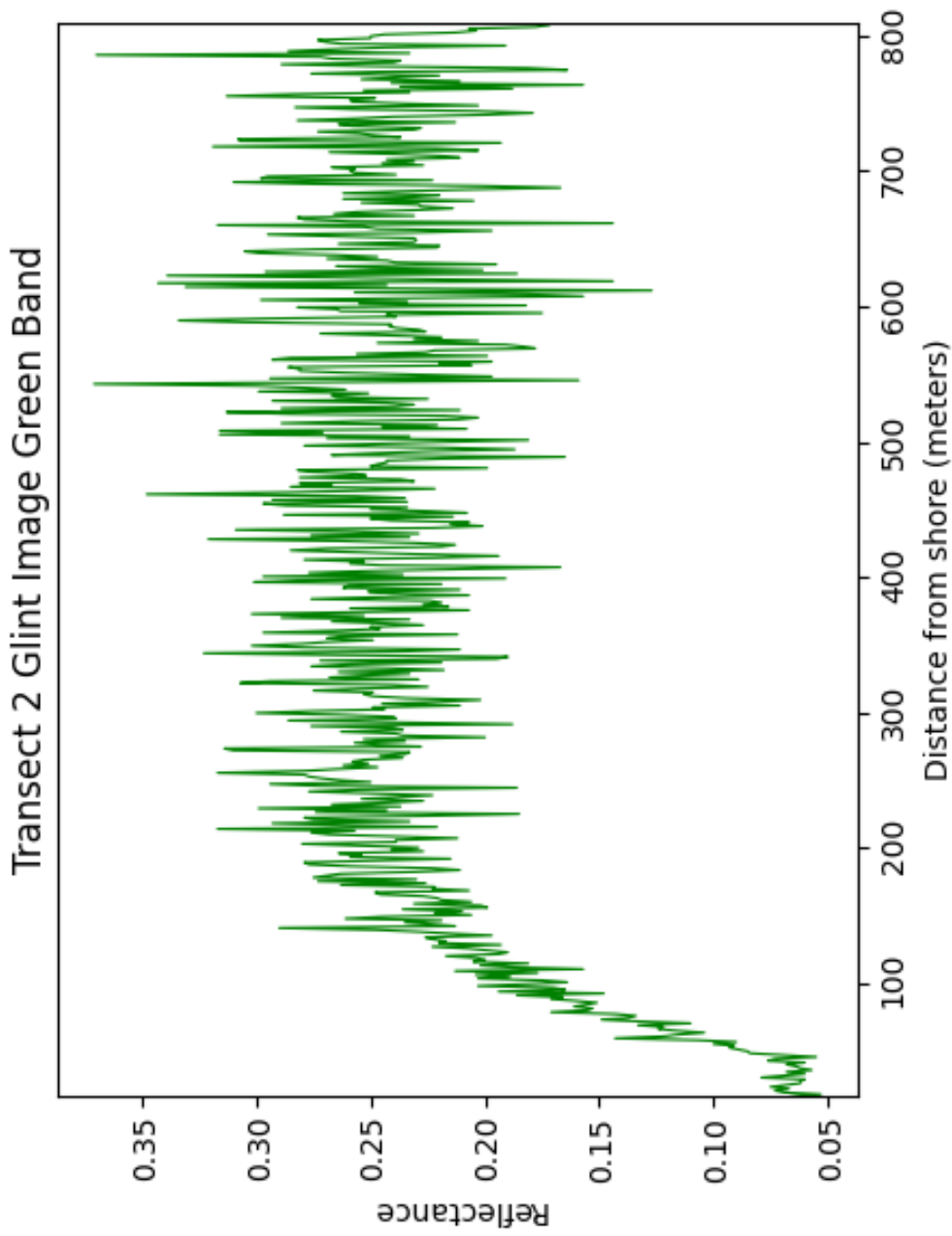


Figure 3.17: Transect 2 from the multispectral glint contaminated image as shown in Figure 3.14. Image taken on 8/28/2014 at 16:01:02.5516 UTC using the green band (545 nm). X-axis starting value represents the beginning of transect 2 on the lagoon side shore.

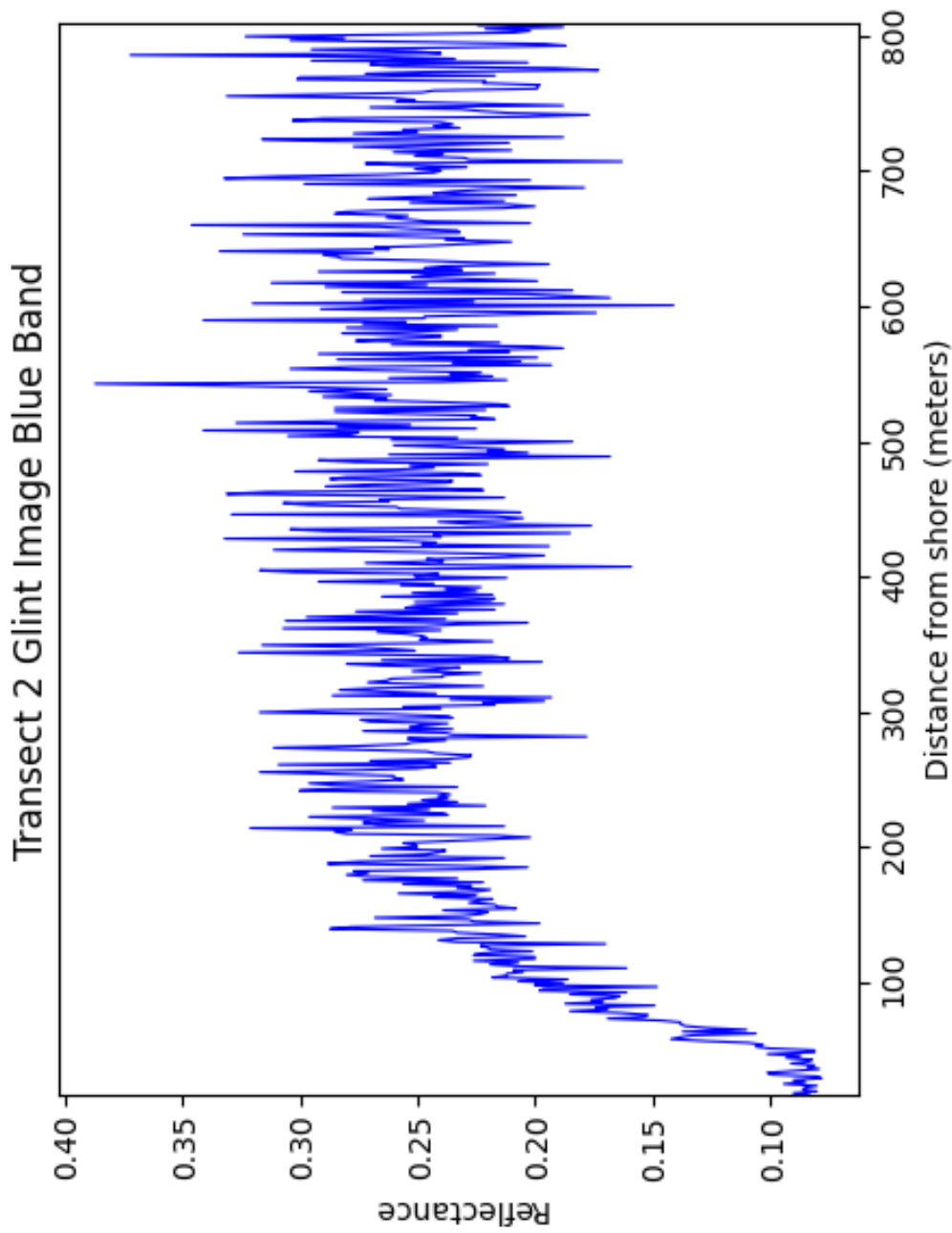


Figure 3.18: Transect 2 from the multispectral glint contaminated image as shown in Figure 3.14. Image taken on 8/28/2014 at 16:01:02.5516 UTC using the blue band (480 nm). X-axis starting value represents the beginning of transect 2 on the lagoon side shore.

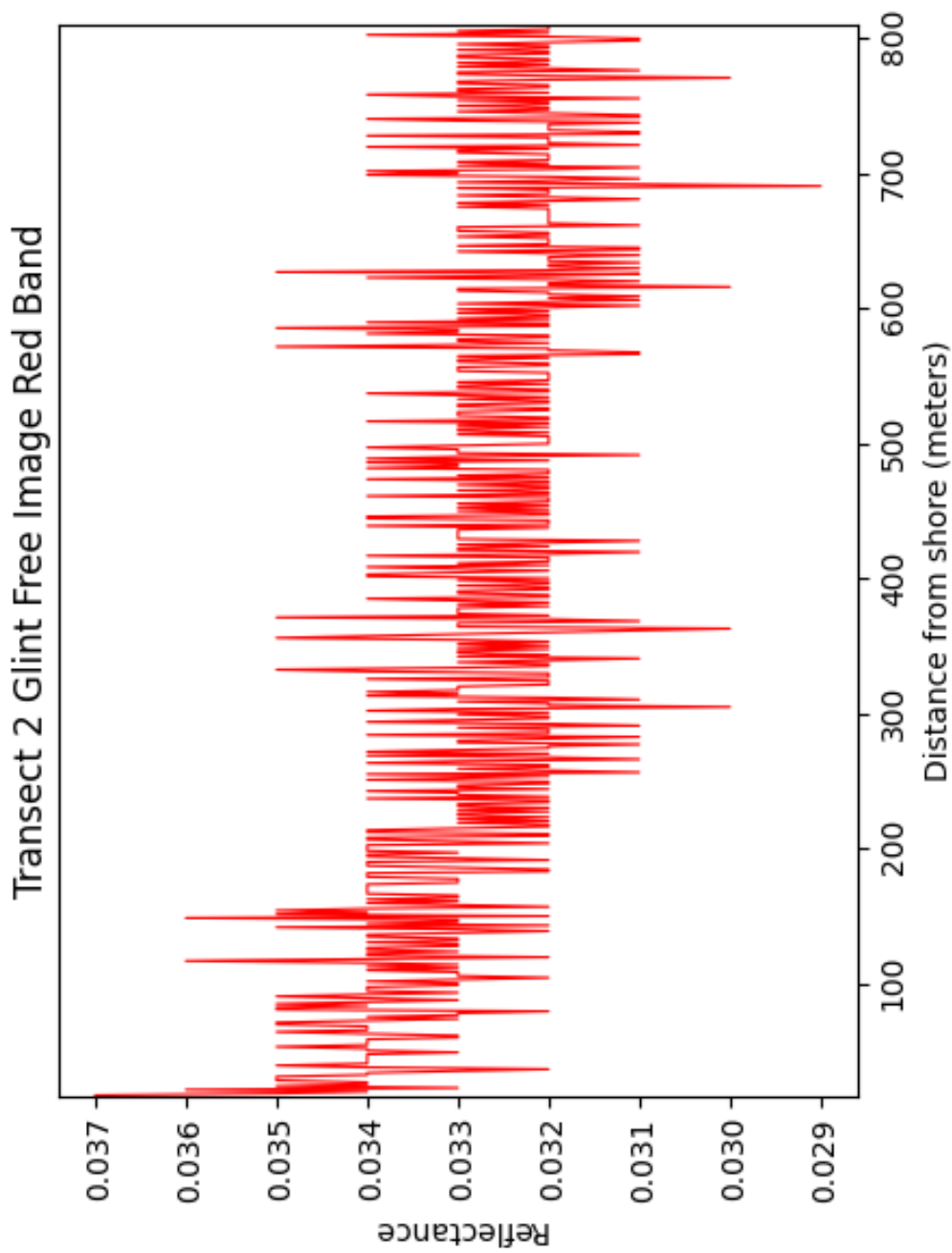


Figure 3.19: Transect 2 from the multispectral glint free image as shown in Figure 3.14. Image taken on 8/28/2014 at 16:02:05.310569 UTC using the red band (660 nm). X-axis starting value represents the beginning of transect 2 on the lagoon side shore.

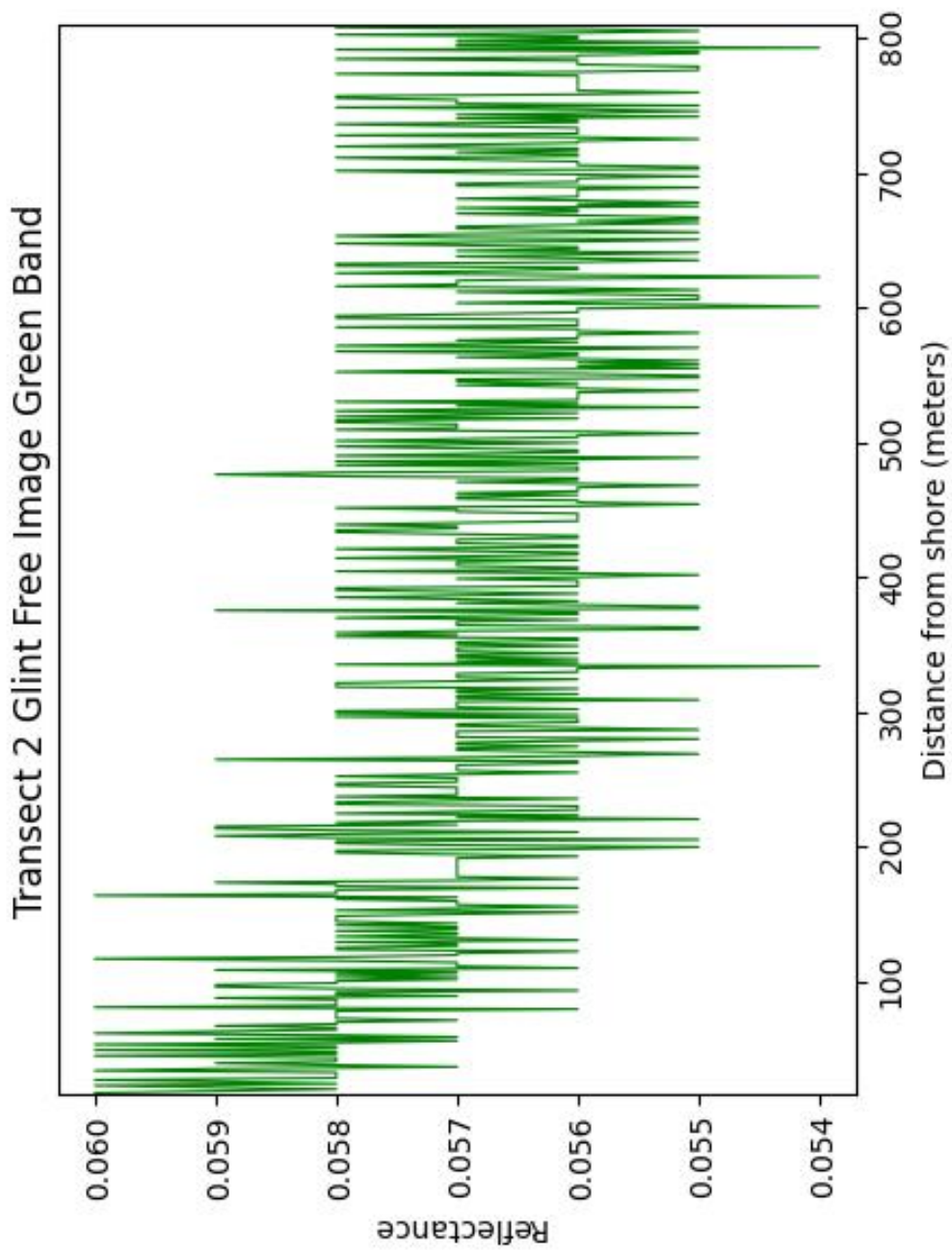


Figure 3.20: Transect 2 from the multispectral glint free image as shown in Figure 3.14. Image taken on 8/28/2014 at 16:02:05.310569 UTC using the green band (545 nm). X-axis starting value represents the beginning of transect 2 on the lagoon side shore.

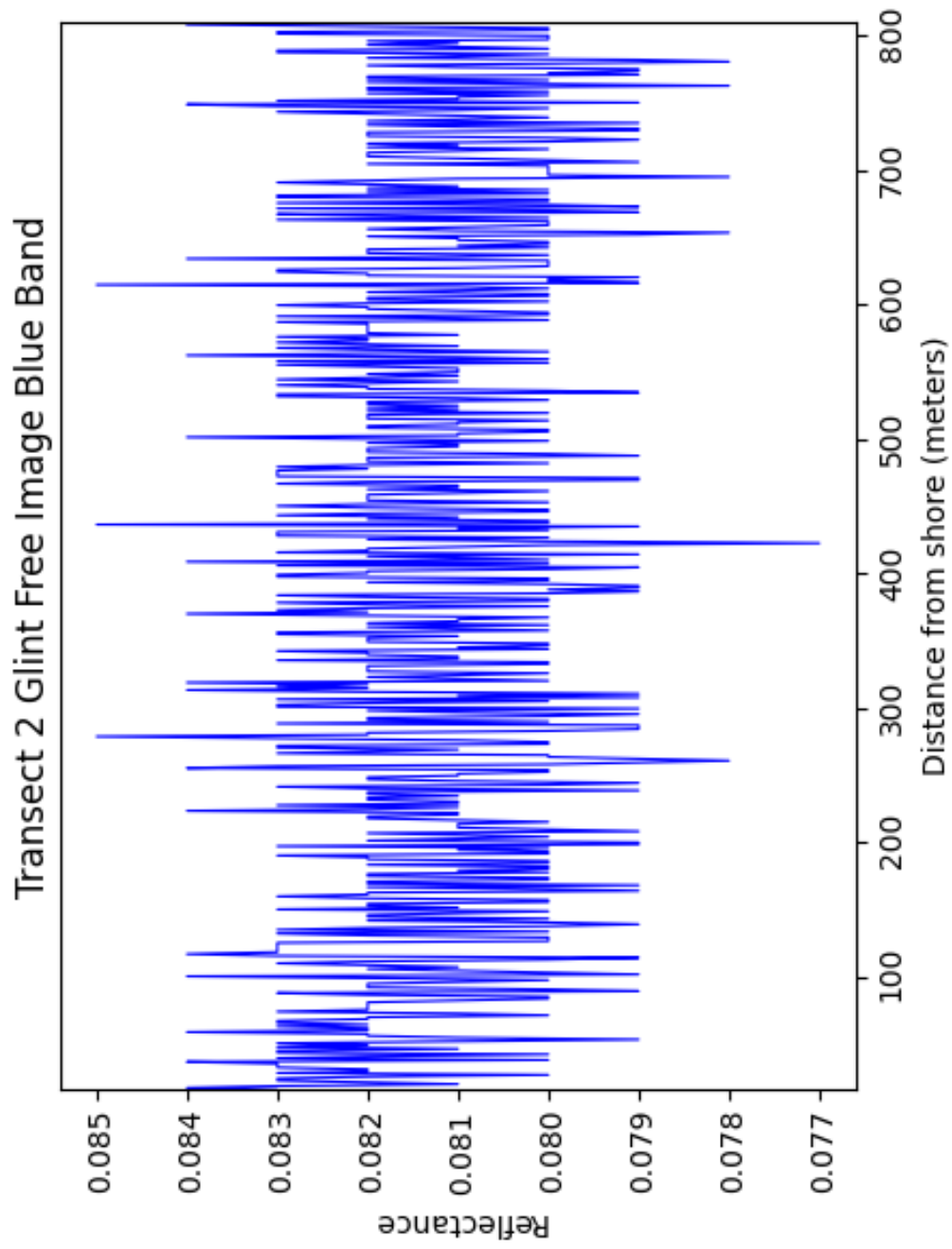


Figure 3.21: Transect 2 from the multispectral glint free image as shown in Figure 3.14. Image taken on 8/28/2014 at 16:02:05.310569 UTC using the blue band (480 nm). X-axis starting value represents the beginning of transect 2 on the lagoon side shore.

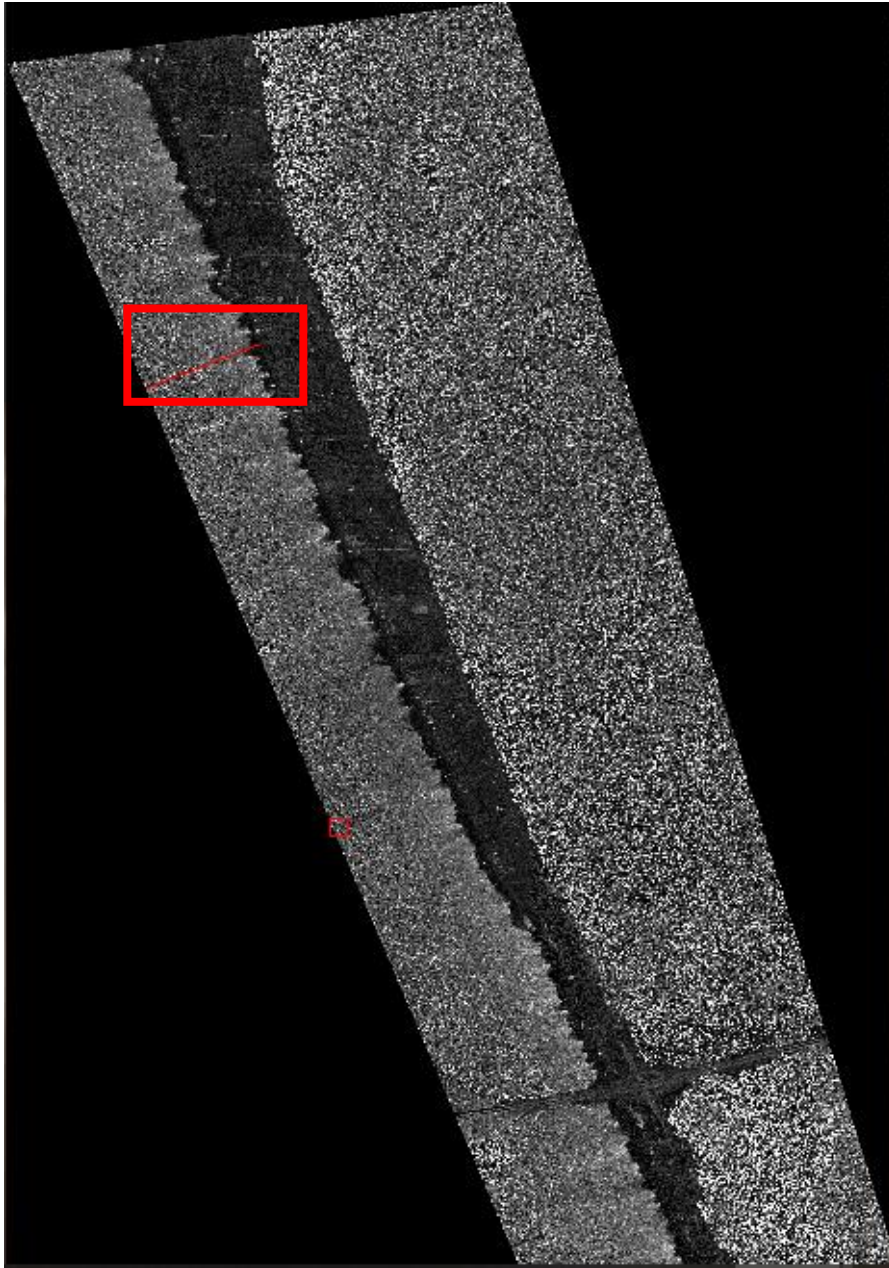


Figure 3.22: Transect 2 panchromatic band glint contaminated image transect shown by red box.

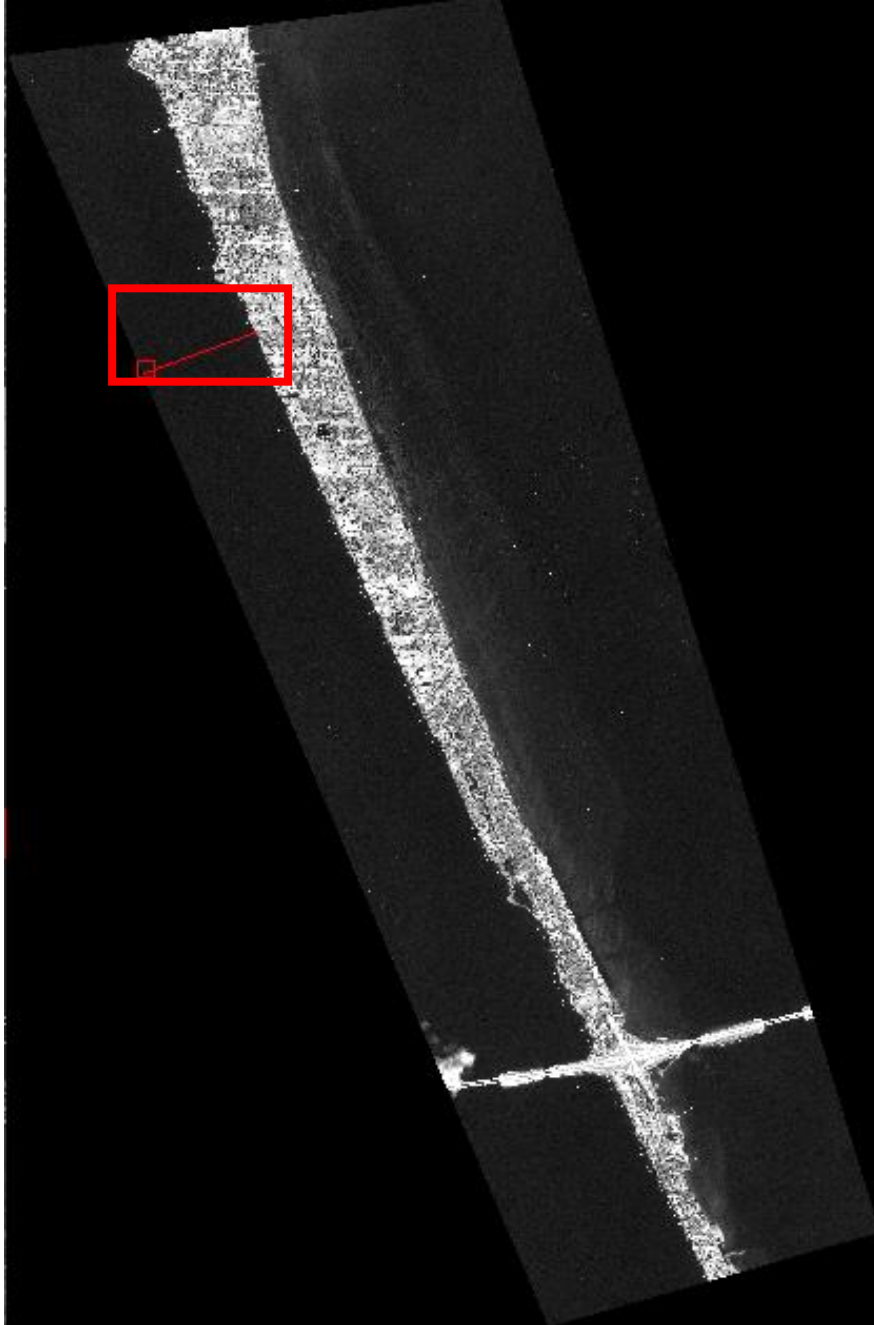


Figure 3.23: Transect 2 panchromatic glint free image transect shown by red box.

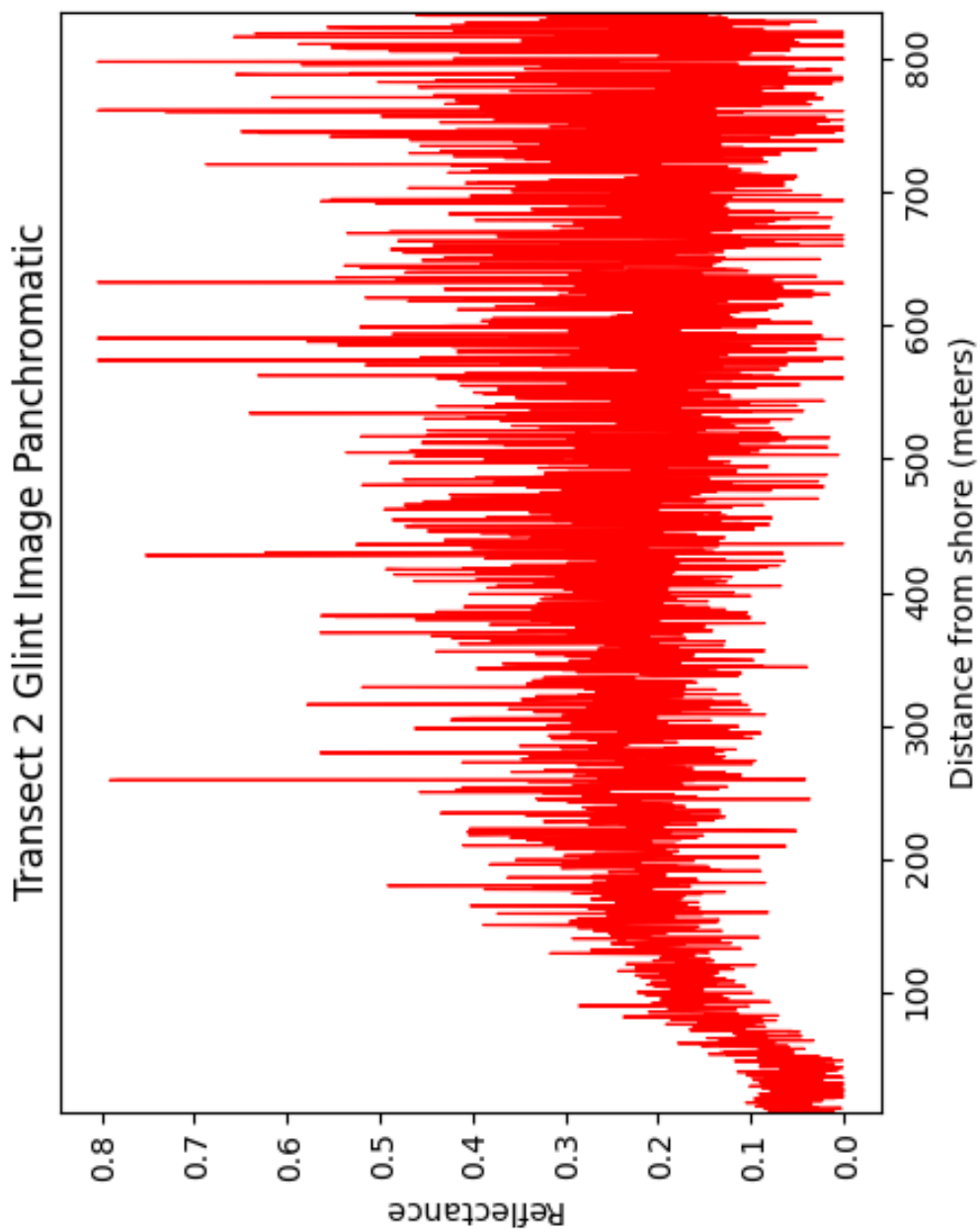


Figure 3.24: Transect 2 from the panchromatic glint contaminated image as shown in Figure 3.22. Image taken on 8/28/2014 at 16:01:02.5516 UTC. X-axis starting value represents the beginning of transect 2 on the lagoon side shore.

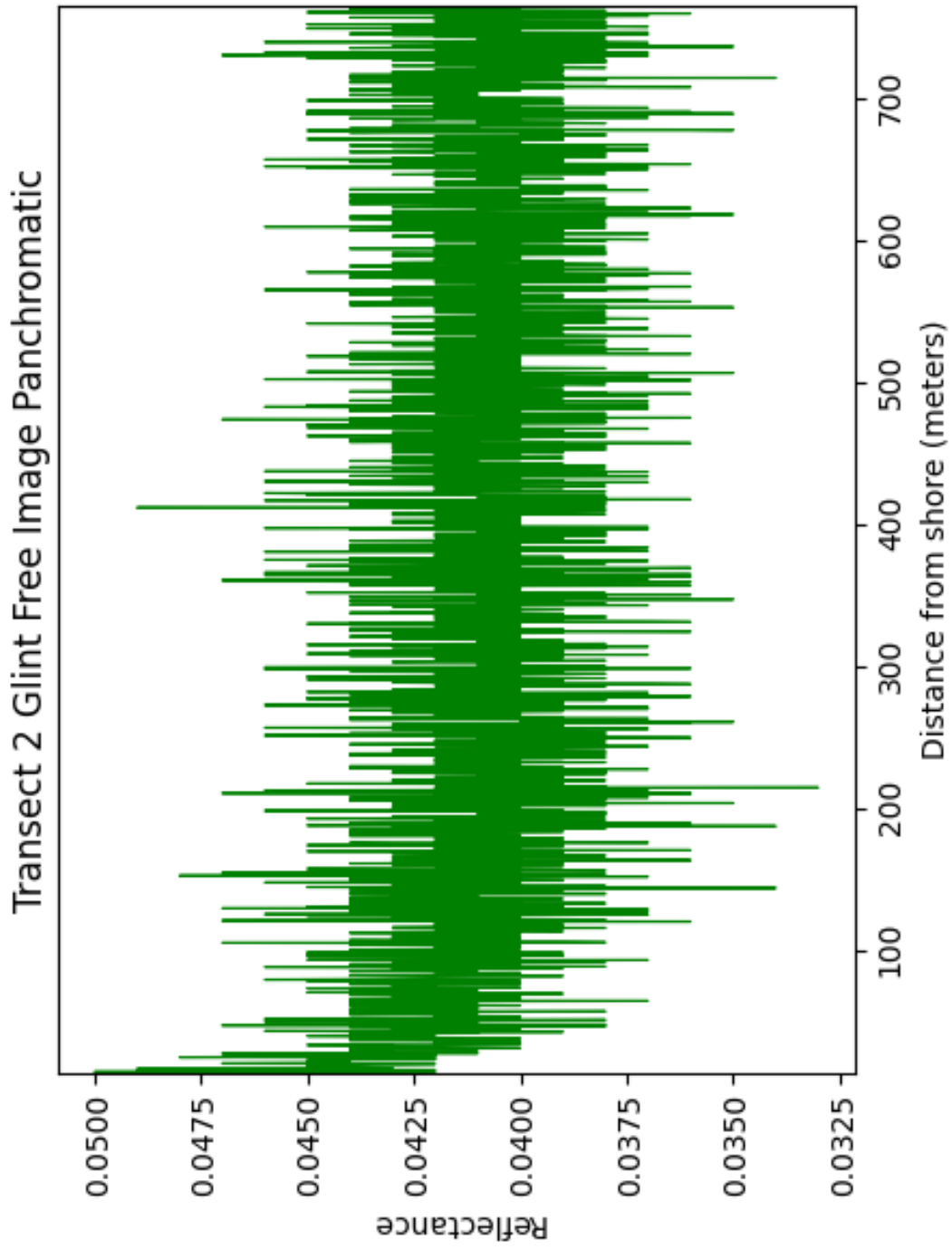


Figure 3.25: Transect 2 from the panchromatic glint free image as shown in Figure 3.23. Image taken on 8/28/2014 at 16:02:05.310569 UTC. X-axis starting value represents the beginning of transect 2 on the lagoon side shore.

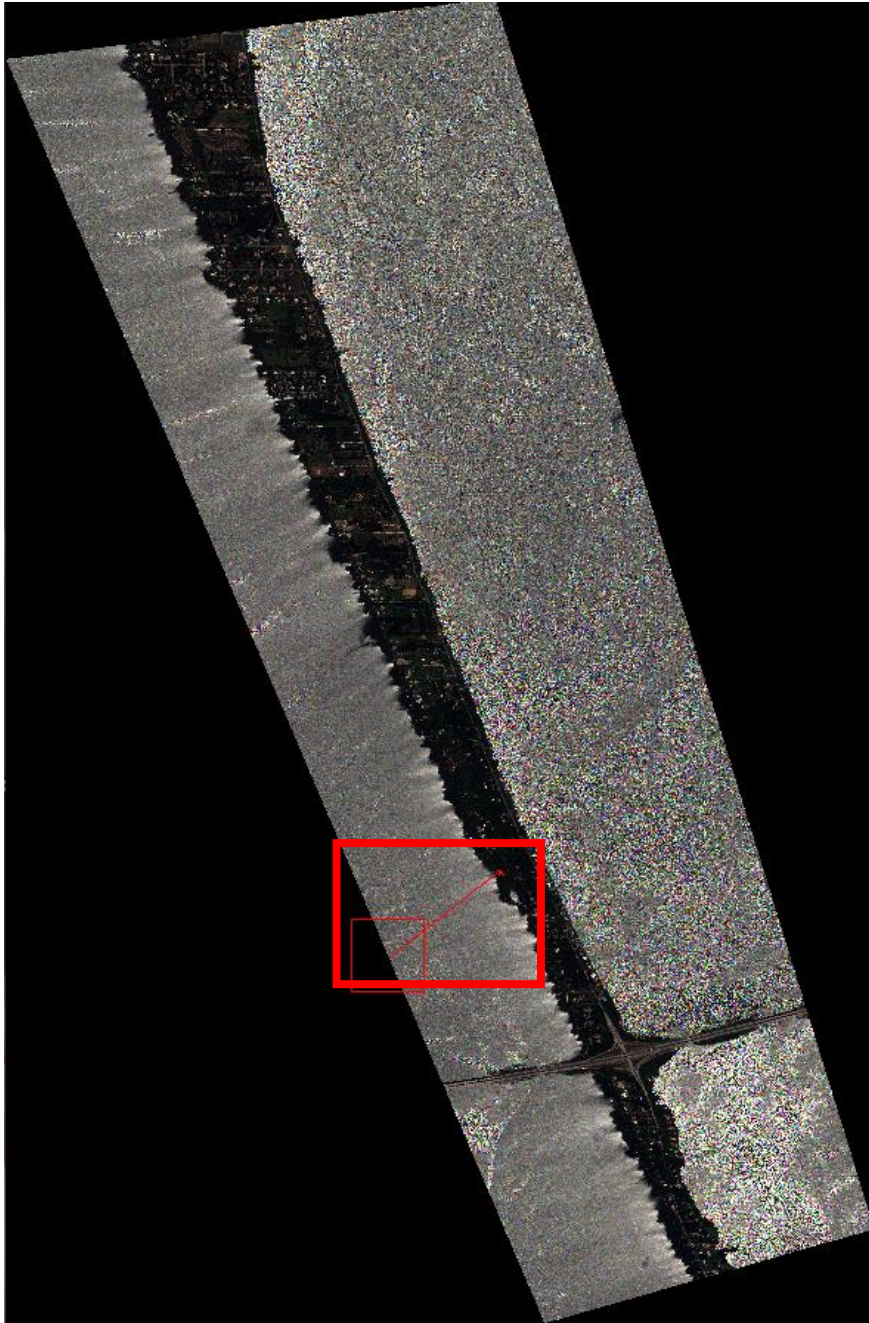


Figure 3.26: Transect 3 multispectral glint image shown in the red box.



Figure 3.27: Transect 3 multispectral glint-free image shown in the red box.

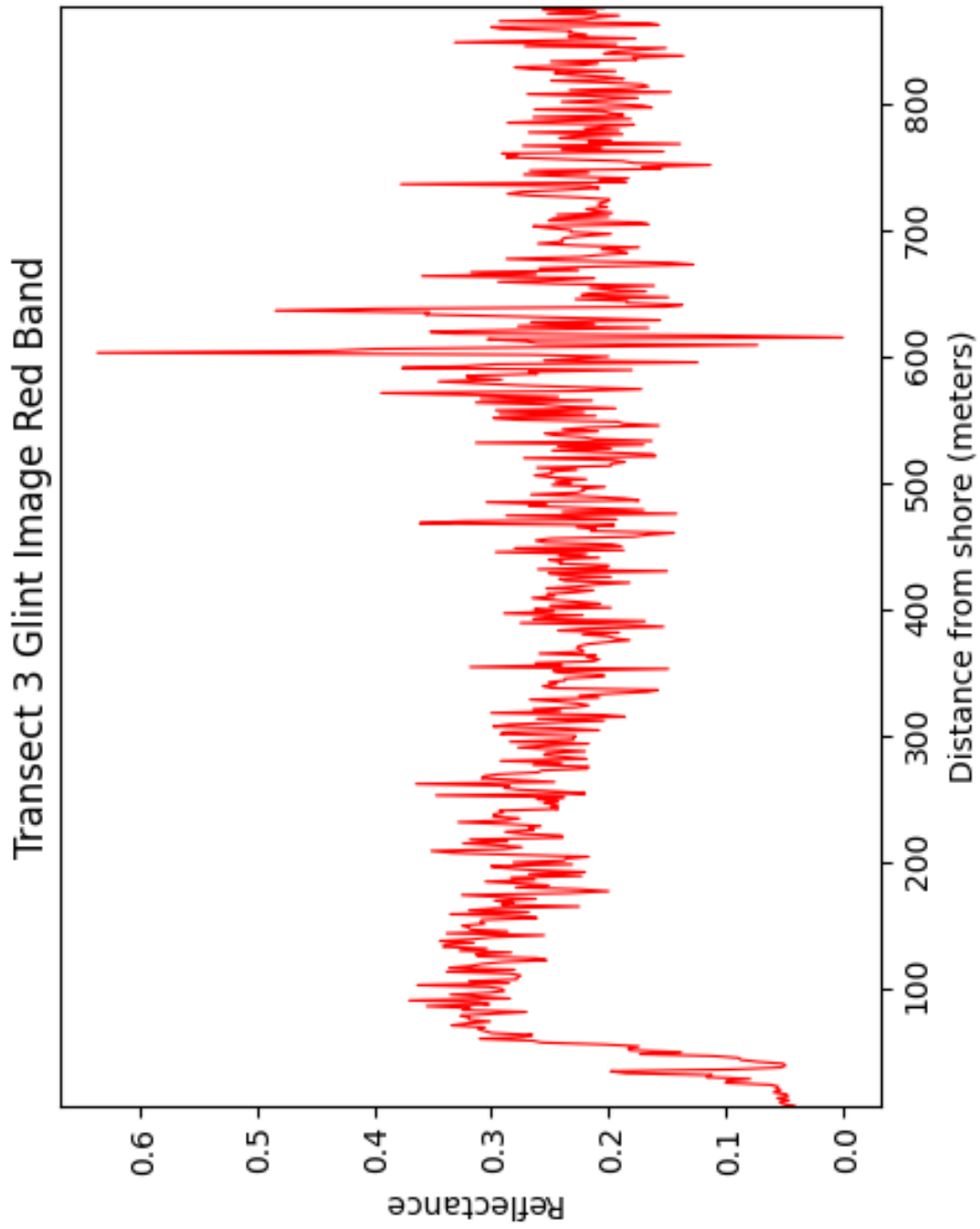


Figure 3.28: Transect 3 from the multispectral glint image as shown in Figure 3.26. Image taken on 8/28/2014 at 16:01:02.5516 UTC. X-axis starting value represents the beginning of transect 3 on the lagoon side shore.

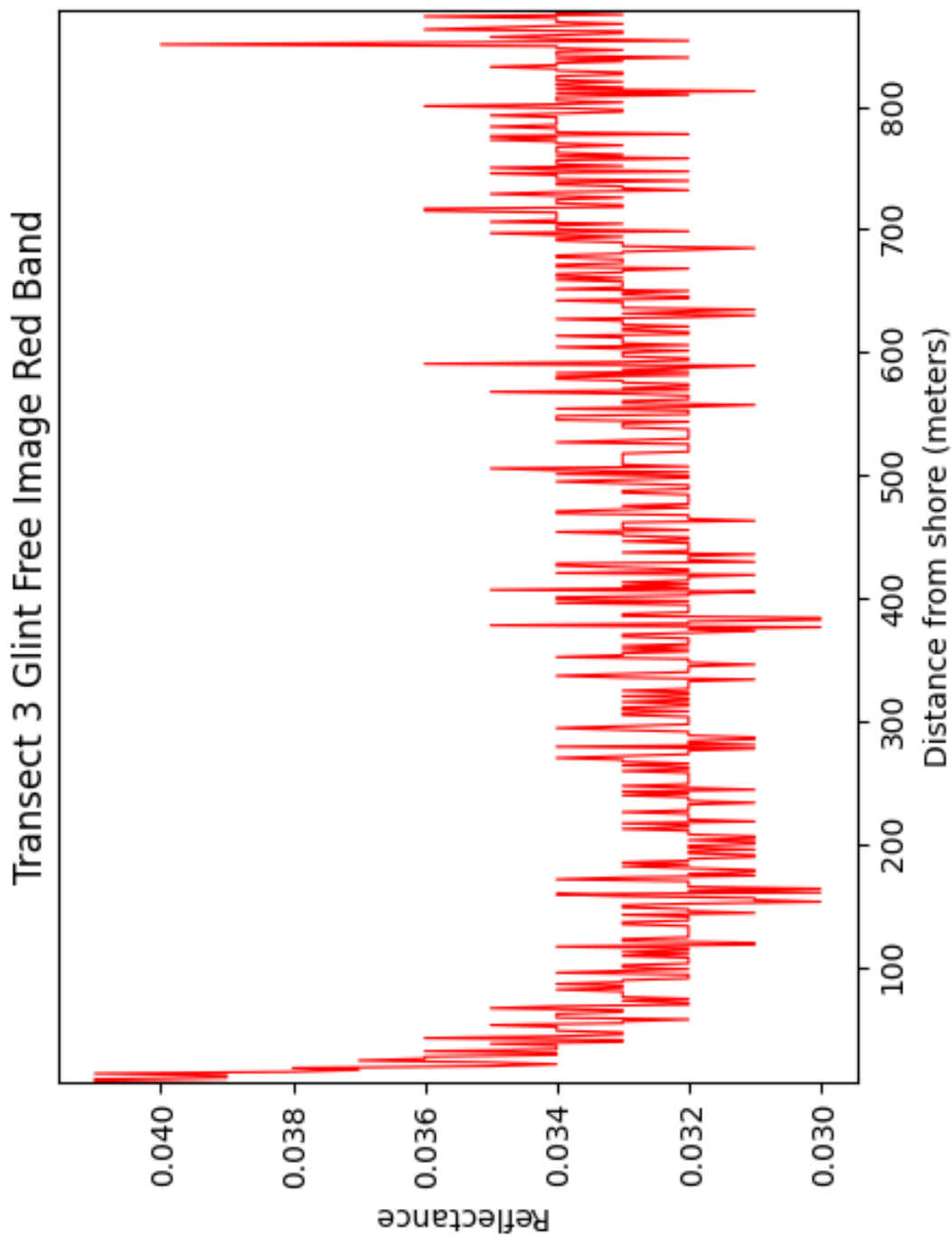


Figure 3.29: Transect 3 from the multispectral glint free image as shown in Figure 3.26. Image taken on 8/28/2014 at 16:02:05.310569 UTC. X-axis starting value represents the beginning of transect 3 on the lagoon side shore.



Figure 3.30: Transect 3 panchromatic glint image shown in the red box.

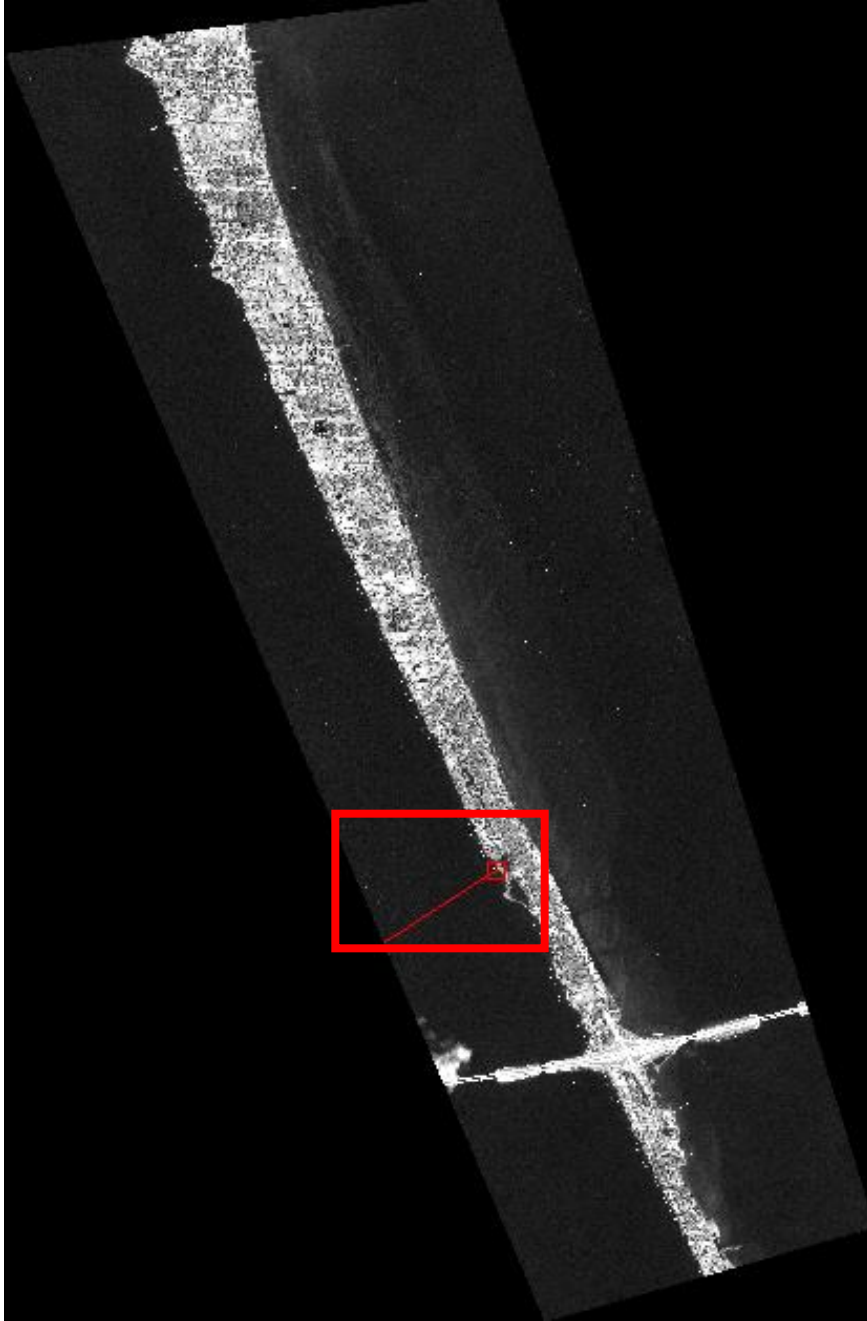


Figure 3.31: Transect 3 panchromatic non-glint image shown in the red box.

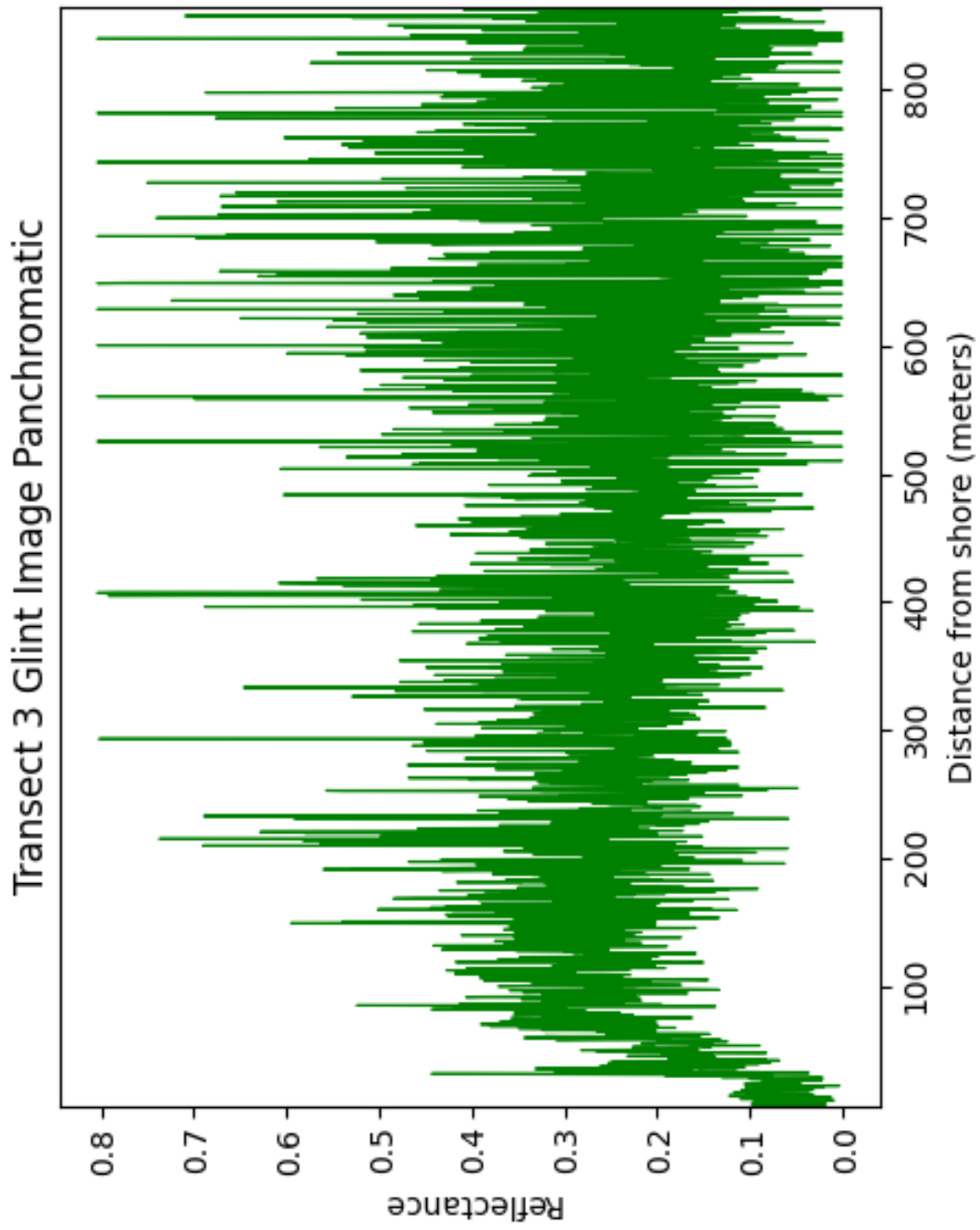


Figure 3.32: Transect 3 from the panchromatic glint image as shown in Figure 3.30. Image taken on 8/28/2014 at 16:01:02.5516 UTC. X-axis starting value represents the beginning of transect 3 on the lagoon side shore.

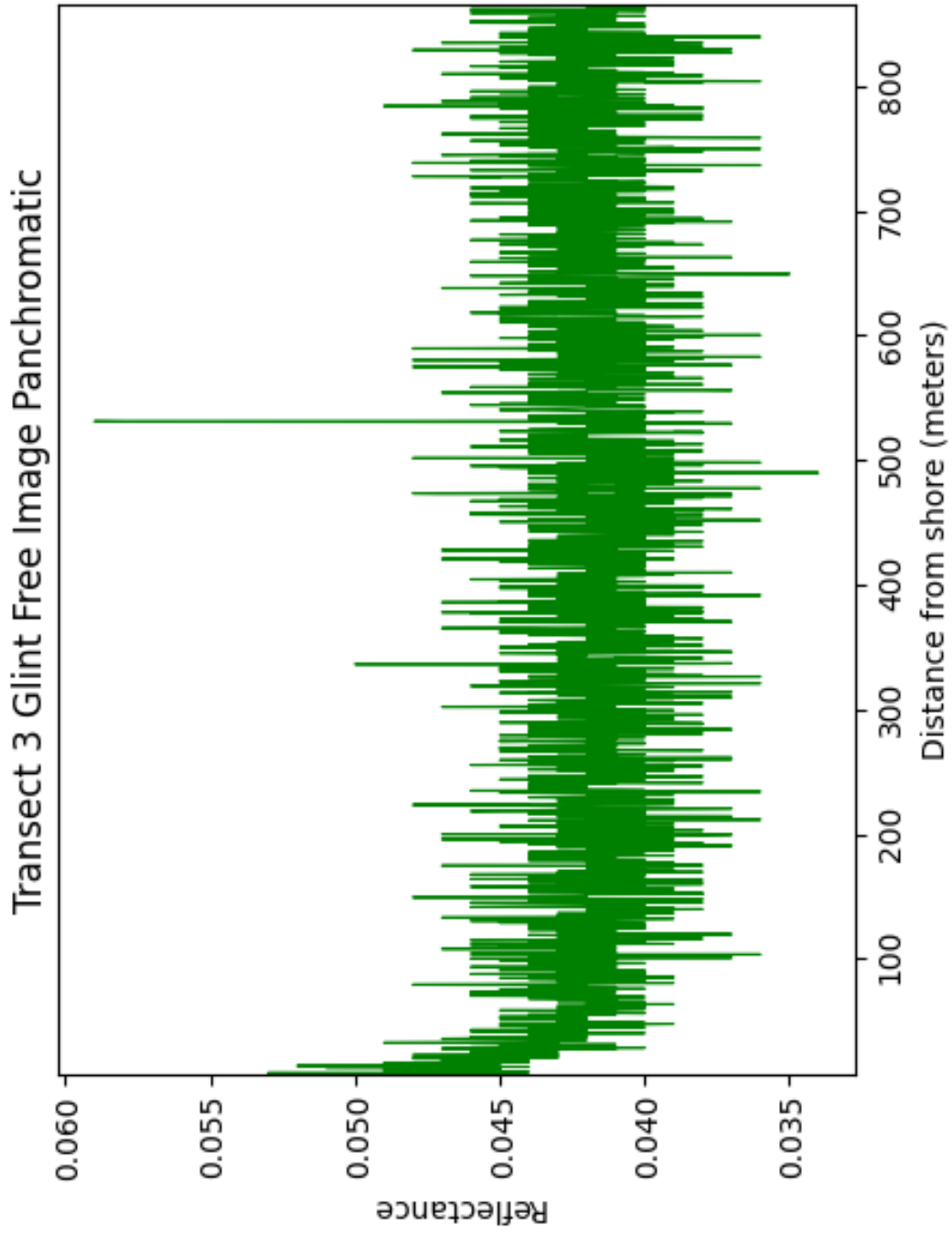


Figure 3.33: Transect 3 from the panchromatic glint image as shown in Figure 3.31. Image taken on 8/28/2014 at 16:02:05.310569 UTC. X-axis starting value represents the beginning of transect 3 on the lagoon side shore.

The plots were created by taking reflectance values for each pixel in a given transect from ENVI on the y axis and plotting them against the pixels corresponding estimated distance from the shore. This distance from shore estimation was calculated by using ENVI's measurement tool to measure both the distance from the shore to the first pixel in the transect and the length of the full transect in meters. Then, to give an approximation for each individual pixels distance from shore, the number of pixels in the transect was divided by the total distance in meters. A column of pixel numbers (starting at 0) was then multiplied by this value and the initial distance from shore to the starting pixel was added. This method, although not perfectly accurate, gives an adequate approximation of each pixels distance from the shore.

3.3 Linearization of Logistic Growth Model

It is apparent by examining the transects of reflectance by fetch distance that they follow a logistic growth curve. Linearization of the logistic growth

function allows one to easily fit the linearized form and estimate parameters. In order to linearize a logistic growth function, the following steps are used.

Starting with the general form of the logistic growth function from equation 2.8, it can be rearranged into a linear version of itself.

$$R = \frac{K}{1 + e^{-rt - C}} \quad 3.1$$

This can be rearranged to:

$$\ln \left[\frac{K - R}{R} \right] = -rt - C \quad 3.2$$

In order to apply this to the data, the values for the y axis of the linearized version were created in Excel, by using the formula $\ln \left[\frac{K-R}{R} \right]$, where K is the maximum value the reflectance values could reach (theoretically equals 1, but in practice is usually much lower for the transects used) and R is the respective reflectance value for each pixels iteration. The x axis is kept the same as distance in meters. Completing this linearization allows the logistic curve function data to undergo a regression and have a fit line produced with estimates for the coefficients necessary using Systat, which is unable to produce fit lines for equations that are more complex such as the original logistic growth equation. Equation 3.2 is merely a starting point for a fit equation solution, however, and the exact form of the right-

hand side of the equation is altered as necessary to provide the most accurate fit line for the glint patterns of the transects used.

Once this optimal fit line is found through trial and error, the values of the coefficients that Systat estimated can be used to produce a final fit of the original unaltered logistic curve reflectance data. This process is done for the residuals between the glint and non-glint image transect values, following which the unaltered residual reflectance values are compared to the logistic curve fit line produced using the coefficient values estimated by Systat. These values can be slightly modified until the fit line is as accurate as possible and final coefficient values are determined for the residual transect. With these final values input to the original logistic equation, the modeled correction values to be subtracted from each glint image pixel can be created and used. The “corrected” reflectances can then be compared to the non-glint reflectances to assess the quality of the correction. Finally, these coefficients can be related to different known glint inducing factor values from table 3.1 to estimate the final composition of the model parameters.

3.4 Parameters for Creating Model

Once the optimal fit and subsequent equation have been found, parameters that are known to influence glint can be mapped to the coefficients produced in the fit equation. A primary parameter for the level of glint in an image is the wind

speed and direction. These values were determined by examining historical weather data archives for Melbourne (Weather Underground). Figure 3.34 shows the measured wind speeds and directional vectors for the day on which the imagery was taken.

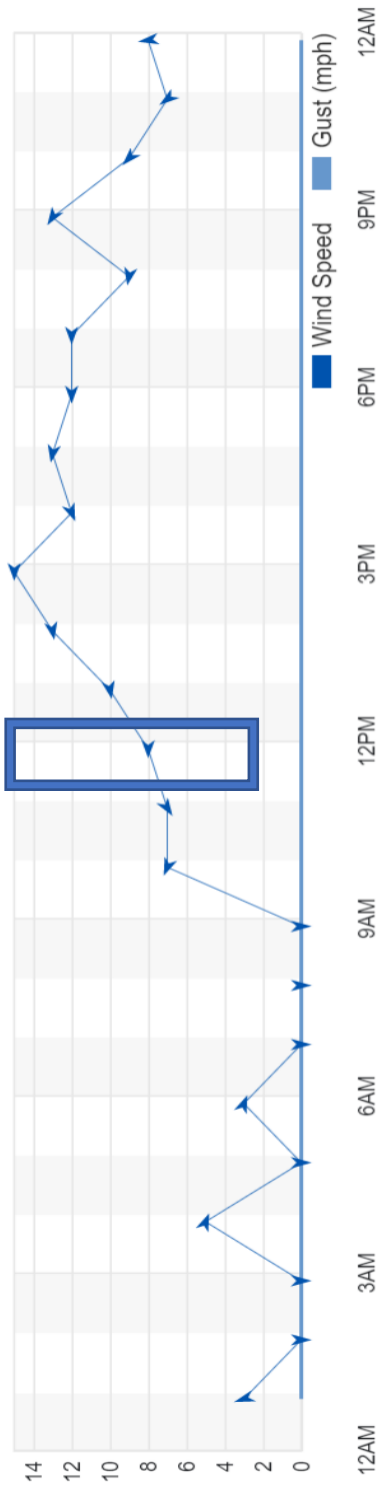


Figure 3.34: Wind speeds and directions for August 28, 2014 at approximately 11:53 am EST (15:53 UTC) from the wunderground historical weather data website. Blue box indicates the hour in which the WorldView-3 imagery was taken (Weather Underground).

The wind speed could then be estimated to around 8 mph (12.875 kilometers per hour) in an eastward direction (90 degrees) at the time the images were collected. This historical data was collected once every hour, the closest data point to the imagery (16:01 and 16:02 UTC) being at 15:53 UTC. This aligns with the wind direction apparent in the imagery based on visible wave direction. Based on the hourly data, the wind was blowing for around 2 hours in a similar direction with a similar wind speed prior to the imagery being collected. At 14:53 UTC, the wind was approximately 7 mph (11.265 km/hour) in an east-northeast direction. At 13:53 UTC, the wind was approximately 7 mph in an east-southeast direction. Prior to this, the wind was not blowing (0 mph) for 3 hours. If the eastward wind direction is taken to be 0 degrees on a coordinate plane for reference, the difference between the sensor azimuth angle (329.9 degrees) and the wind direction would be about 31 degrees.

	Glint Image	Non-Glint Image	Difference
Solar azimuth	129.5 °	129.9°	0.4°
Solar elevation angle	63.2 °	63.3°	0.1°
Satellite azimuth angle	329.9°	221.5°	108.4°
Satellite elevation angle	68.6°	60.4°	8.2°
Across track viewing angle	-12.8°	-14.9°	2.1°
In track viewing angle	14.9°	-22.4°	37.3°
Off nadir viewing angle	19.6°	26.6°	7°
Wind speed	12.875 km/hour	12.875 km/hour	-
Wind direction	E (90°)	E (90°)	-
Difference between sensor azimuth and wind direction	30.1°	138.5°	-
Time wind was blowing in the same direction	~2 hours in an eastern direction (7200 sec)	~2 hours in an eastern direction	-

Table 3.1: Possible values that could contribute to glint for consideration when evaluating fit equation coefficients.

Taking all of these values into account, an estimation of what parameters fit into the equation coefficients can be found. This estimation will not be perfect, but it can get close to estimating what factors are inducing the presence of glint in these images. First, a dimensional analysis is done on the linear fit equation to understand which parameters will work when input into different parts of the equation by determining what their units must be. The left-hand side of the equation, $\ln \left[\frac{K-N}{N} \right]$,

is comprised of only reflectance values and is therefore dimensionless. This implies that the right-hand side of the equation must also produce a dimensionless result. This side of the equation, $-rt - C$, has the t component, which is a distance. This implies the necessity of an inverse length component in the r term to cancel out and arrive at a dimensionless result. This information allows for the narrowing down of which glint inducing parameter values can be considered as components for the r and C terms of the equation (as well as any other coefficients added during the Systat linear estimation). Once the best estimations for which terms make up the coefficients in the equation are found, the final model is ready and can be tested on other transects within the image for accuracy.

Knowing that the r term in the equation must have an inverse distance component indicates that it must include one of the terms in Table 3.1 that includes distance. The only term with a distance component would be the wind speed, and if the inverse wind speed is used it would then satisfy the inverse distance requirement. Using the inverse wind speed would produce units of $\frac{time}{distance}$, which now creates the necessity of a $\frac{1}{time}$ term in r as well. A possibility for this term based on Table 3.1 could be the inverse of the time the wind has been blowing in the same direction, which was estimated at around 2 hours but is most likely a slightly different value. Not knowing the exact value to use for this term allows for some flexibility in the final value for r produced using values from Table 3.1. The

values used for the r term were all normalized to units of meters and seconds. With these values added in, an additional non-dimensional term was necessary to produce a final value for r that matched what the model produced. Further discussion of the final terms used is given in section 4.1. This criterion was also used when determining terms for the c and a coefficients, trial and error was performed using values that make the most logical sense to contribute to each term until a value close to the model coefficient was produced. Final values with their designated components and units are shown in section 4.1.

3.5 Methods for testing model correction accuracy

After a final model was produced, various methods were used to test the accuracy of the model. The model was first tested on various transects from different parts of the image to provide variability. To test the model on these transects, the residuals between the glint and non-glint images were calculated for each transect. These were then plotted with the model estimated residuals to compare similarity. The “corrected” reflectance values were then calculated by subtracting the model residual reflectance values from the glint image reflectance values for each transect. These were plotted with the glint and non-glint transect reflectances for comparison.

A visual correction was also attempted on a region of interest (ROI) within the glint image to test the model results visible to the eye. In order to do this, an ideal ROI was selected using ENVI's ROI creation tool and Subset Data via ROIs tool. To allow for incorporation of the distance from shore component, an ASCII file of each pixels approximate distance from the shore was created using a python script written to create ASCII files using a table of values. In order to estimate these distances, an ROI whose right edge was parallel to the shoreline was selected and the distance from the shore to the first pixel in the ROI was measured using ENVI's measurement tool. This value was then used as the last distance from shore value for every row of pixels in the table. Starting from this ending value, 1.24 meters were added for each new pixel in a row until the left edge of the ROI was reached. The dimensions of the ROI were obtained for this by examining the image header file. Once this ASCII file was finished and created, it was added into ENVI, allowing it to be input to the band math tool. In order to perform the band math, the final equation of the model, which estimates the residual reflectances between glint and non-glint images (what needs to be removed), was subtracted from the glint image reflectances. This produced a model corrected ROI which could then be used to evaluate the accuracy of the correction performed. A few statistical metrics and the average percent of glint corrected were calculated to assess accuracy of the model using Systat's Basic Statistics tool.

3.6 Comparison to Hedley Glint Correction Method

In order to assess the quality of the correction model produced, it was compared to an existing glint correction method by Hedley (2005). Due to the shallow water conditions of the water in the imagery, a NIR based correction method such as Hedley's would be most appropriate (Kay, 2009). The Hedley correction method involves first selecting a sample area in the image in which the underlying signal from the pixels is expected to be relatively homogeneous and where a range of sun glint is present. Areas of the image containing the deepest water meet these criteria the best. Once a sample area is selected, the minimum Near Infrared (NIR) reflectance in the area must be determined. Then a linear regression must be performed between the NIR pixel values of the sample area and the visible bands corresponding pixel values. If using multispectral imagery, this can be repeated for various bands individually to create a final image. After completing the regression, the slope of this regression line must be determined. To finalize the process of deglinting the imagery, the band math tool in ENVI is used to apply the Hedley correction equation to each pixel, utilizing the slope of the regression line calculated (b_i), the NIR reflectance of each pixel in question (R_{NIR}), the minimum NIR reflectance value for the sample area (Min_{NIR}), and the

visible bands reflectance of each pixel in question (R_i). This is represented in equation 3.3 from Hedley (2005).

$$R_i' = R_i - b_i(R_{NIR} - Min_{NIR}) \quad 3.3$$

For this correction, the glint free image is regarded as the ideal final “corrected” outcome, and the glint image is regarded as the raw image that has a correction performed on it. To perform the Hedley correction, first a region of interest was chosen that matched the necessary criteria. By linking and comparing the glint contaminated image to the glint free image, a region was selected where the glint was strong with variation and the underlying signal should be relatively homogenous. Figures 3.35-3.37 show the region of interest selected. Once selected, the NIR, blue, red, and green band reflectance values for the region were extracted and the minimum NIR reflectance value in the region was determined to be 0.0003. The linear regression was then performed using python to obtain the slope value needed for each band. The final equations were input into the ENVI band math tool for each band as shown in equations 3.4-3.6.

$$R_{red}' = R_{red} - 0.08143558(R_{NIR} - 0.0003) \quad 3.4$$

$$R_{blue}' = R_{blue} - 0.09085432(R_{NIR} - 0.0003) \quad 3.5$$

$$R_{green}' = R_{green} - 0.11694104(R_{NIR} - 0.0003) \quad 3.6$$

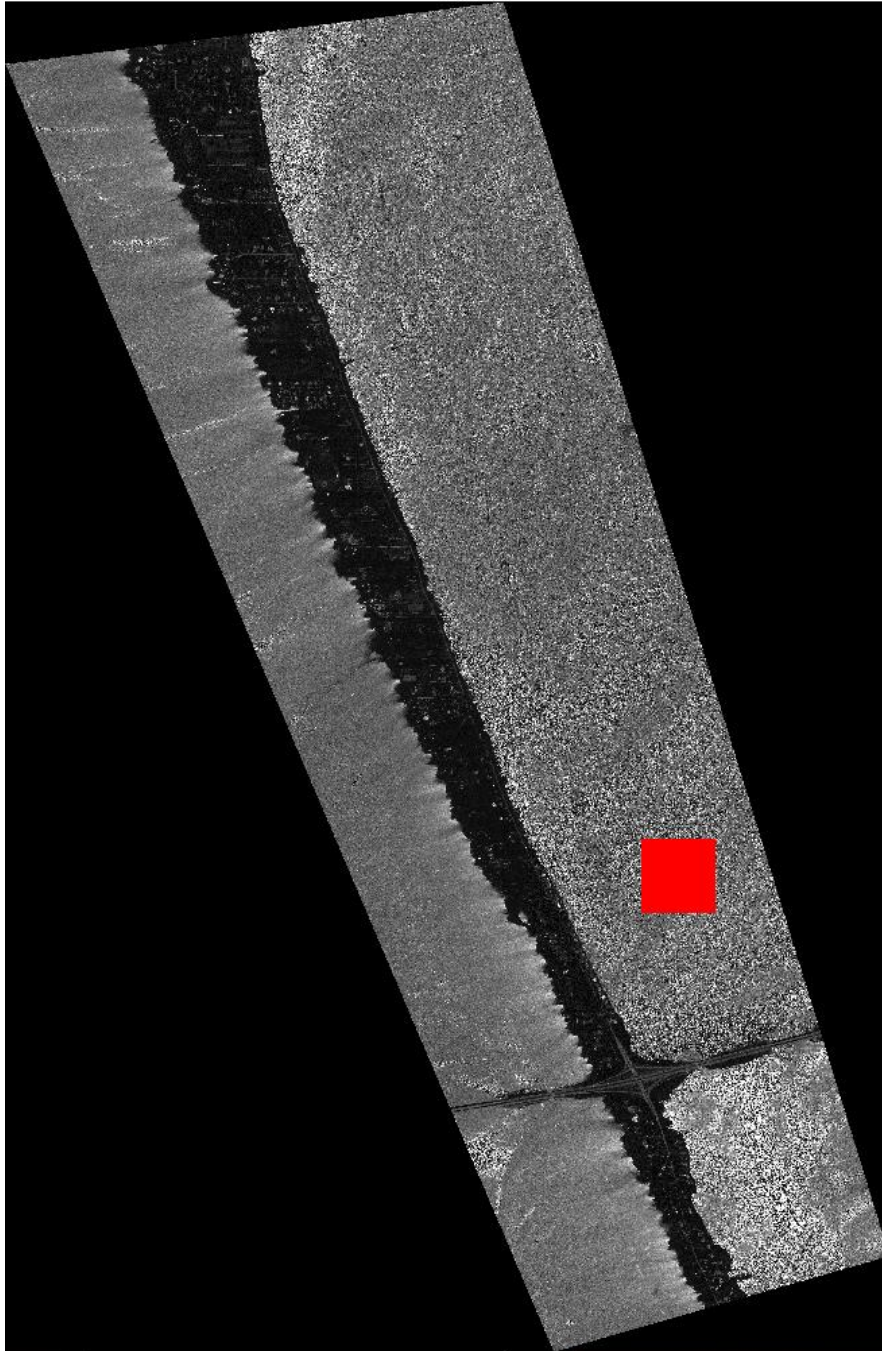


Figure 3.35: Glint contaminated image showing the region of interest used for Hedley correction in the red box.



Figure 3.36: Glint free image showing region of interest used for Hedley correction for reference.

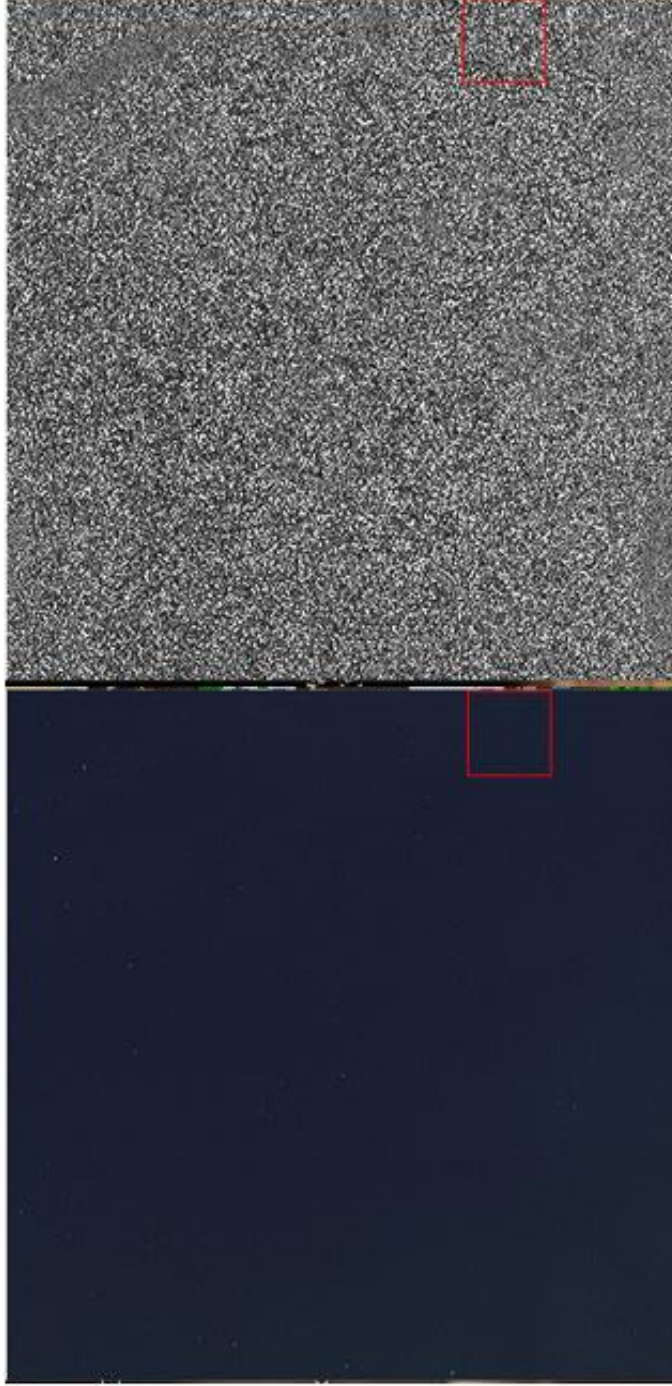


Figure 3.37: Area within the red boxes of figures 10 and 11 (region of interest) shown for reference. It is evident that this is an area of relatively deeper open water, very homogenous in the glint free image (left) but showing a varying amount of glint in the glint contaminated image (right).

Once the initial Hedley correction was performed on the region of interest, the resulting image and reflectance value changes were examined. Due to the relatively small change in reflectance produced, the results of the correction were scaled up by varying percentages. A scaling factor was introduced to the original Hedley equation used, shown in equations 3.7-3.9. By examining the equations used to produce the corrected reflectance values for each band, it is evident that the linear regression line slope term being relatively very small is what is causing the inadequate correction. Due to this value being small, the amount that is subtracted from the original reflectance value to “correct” the reflectance is very small. Therefore, the scaling factor is multiplied by the linear regression line slope term to produce the desired outcome.

$$R_{red}' = R_{red} - 0.08143558(2)(R_{NIR} - 0.0003) \quad 3.7$$

$$R_{blue}' = R_{blue} - 0.09085432(2)(R_{NIR} - 0.0003) \quad 3.8$$

$$R_{green}' = R_{green} - 0.11694104(2)(R_{NIR} - 0.0003) \quad 3.9$$

As the 100% increase still proved to produce an inadequate correction of the glint, a larger scale factor was introduced. This scale factor was calculated to be

the ideal value using a sample pixel from the Hedley corrected band values and the glint free image band values. The ideal corrected pixel value R_{red}' was taken from the glint free image, the uncorrected pixel value R_{red} was taken from the glint contaminated image, and the NIR pixel value was taken from the glint contaminated image as well. With these values from a specified pixel input to equation 3.3, the ideal scale factor was solved for, to be about 61, as seen in equation 3.10.

$$0.032 = 0.325 - 0.11694104(x)(0.041 - 0.0003) \quad 3.10$$

4. Results

4.1 Model Parameter Results

The residuals of transect 2 shown in figures 3.15-3.25 were used to produce an initial version of the model. After the linearization was applied, these values were input to Systat and the Regression: Nonlinear: Estimate Model tool was used to fit the linearized y axis data to the x axis (distance) data as shown in Appendix B. Once the first iteration was completed, it was evident that the plot still had a nonlinear shape present, so the fit line required modification to accommodate for this. For the subsequent iterations, a new form of the equation was tested as seen in equation 4.1 to incorporate an exponential component. This produced an adequate fit, as seen in figure 4.1.

$$a + (r * c^{distance}) \quad 4.1$$

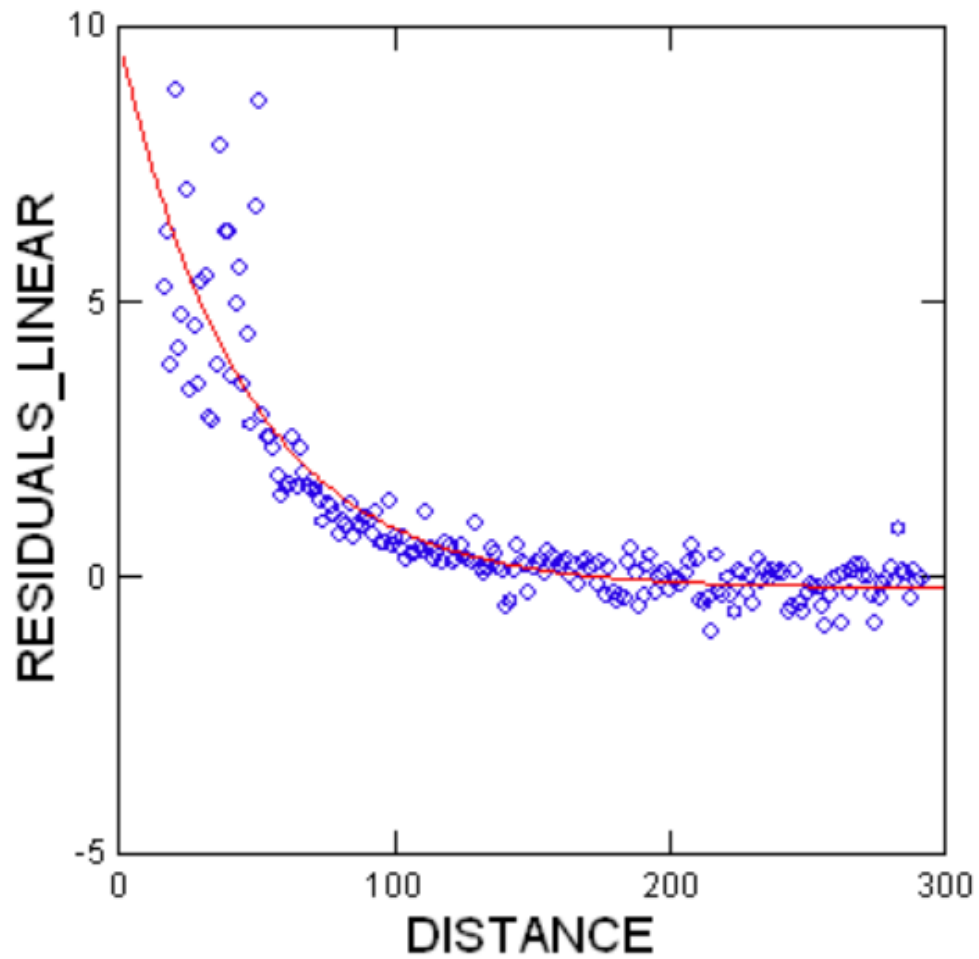


Figure 4.1: First transect multispectral blue band residuals (glint image minus non-glint image) linearized. The nonlinear regression estimate model was run using equation 4.1. An estimated value of .978 for c was used; a and r were estimated by the model. This estimated c value was obtained through trial and error.

The estimated parameters for various iterations were as follows. Values labeled as given were estimated after trial and error and input to the model tool before running. Values labeled as estimated were estimated by the model tool using the equation and values given. The number of iterations was increased to 200 to allow for better estimation of coefficient values.

First Transect	
Equation	$a + (r * c^{distance})$
a	-0.192 (estimated)
r	9.966 (estimated)
a estimated range	-0.329 to -0.054
r estimated range	9.283 to 10.65
c	.978 (given)
R²	0.848

Table 4.1: Estimated and given coefficient values for the final and most accurate iteration of the estimate model.

The final coefficients determined as shown in Table 4.1 were then put into the original logistic equation, which was modified to accommodate for the new coefficients. The final version of the linearized equation is shown in equation 4.2,

which was then transformed back into the original logistic equation form as shown in equation 4.3.

$$\ln \left[\frac{K - N}{N} \right] = a + (r * c^{distance}) \quad 4.2$$

$$N_t = \frac{K}{1 + e^{a+(r*c^{distance})}} \quad 4.3$$

This logistic fit line with Systat estimated coefficient values was plotted along with the original unaltered reflectance values of the first transect. The similarity of these were estimated by eye and the values of a, r, and c were adjusted until the best fit was achieved using Excel. The final coefficient values determined for this transect are shown in Table 4.2.

Final Coefficients for Transect 1	
a	-0.244
r	8.453
c	0.978
Final fit equation	$N_t = \frac{0.25}{1 + e^{-0.244 + (8.453 * 0.978 \text{distance})}}$

Table 4.2: Final coefficients determined by examining the fit line and glint reflectance data in Microsoft Excel.

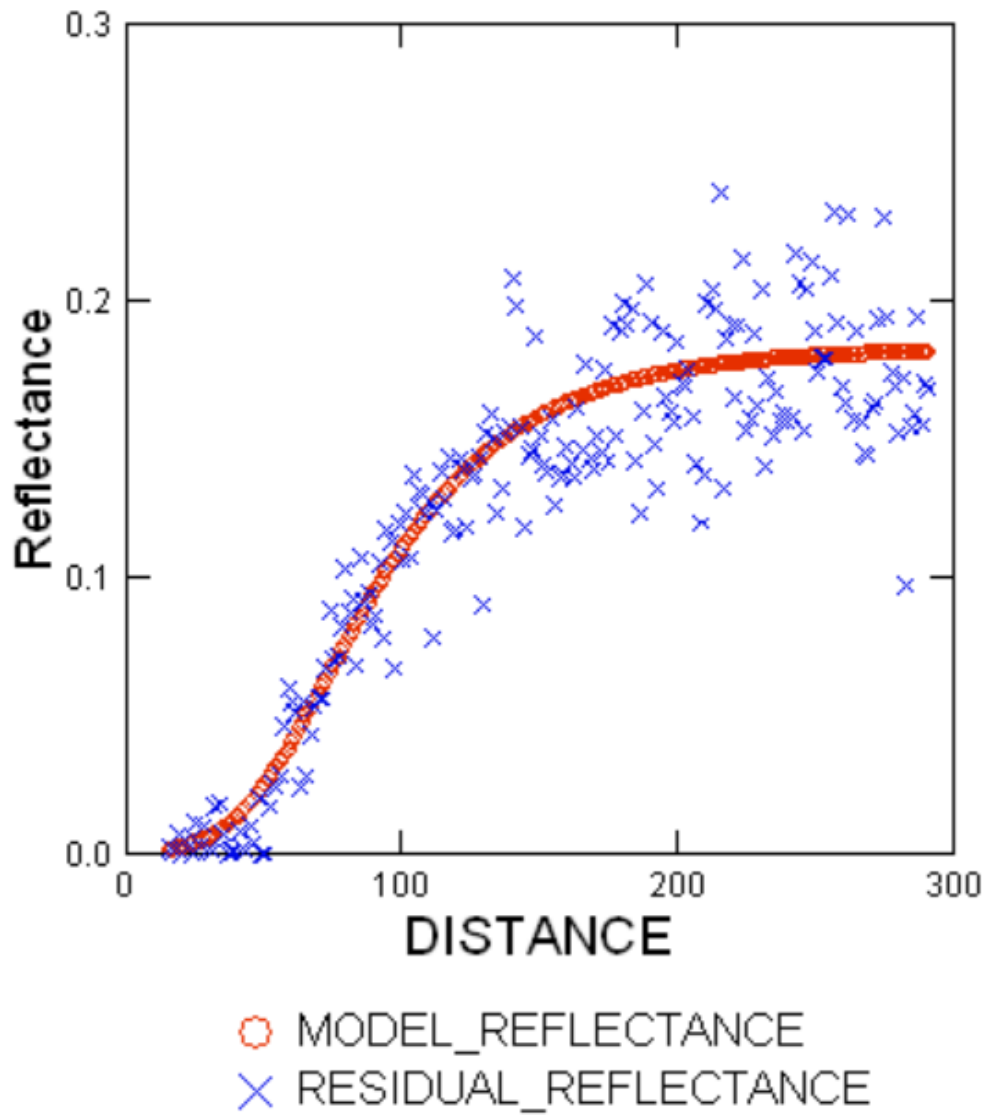


Figure 4.2: First transect residual reflectance compared to the modeled residual reflectance created using coefficients estimated from Systat.

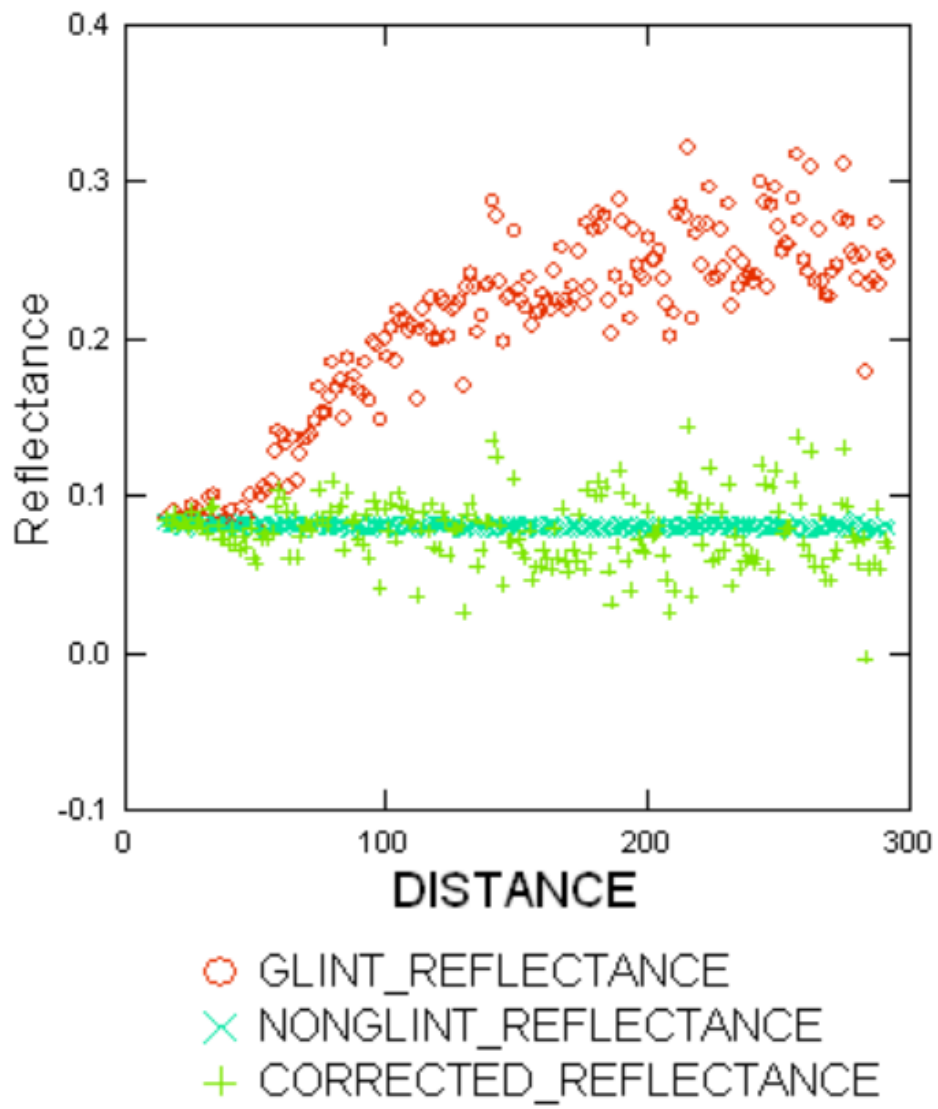


Figure 4.3: First transect glint and non-glint image reflectance compared to the model corrected reflectance values.

As seen in Figure 4.4, the model correction does remove a significant amount of the glint present, but there is still noise left in the signal. A second transect was also selected to produce varying model results that could be compared with the initial model created. This second transect showed a sharper increase and flattening than the first transect, producing varying coefficient values. The process of linearizing the transect reflectance values in order to fit the values using Systat was repeated. The final best fit coefficient values determined using Systat are shown in Table 4.2.

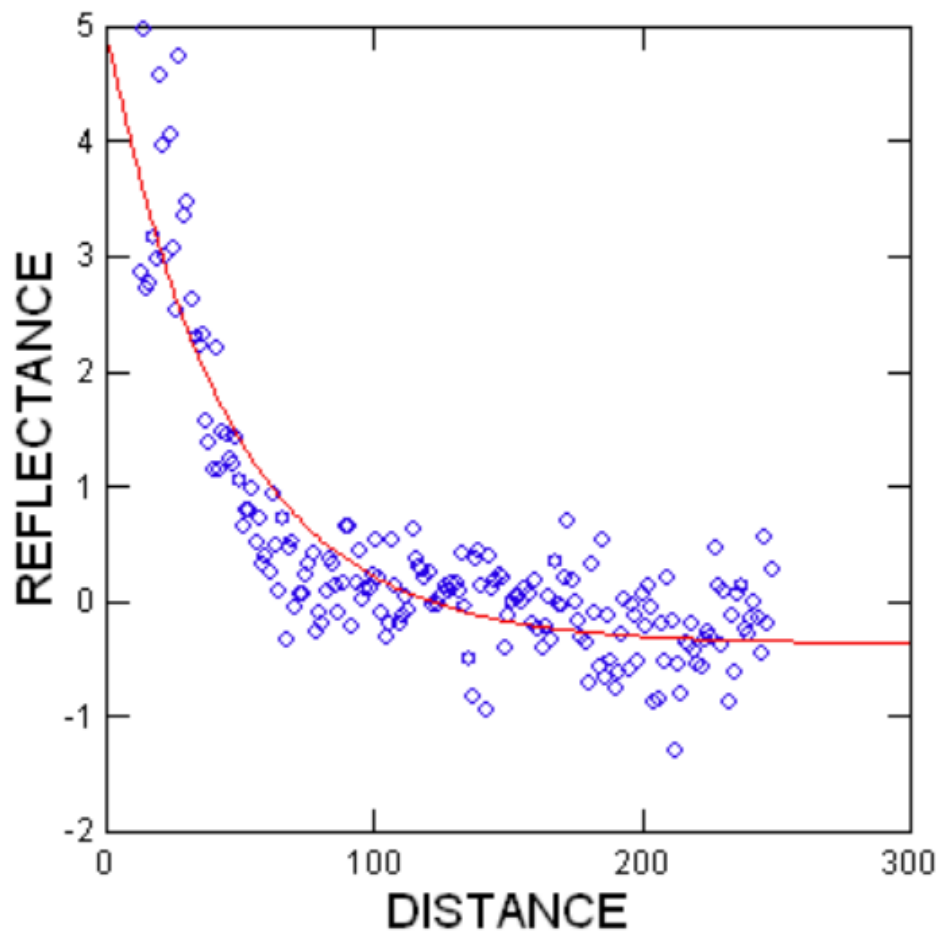


Figure 4.4: Second transect multispectral blue band residuals (glint image minus non-glint image) linearized. The nonlinear regression estimate model was run using equation 4.1. An estimated value of .978 for c was used; a and r were estimated by the model.

Second Transect	
Equation	$a + (r * c^{distance})$
a	-0.367 (estimated)
r	5.366 (estimated)
a estimated range	-0.453 to -0.280
r estimated range	4.995 to 5.737
c	.978 (given)
R²	0.834

Table 4.3: Second transect parameters as estimated by Systat using the nonlinear estimate model tool.

After evaluating the fit of the logistic equation using the Systat estimated coefficients on the glint image data for this transect, new best fit coefficients were estimated using Excel.

Final Coefficients for Transect 2	
a	-0.695
r	10.5
c	0.9725
Final fit equation	$N_t = \frac{0.28}{1 + e^{-0.695 + (10.5 * 0.9725 \text{distance})}}$

Table 4.4: Final coefficients determined by examining the fit line and glint reflectance data in Microsoft Excel for the second transect.

This second transect was considerably more difficult to fit than the first transect given its sharper increase and flattening. The Systat estimated coefficients did not fit very well, resulting in more estimation by eye using Excel to be necessary. It is important to note that the fit lines tested were quite dependent on the K value used (0.28 in the final fit equation in Table 4.4). This value was changed between transects based on the highest reflectance value present in the transect data. This value should be approximated based on the area being corrected with the model and would vary based on the level of glint present.

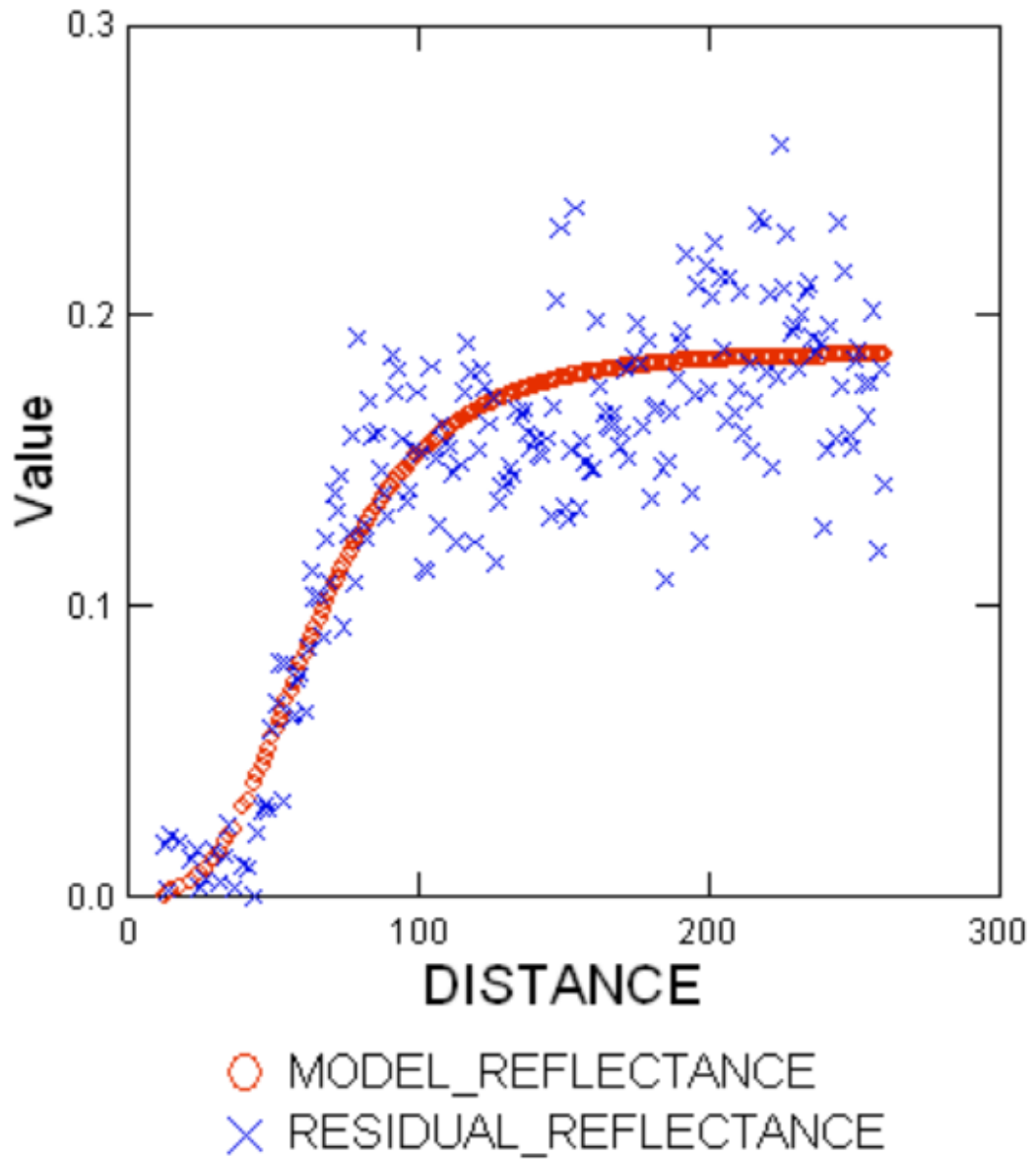


Figure 4.5: Second transect residual reflectance compared to model predicted residual reflectance values.

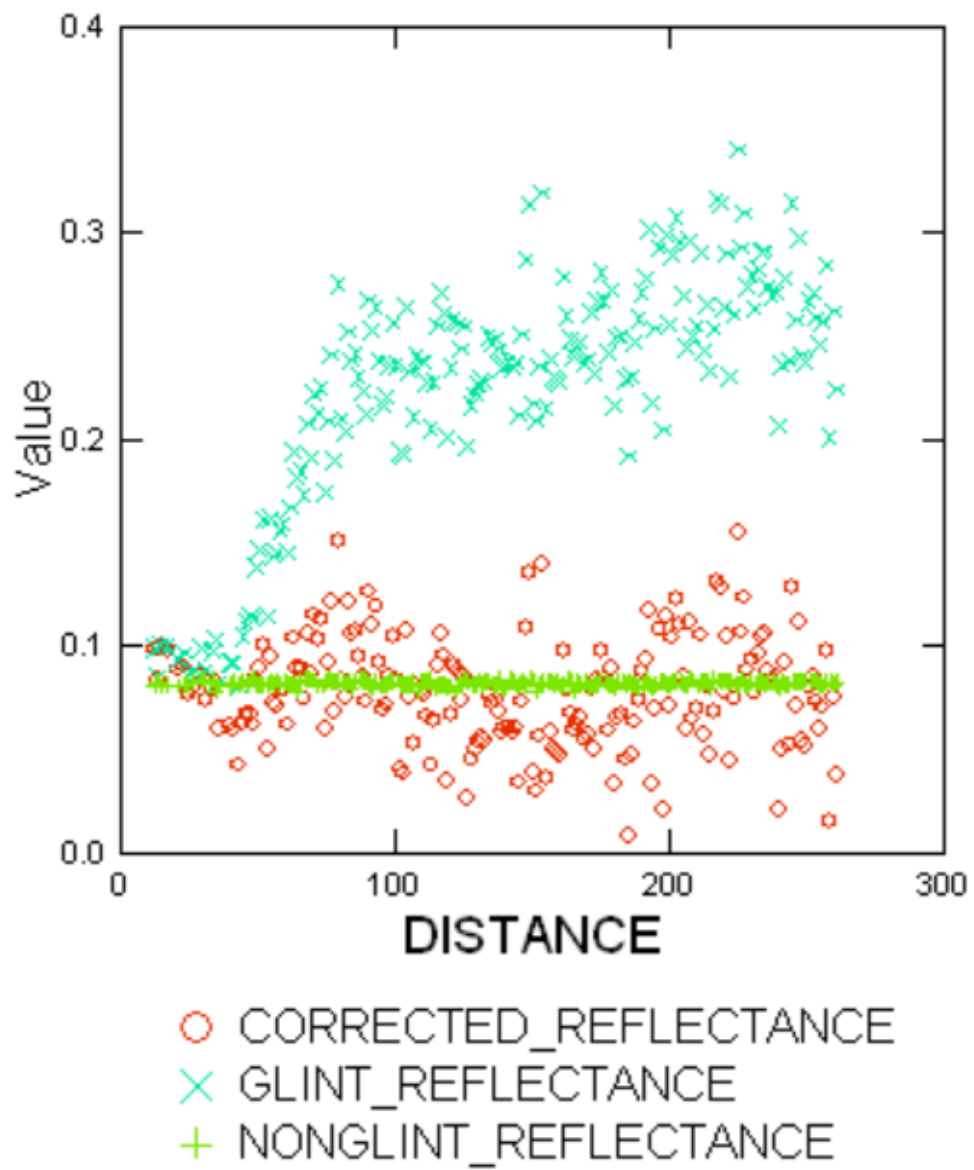


Figure 4.6: Second transect glint and non-glint reflectance compared to the model corrected reflectance values.

The models were then tested on other transects to determine their accuracy and ability to correct. It was apparent upon a visual inspection of various transects across the image that most of them showed a sharp increase and flattening pattern, closer to the shape of the second model produced, which therefore produced much better fits consistently. Due to this, the second model presented was used as the final model for all further analysis. A transect with a much larger total length was selected to test the models ability to correct as distance from the shore increases. Figure 4.7 shows the residuals of the images plotted with the model estimated residual values using the second model. It can be seen that in this case, the model does not predict the steepness of the increase well. For this transect, distance from the shore on the right hand side of the image was estimated using a georeferenced version of the image in ArcGIS Pro. Due to this estimation, the distance values are not as accurate as previous transect from the left hand side of the image.

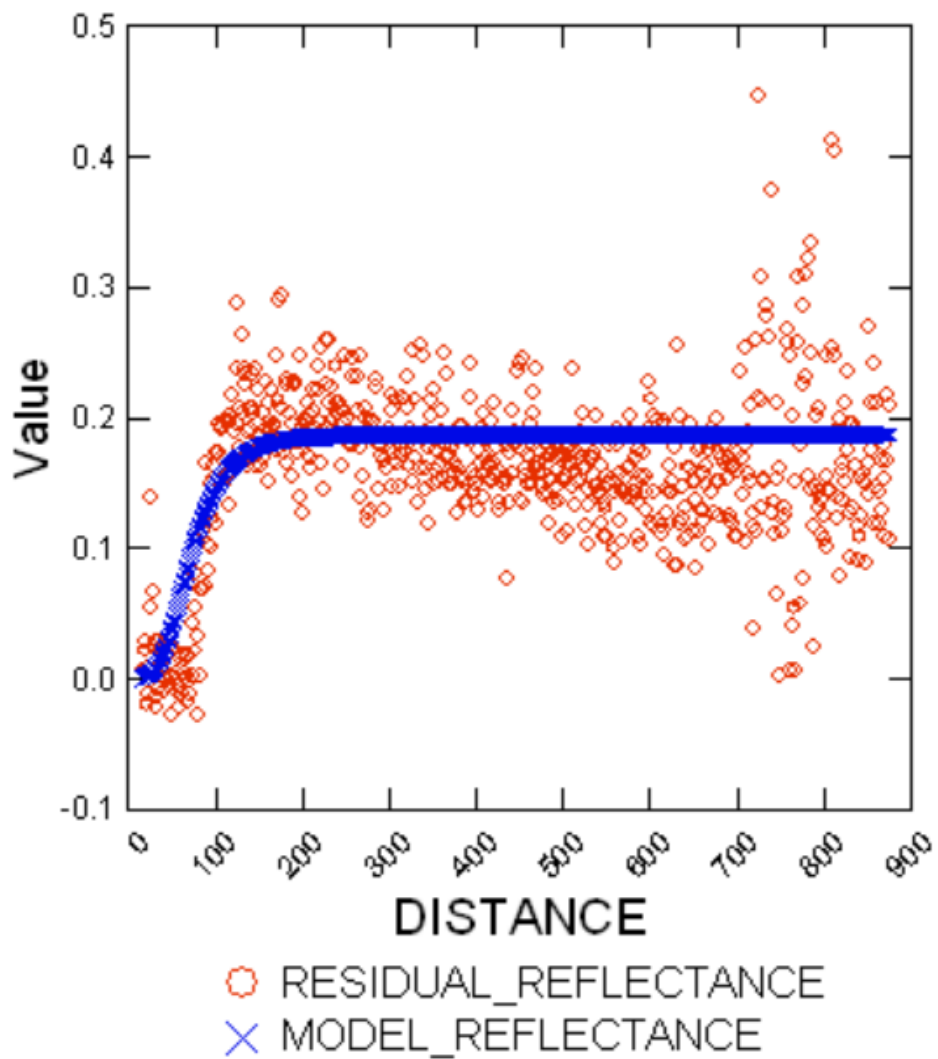


Figure 4.7: Glint image and non-glint image residuals plotted with model predicted residual reflectance values.

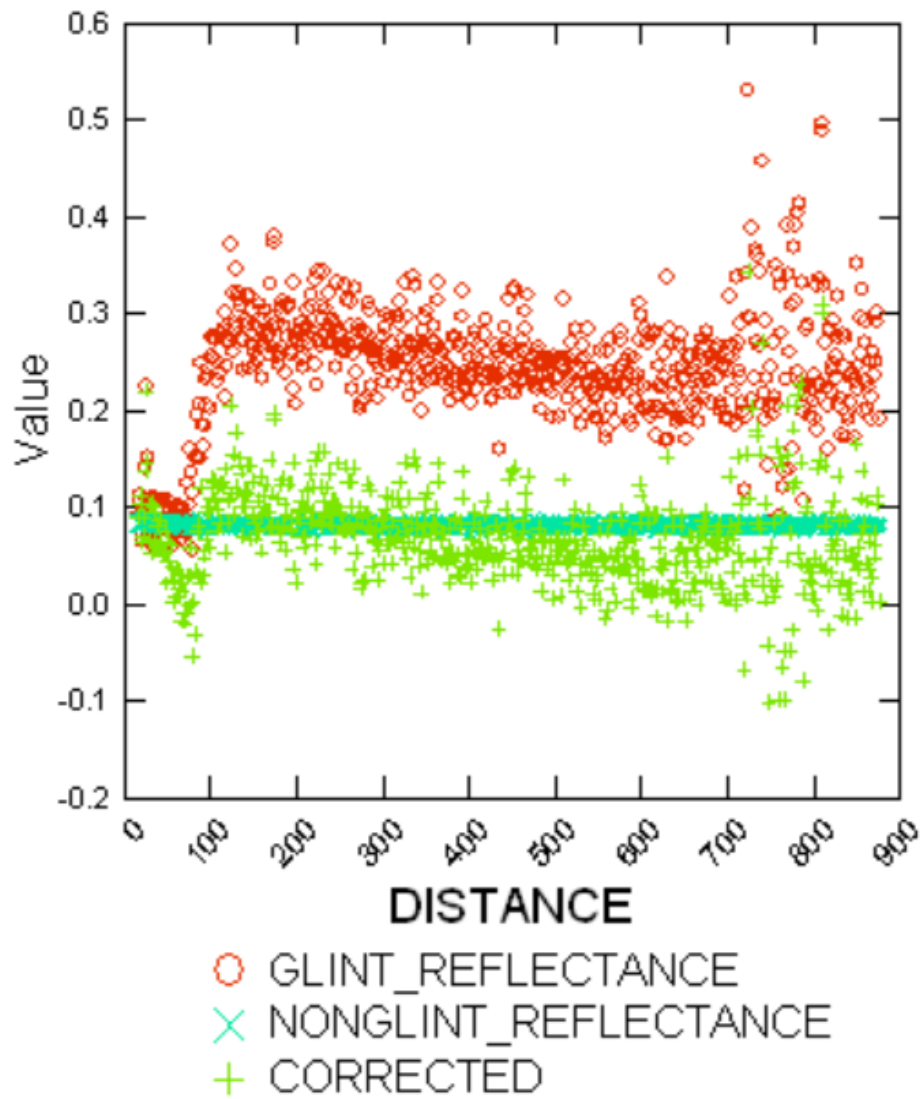


Figure 4.8: Model corrected reflectance values compared to the glint and non-glint reflectance.

It is evident that as distance from the shore increases and the reflectance signal becomes more filled with noise (more variable), the model is less accurate as it is essentially just subtracting a baseline value that comes from the K used. Thus, the noise itself is still present after correction but its scale is greatly reduced, making the signal more accurate than before correction although it retains the same noise patterns. This suggests the model is most accurate at distances closer to the shore. Further transects that do not include larger distances from the shore were used to continue testing the model. Another transect from the left hand side of the image but at a far distance from the transect used to create the model was used for the next test shown in figure 4.9.

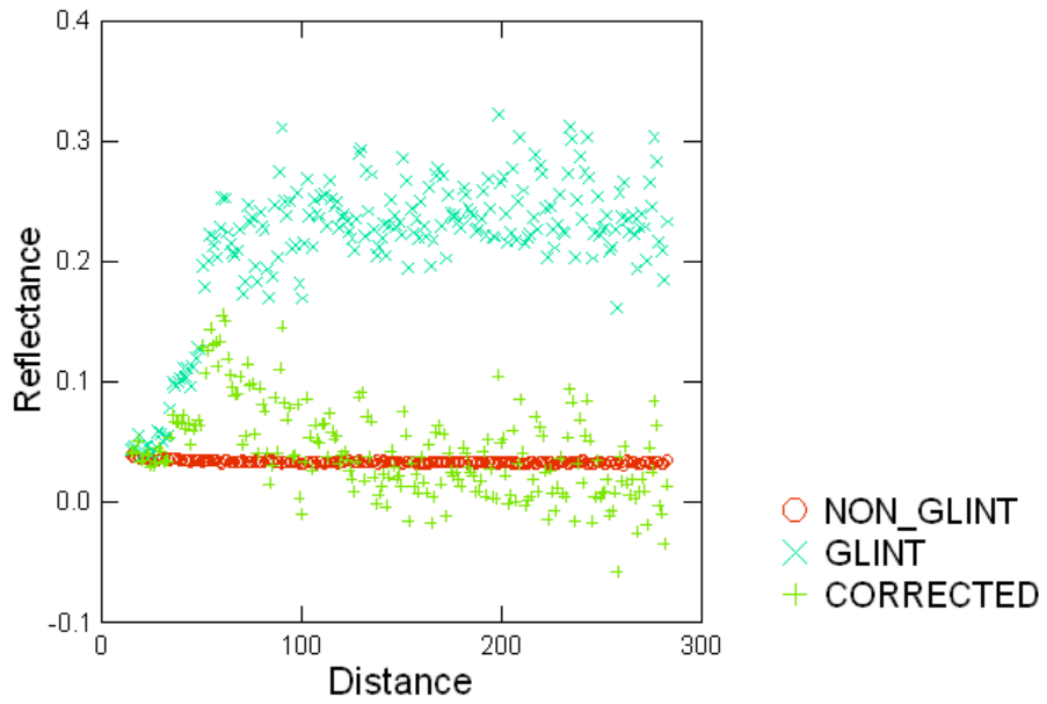


Figure 4.9: Additional transect correction shown compared to glint and non-glint transects.

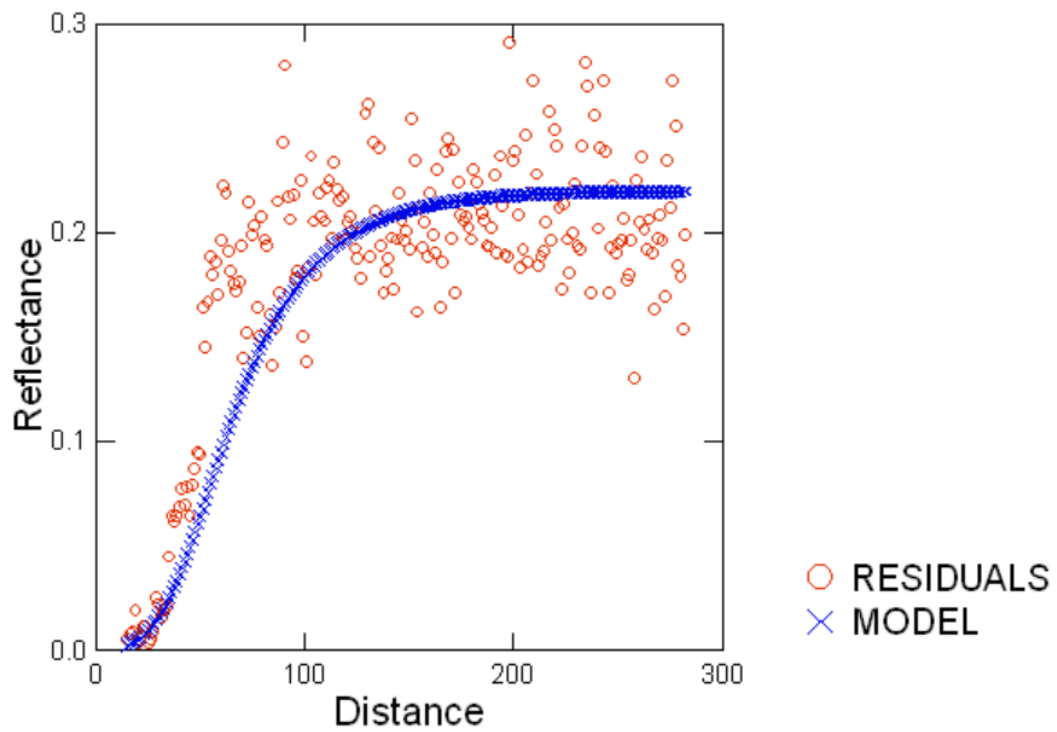


Figure 4.10: Additional transect model predicted residual reflectance values of glint and non-glint image compared to the actual values.

As seen in figure 4.10, although the model does not perfectly fit the steepness of the plot's increase, it still fits the data relatively well for being a randomly selected transect. Based on its ability to better fit other transects in the image, this model based on transect 2 was used as the final model. Given the coefficients determined using Systat and Excel, best estimates for the makeup of these coefficients were established for a, r, and c as shown in Tables 4.5-4.7.

a	
Terms Used	$-\frac{\alpha_1}{\alpha_2}$
Term Units	Dimensionless
Term Values	$-\frac{221.5^\circ}{329.9^\circ}$
Final Value	-0.671
Model Value	-0.695

Table 4.5: For terms used, α_1 refers to the non-glint image sensor azimuth angle and α_2 refers to the glint image sensor azimuth angle (ratio).

r	
Terms Used	$\frac{1}{\vartheta} * \frac{1}{\tau} * \delta^2 * \omega$
Term Units	$\frac{seconds}{meter} * \frac{1}{seconds}$
Term Values	$\frac{1}{3.58} * \frac{1}{7200} * 88^{o2} * 30.1^{\circ}$
Final Value	9.05
Model Value	10.5

Table 4.6: For terms used, ϑ refers to the wind speed in meters per second, τ refers to the time the wind was blowing in the same direction without changing, δ refers to the wind direction angle, and ω refers to the difference between the sensor azimuth angle and the wind direction angle.

c	
Terms Used	$1 - [2 * (\theta_1 + \theta_2 + \theta_3) * (\delta)]$
Term Units	Dimensionless
Term Values	$1 - \left[2 * \left(\frac{12.8}{14.9} + \frac{14.9}{-22.4} + \frac{19.6}{26.6} \right) * \left(\frac{1}{88} \right) \right]$
Final Value	0.97885
Model Value	0.9725

Table 4.7: For terms used, θ_1 refers to the in track viewing angle ratio between the glint and non-glint images. θ_2 refers to the across track viewing angle ratio between the glint and non-glint images. θ_3 refers to the off nadir viewing angle ratio between the glint and non-glint images. δ refers to the inverse of the wind direction, estimated (Eastern wind ~ 90 degrees).

For the value of a, there is only a slight variation between the final value estimated and the model coefficient, within the range of possible values that does not significantly affect the quality of the fit of the model to the data. For the value of r, many of the terms used for the estimate are approximations which can explain the difference between the estimate and the model coefficient. The time the wind was blowing in a constant direction, wind direction angle, and the wind speed are all rough estimates based on historical weather data taken hourly, so some inaccuracies are expected. This can explain the variability of this value. The r term

in the exponential growth model affects the steepness/slope of the curve, which would suggest it is tied to how quickly the amount of glint increases. The terms tied to wind make the most logical sense for this coefficient, because the strength of the wind will cause the increase in glint levels to be more rapid if it is greater. The a term in the model affects the y intercept of the curve, shifting all of the values up or down accordingly, which essentially increases or decreases the total amount of glint present. Because the sensor azimuth angle has a great influence on the amount of glint present, it makes sense that it could play into this coefficient, however this is just an estimate, so it could fit in to a different part of the equation as well.

For the value of c , the slight difference in the model value and the final value estimated using viewing and wind angles could be accounted for due to the uncertainty of the exact wind direction angle. 88 degrees was used in the final value estimation, but the actual value could have varied slightly. The historical data used for this was around 8 minutes prior to the time the first image was collected and did not give precise values for wind directions, only vector arrows. The possible terms that could make up the a , r , and c coefficients given in Tables 4.6-4.8 are only best estimations based on what terms are known to cause glint as well as terms that showed significant differences from the glint to non-glint images. The actual makeup of these coefficients could vary from the estimations given, but they are a good basis to work from for further research and estimation of glint inducing

parameters. The c term in the exponential growth model also contributes to the steepness/slope of the curve as well as the flatness of the beginning and ends of the curve. This coefficient was more difficult to estimate, so values that changed significantly between the glint and non-glint images that are known to contribute to glint were included. Ratios between the various viewing angles as well as the wind direction were used here, all of which could make sense for changing the parts of the curve that the r term influences.

After initial model testing on the transects shown above and final estimations of coefficients values were solidified, more in depth model testing was performed using a region of interest (ROI) from the image. Figure 4.11 shows the region selected for this analysis.



Figure 4.11: The area of the image used for the region of interest (ROI) subset in the glint image. The region within the red box is shown zoomed in. The ROI is made up of all pixels within the green box.

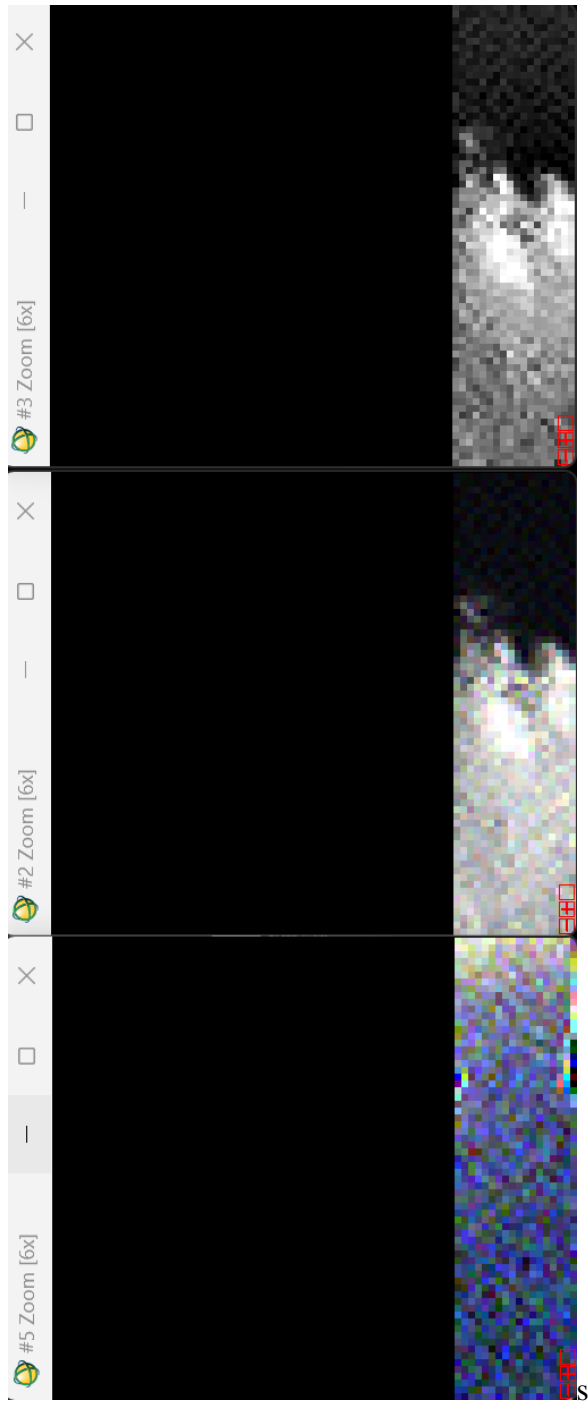


Figure 4.12: A side by side comparison of the ROI used for the non-glnt image (left), the glint image (middle), and the model corrected image (right).

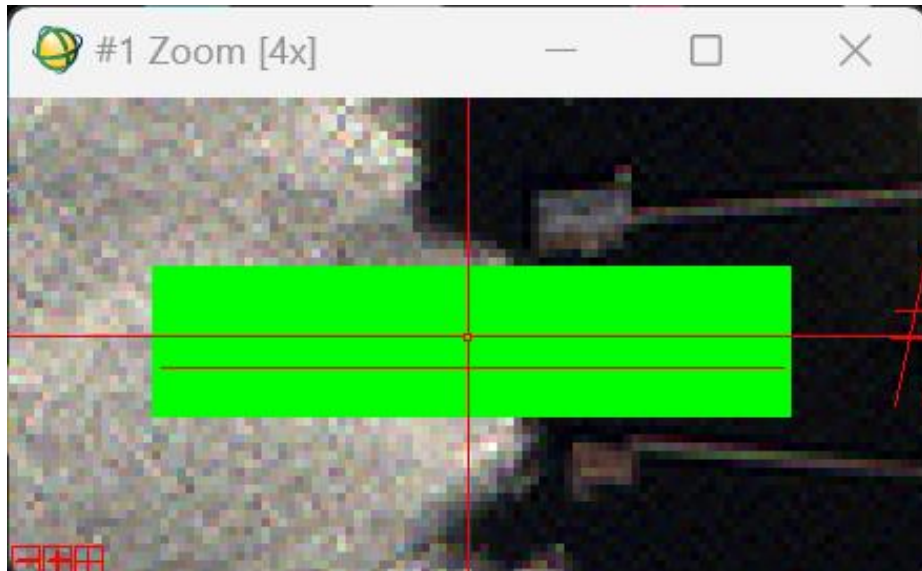


Figure 4.13: Location of the transect across ROI used (red line visible below the crosshairs).

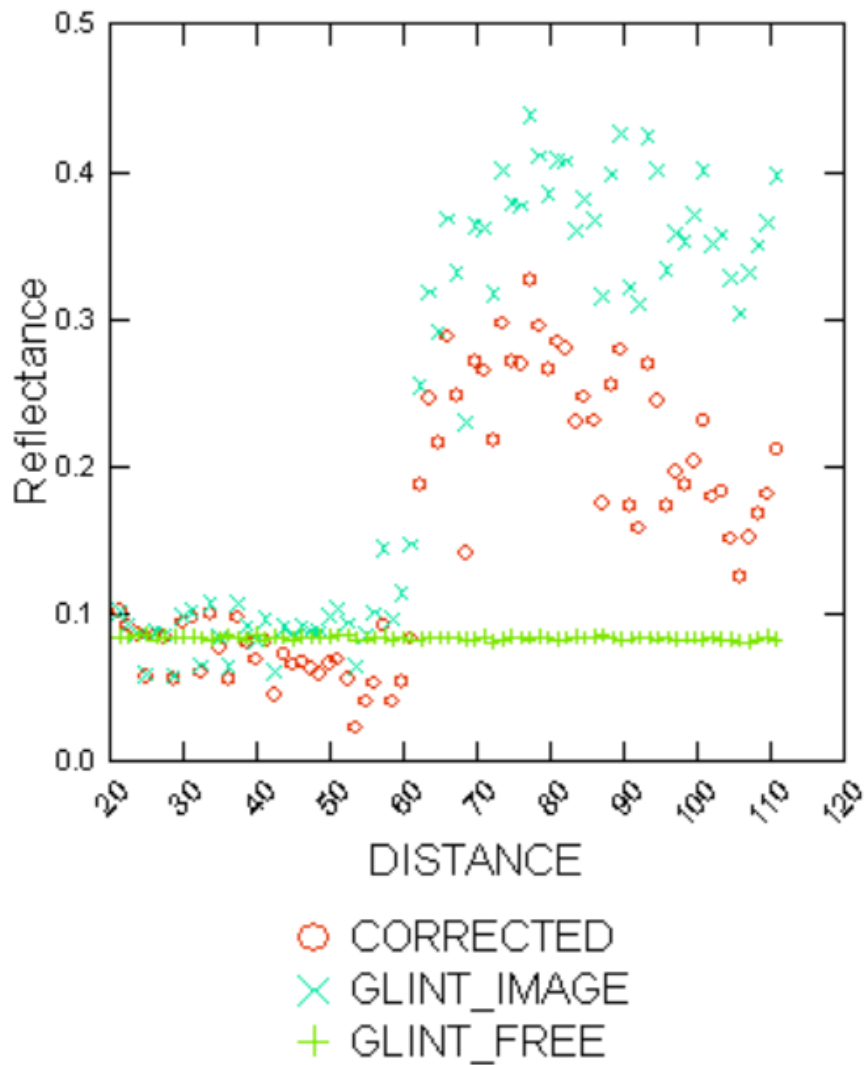


Figure 4.14: ROI visual correction transect reflectances compared to glint and non-glint image transect.

Transect	Mean	Standard Error	Std Deviation	Percent Corrected
Glint	0.238	0.016	0.139	-
Non-glint	0.083	0	0.001	-
Model Corrected	0.154	0.01	0.087	54.19%

Table 4.8: Values taken from the blue band of the glint and non-glint images. Based on the arithmetic means, the amount that was corrected on average from the glint transect using the model was 0.084. Subtracting the Non-glint mean from the glint mean yields that 0.155 should have been corrected out. Thus, a 54.19% correction value was calculated (what was removed- glint minus corrected, divided by what should have been removed- glint minus non-glint).

As can be seen in figure 4.12, although not complete, a definite change can be seen visually from the glint ROI to the corrected ROI. When the pixels are examined statistically, it can be seen that around half of the glint contamination is being successfully removed from the ROI. Figure 4.14 shows that the model struggles to fully correct pixels that are located around 60-70 meters from the shore, where the sharp increase occurs in the plot. After this distance, the amount of glint corrected increases steadily as the distance from the shore increases. This pattern can be expected to continue up to a limit, where the glint removed will appear as it does in figures 4.7-4.8. As an additional check of the accuracy of the model on this region, a random sample of 25 pixels was selected from the corrected

ROI to assess the percent corrected for each pixel. A final average percentage corrected for this sample is also provided, where 3 outliers were removed. These pixels were removed due to the over correction performed on them which skewed the average percent corrected with false negative values.

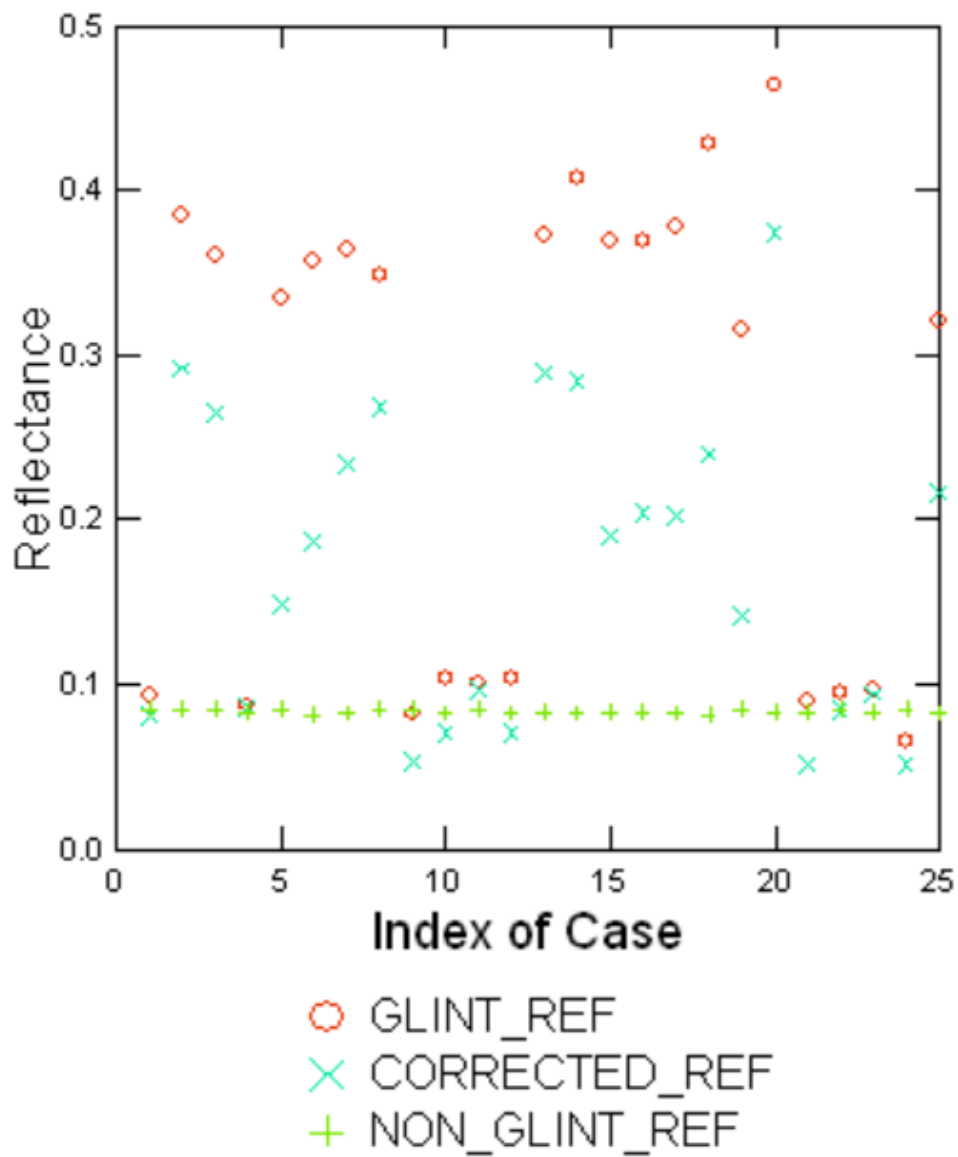


Figure 4.15: Random sample of 25 pixels from the ROI selected, showing corrected reflectance value with the glint and non-glint pixels corresponding.

Pixel	Glint	Corrected	Non-glnt	% Corrected
1	0.093	0.081	0.084	133.3333333
2	0.385	0.292	0.084	30.89700997
3	0.361	0.265	0.084	34.65703971
4	0.087	0.086	0.083	25
5	0.334	0.149	0.084	74
6	0.357	0.187	0.081	61.5942029
7	0.364	0.234	0.082	46.09929078
8	0.349	0.269	0.084	30.18867925
9	0.082	0.053	0.084	-1450
10	0.103	0.071	0.082	152.3809524
11	0.101	0.097	0.084	23.52941176
12	0.103	0.071	0.082	152.3809524
13	0.373	0.289	0.083	28.96551724
14	0.407	0.284	0.082	37.84615385
15	0.369	0.191	0.083	62.23776224
16	0.369	0.204	0.083	57.69230769
17	0.378	0.203	0.082	59.12162162
18	0.428	0.24	0.081	54.17867435
19	0.315	0.142	0.085	75.2173913
20	0.464	0.375	0.083	23.35958005
21	0.09	0.052	0.083	542.8571429
22	0.095	0.084	0.084	100
23	0.097	0.094	0.083	21.42857143
24	0.065	0.051	0.084	-73.68421053
25	0.321	0.216	0.082	43.93305439

Table 4.9: Random pixel reflectance values for glint, non-glnt, and the corrected ROIs. Values that are above 100 or negative reflect areas where the model over corrected glint pixels. An average correction percentage of 60.37% when outlier pixels 9, 21, and 24 were removed was calculated.

Transect	Mean	Standard Error	Std Deviation	Percent Corrected
Glint	0.26	0.029	0.143	-
Non-glint	0.083	0	0.001	-
Model Corrected	0.171	0.019	0.094	49.7%

Table 4.10: Statistics calculated for the random sample of 25 pixels from the ROI used. Percent corrected based solely on mean values values, not averaged with every pixel as in Table 4.9.

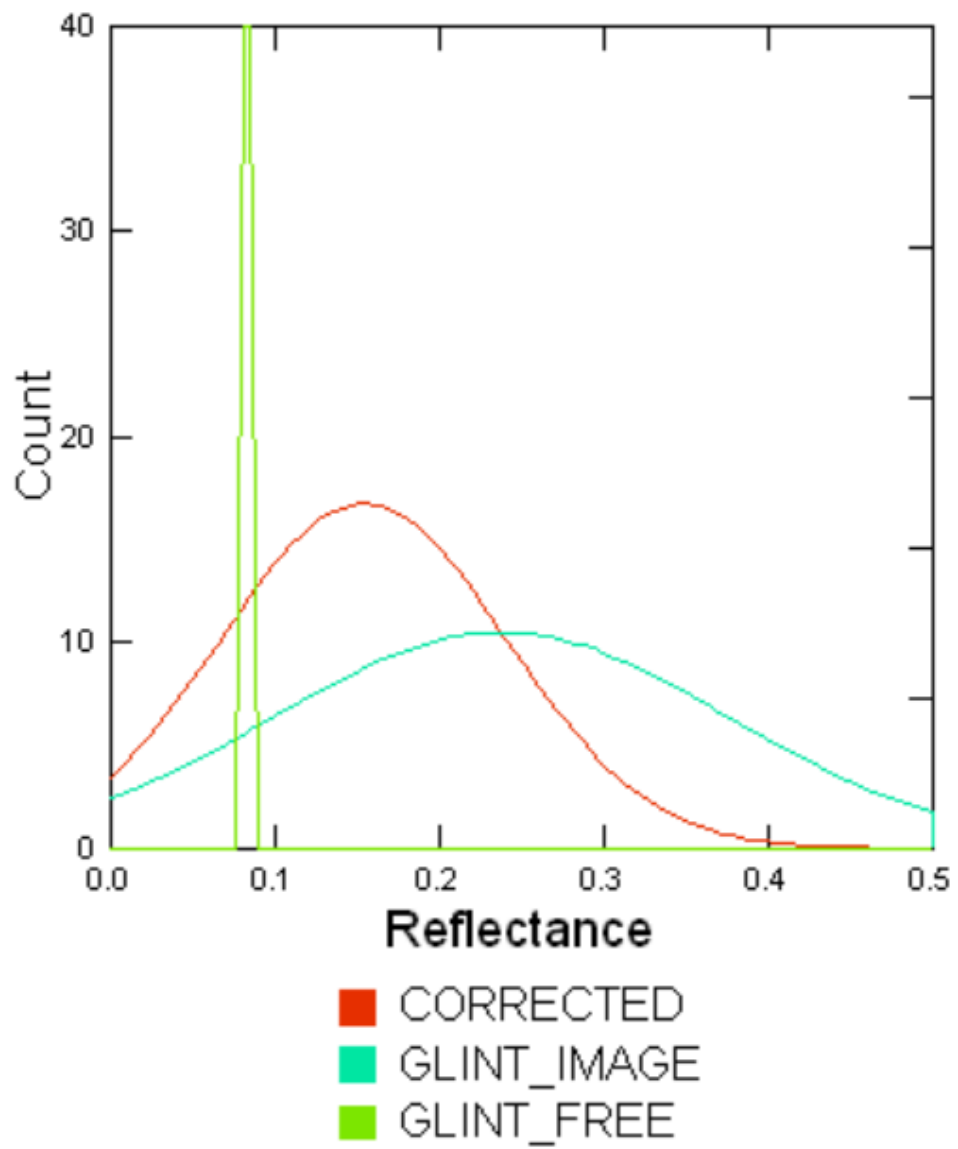


Figure 4.16: Distributions of reflectance values in the transect through the ROI for both images and the corrected image.

As evident from figure 4.11, although the model does not perfectly correct all of the glint present, it does remove a considerable amount of it and transforms the distribution of reflectance values closer to what it should be. When examining on a pixel by pixel basis for this random selection of pixels, it is seen that the model continues to correct around 50 to 60 percent of the glint present.

4.2 Hedley Comparison Results

The results of the Hedley correction on the glint contaminated image are shown in figures 4.1-4.8. It is evident that the correction method did not actually correct most of the glint known to be present in the image.



Figure 4.17: Multispectral region of interest ENVI windows displayed using original reflectance values (left) and Hedley corrected reflectance values (right). A visible difference is not very pronounced.

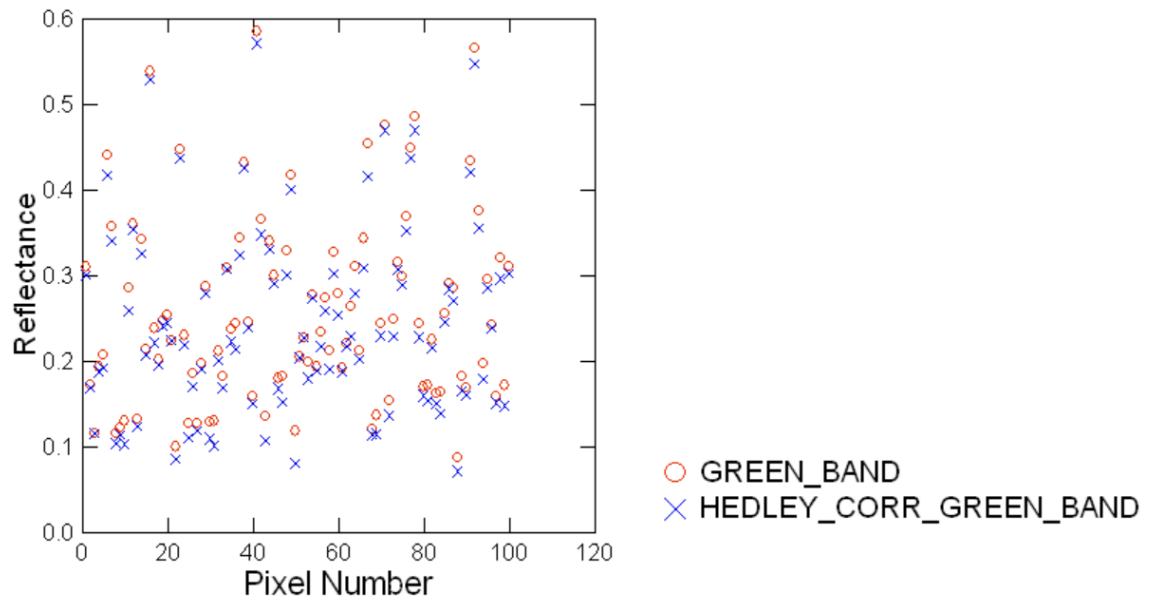


Figure 4.18: A section of the region of interest reflectance values of the original green band (glint contaminated image) and corresponding reflectance values for the Hedley corrected pixels, no scaling factor introduced.

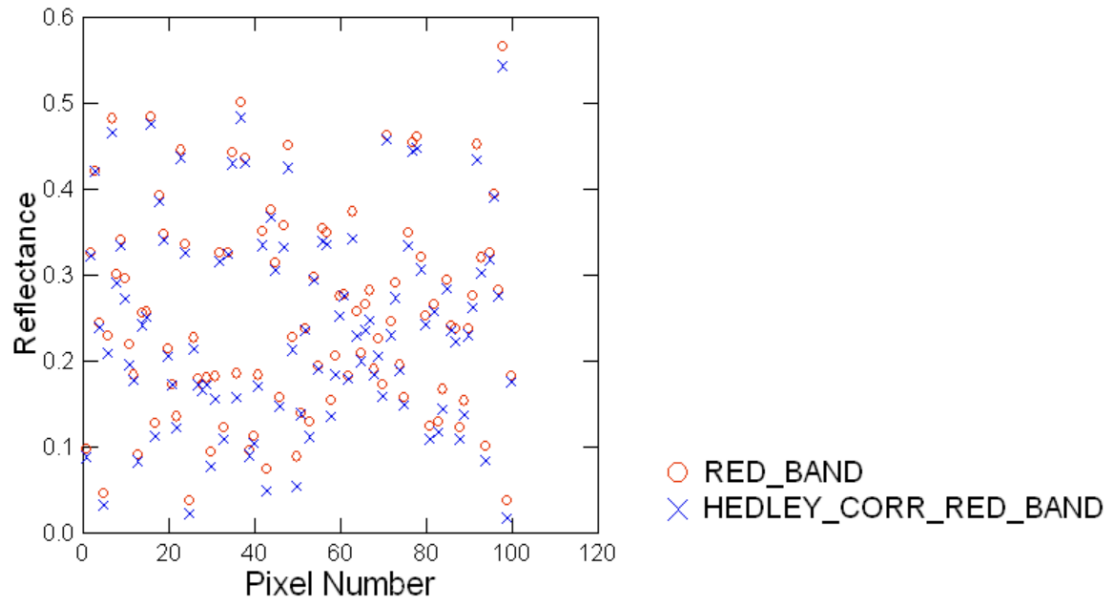


Figure 4.19: A section of the region of interest reflectance values of the original red band (glint contaminated image) and corresponding reflectance values for the Hedley corrected pixels, no scaling factor introduced.

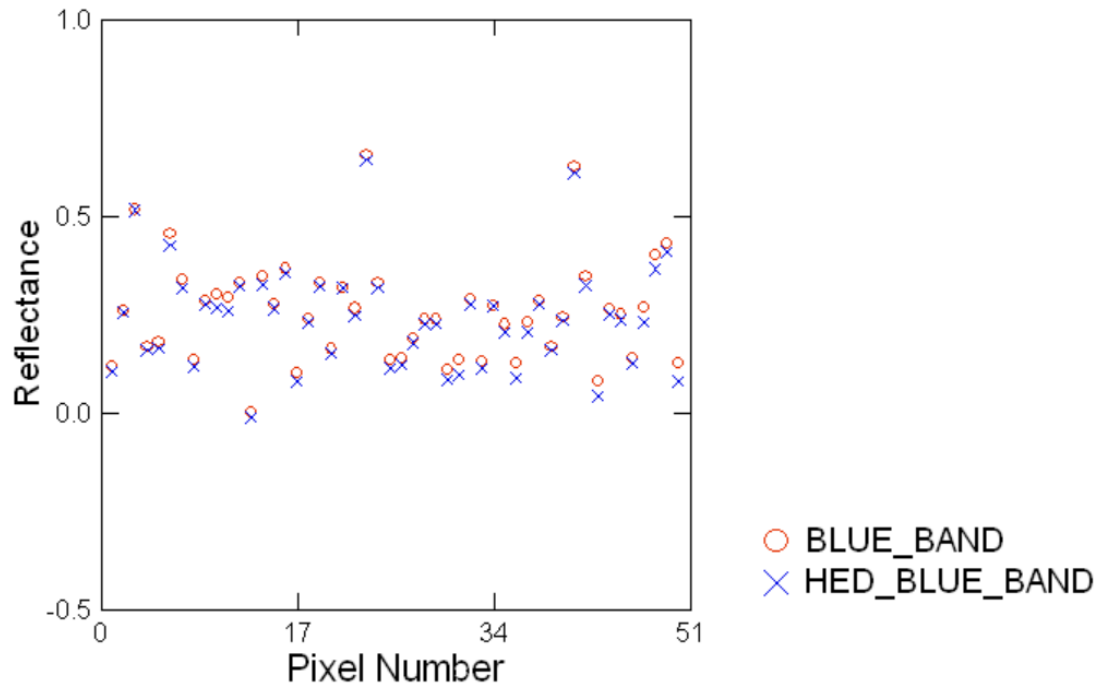


Figure 4.20: A section of the region of interest reflectance values of the original blue band (glint contaminated image) and corresponding reflectance values for the Hedley corrected pixels, no scaling factor introduced.

Due to the inadequacy of this correction, a scale factor was introduced to uniformly increase the value that is subtracted from the original reflectance value to correct it. Figures 4.5-4.7 show each band with a 100% increase in this value.

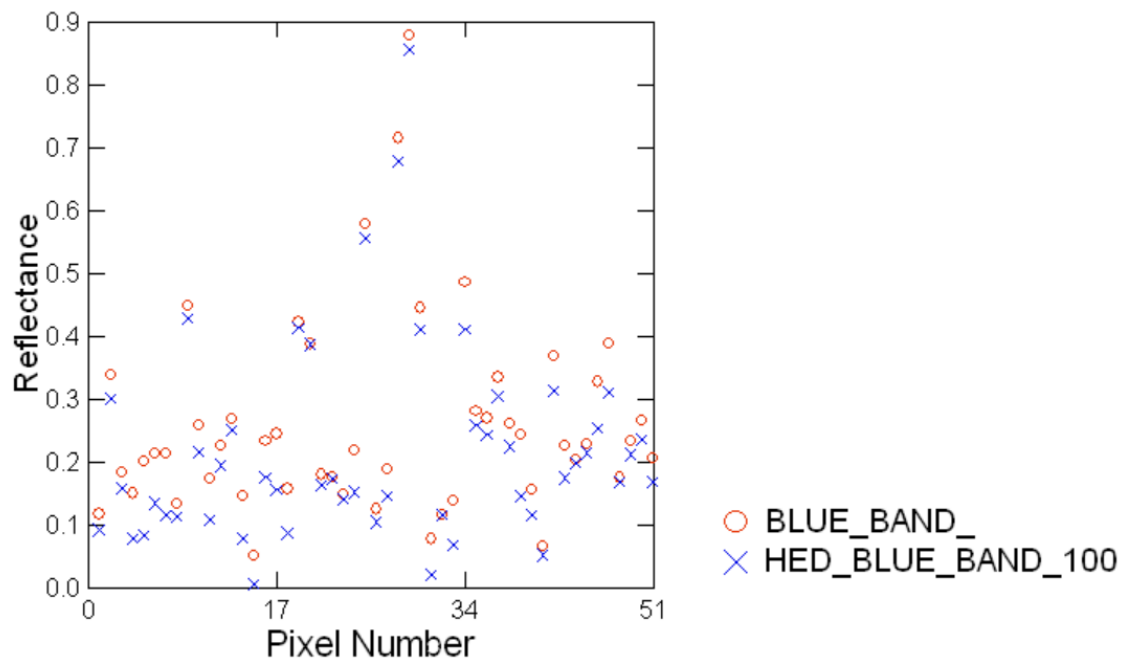


Figure 4.21: A section of the region of interest reflectance values of the original blue band (glint contaminated image) and corresponding reflectance values for the Hedley corrected pixels, a 100% increase scaling factor introduced.

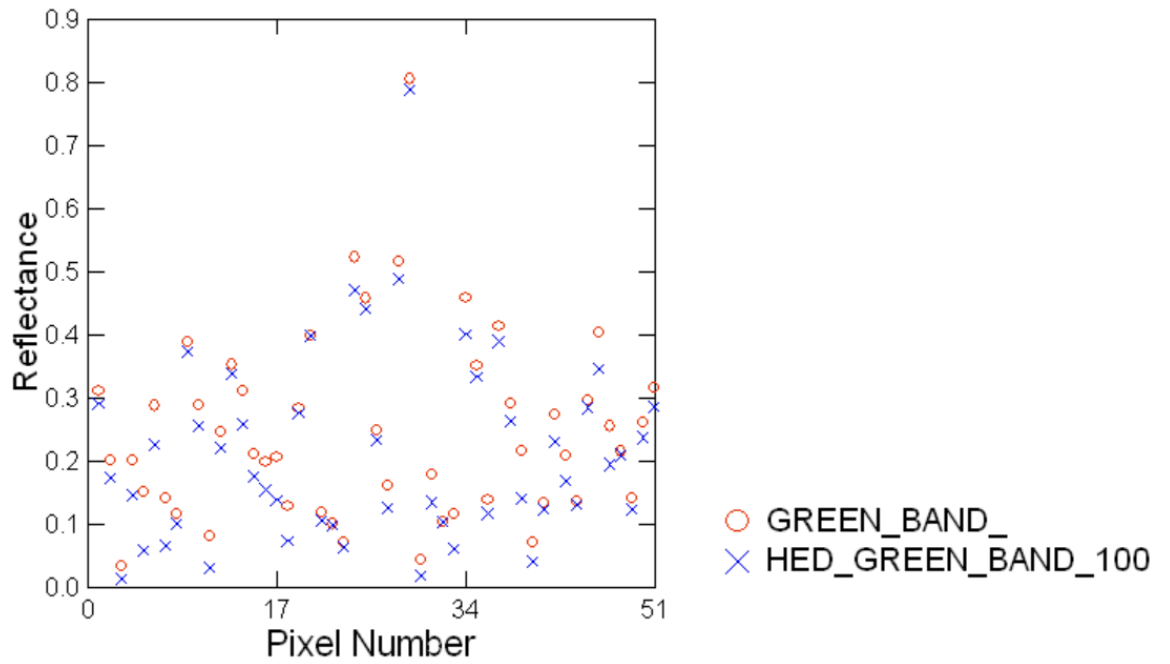


Figure 4.22: A section of the region of interest reflectance values of the original green band (glint contaminated image) and corresponding reflectance values for the Hedley corrected pixels, a 100% increase scaling factor introduced.

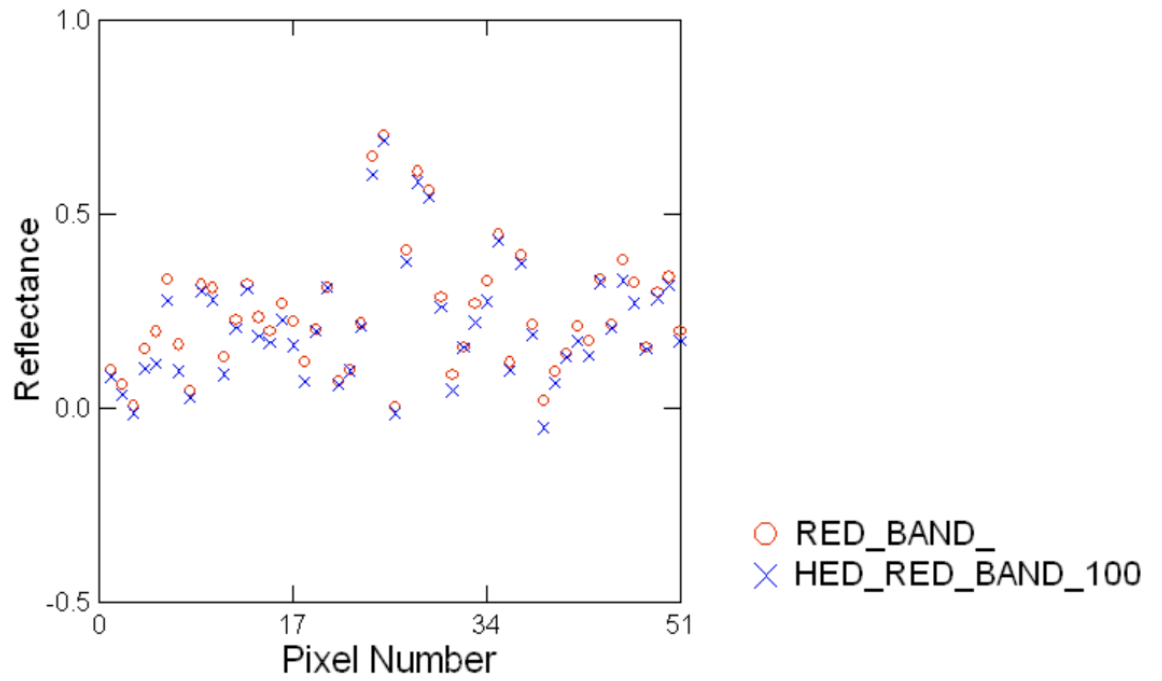


Figure 4.23: A section of the region of interest reflectance values of the original red band (glint contaminated image) and corresponding reflectance values for the Hedley corrected pixels, a 100% increase scaling factor introduced.

Due to the inadequacy of this 100% scale up, the ideal calculated 6000% scale factor was introduced as seen in figure 4.8. Although this scale factor was calculated using a sample pixel and all of the corresponding values for that pixel from both images, the Hedley correction using this scale factor still did not produce adequate results. The uncorrected glint free image pixel values are all very homogenous, around 0.03, so even if a scale factor is made to create the perfect correction for one pixel, the other pixels will still not be corrected adequately due to the nature of the equation and the inevitable variability of the values it produces.

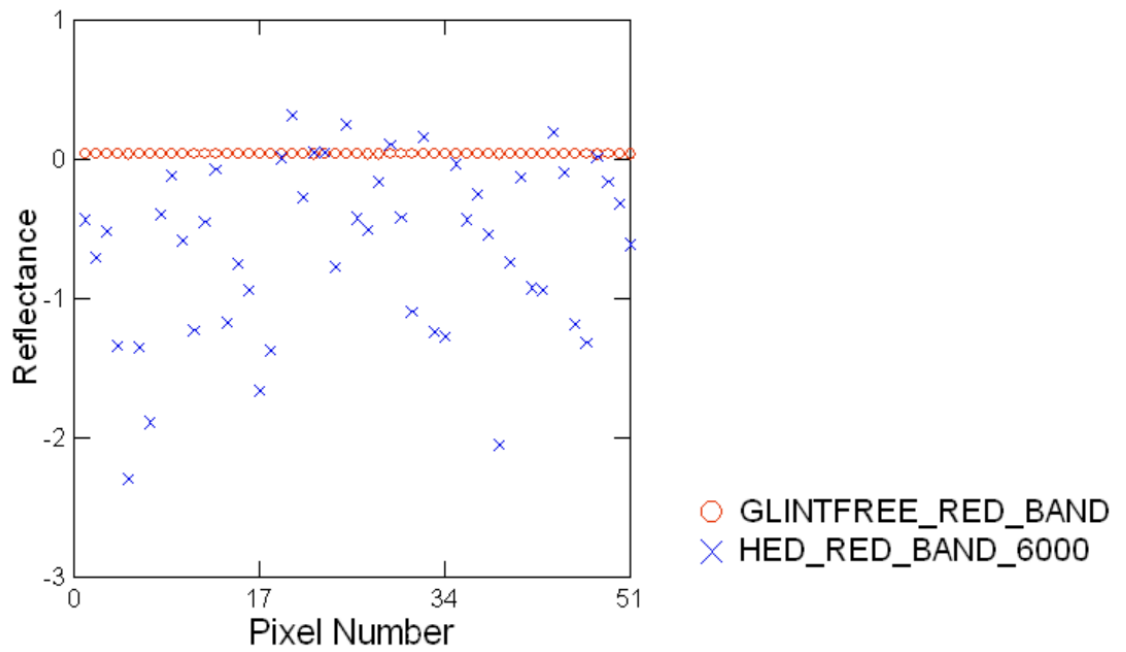


Figure 4.24: A section of the region of interest reflectance values of the glint free image (which would be the ideal corrected values) and corresponding reflectance values for the Hedley corrected pixels, a 6000% increase scaling factor introduced.

Based on these correction results, it is evident that a NIR method such as Hedley's proves inadequate to properly correct this image due to the intensity and variability of the glint present. Even when the correction is scaled up to the appropriate range of values, the "corrected" pixels still have a strong presence of noise relative to the non-glint pixels. This is due to the very high amount of glint present in the image, causing a large amount of variability within the image. When one average pixel is selected to scale the rest of the correction to, the noisy pixels around it will also be scaled into much larger values that no longer make logical sense as reflectance values. This is seen in figure 4.24, where some of the noisiest pixels are amplified to values such as -2. This shows that with an image that has very high levels of glint, an accurate correction with this method would not be possible.

5. Summary and Recommendations

5.1 Summary of Work Done

For this thesis, a model of sun glint was produced using the residuals between two nearly simultaneously collected WorldView-3 images. Transects corresponding to fetch distance changes were produced and used to create estimated glint equations. Although a perfect model could not be attained, a good working estimate for the best fitting glint inducing parameters to the final coefficients was made to produce the final model. These parameters accounted for viewing angle geometry and wind properties, which are the terms known to induce glint. The resulting model was also compared to a commonly used NIR glint correction method, which proved ineffective for accurately removing the glint in these images. Relative to the model created in this work, the Hedley method proves less effective. Although noise is still present in the final model corrections, the model is still able to correct better than some existing methods for images with a large amount of glint.

5.2 Recommendations

If this work were to be continued and built upon, it would be highly beneficial to purchase more imagery with a larger area, namely expanding to the East shore of the Banana River side of the image. This would greatly improve the

fetch distance distribution of glint and allow for better transects containing more useful information to be created. If more imagery could be identified that shared the same characteristics of the glint contaminated and glint free images used in this work, these would be very useful for building this model, allowing for different wind speeds, wind directions, and sensor and sun geometry angles to test on the model and fine tune it further. Additionally, although many glint inducing factors were considered when estimating the makeup of the fit line coefficients, there may be other factors contributing to the existence of sun glint that were not considered in the scope of this study, such as the bathymetric composition of the seafloor amongst others. If additional time was available, this study could be performed on more transects within the same images and tested across various areas in the images. Due to the scope and timeline of this thesis, further analysis was unable to be conducted and is recommended for future continuations of this work.

References

- Bostater, C., Gimond M., & Campbell M. (2000). Comparing a hyperspectral Monte-Carlo approach for simulating water surface reflectance signatures based upon radiative transfer theory: simulating clear water and Caribbean Sea bottom types. *SPIE, Vol 4172*.
- Bostater, C., Ma, W., & McNally, T. (1997). Advancement of an optical remote sensing model to simulate the underwater light field. *SPIE, Vol 2959*, 180-188.
- Hedley, J. D., Harborne, A. R., & Mumby P. J. (2005). Simple and robust removal of sun glint for mapping shallow-water benthos. *International Journal of Remote Sensing, Vol 26*(issue 10), 2107-2112.
- Tsoularis, A., Wallace, J. (2002). Analysis of Logistic Growth Models. *Mathematical Biosciences, Vol 179*(1), 21-55.
- Kay, S., Hedley, J. D., Lavender, S. (2009). Sun Glint Correction of High and Low Spatial Resolution Images of Aquatic Scenes: a Review of Methods for Visible and Near-Infrared Wavelengths. *Remote Sensing, Vol 1*(4), 697-730.
- Cox, C. & Munk, W. (1954). Measurement of the Roughness of the Sea Surface from Photographs of the Sun's Glitter. *Journal of the Optical Society of America, Vol 44*(11), 838-850.
- Bostater, C., & Huddleston, L. (2000). Layered analytical radiative transfer model for simulating water color of coastal waters and algorithm development. *SPIE, Vol 4172*, 153–161.

- Adjovu G. E., Stephen H., James D., & Ahmad S. (2023). Overview of the Application of Remote Sensing in Effective Monitoring of Water Quality Parameters. *Remote Sensing*, Vol 15(7), 1938.
- Weather Underground. (2014). Melbourne, FL Weather History. <https://www.wunderground.com/history/daily/us/fl/melbourne/KMLB/date/2014-8-28>.
- Land Info Worldwide Mapping LLC. (2018). Satellite Imagery Pricing. https://landinfo.com/wp-content/uploads/2018/04/landinfo.com-LAND_INFO_Satellite_Imagery_Pricing.pdf
- Ebuchi, N., & Kizu, S. (2002). Probability Distribution of Surface Wave Slope Derived Using Sun Glitter Images from Geostationary Meteorological Satellite and Surface Vector Winds from Scatterometers. *Journal of Oceanography*, Vol. 58, 477-486.
- Wu, J. (1990). Mean square slopes of the wind-disturbed water surface, their magnitude, directionality, and composition. *Radio Science*, Vol 25(1), 37-48.
- Kutser, T., Vahtmäe E., & Praks J. (2009). A sun glint correction method for hyperspectral imagery containing areas with non-negligible water leaving NIR signal. *Remote Sensing of Environment*, Vol 113(10), 2267-2274.
- Lyzenga, D., Malinas, N., & Tanis, F. J. (2006). Multispectral bathymetry using a simple physically based algorithm. *Geoscience and Remote Sensing*, Vol 44, 2251- 2259.

- Taggart, A. (2021). A Glint Contaminated Pixel Correction Algorithm and Potential Application for Estimating Water Visibility. *Florida Institute of Technology Thesis*.
- Taggart, A., & Bostater, C. (2021). A WorldView-3 multispectral glint correction methodology and relation to hyperspectral signatures in space coast Florida waters. *SPIE International Society for Optics and Photonics, Vol 11857*, 85-92.
- Aziz, S., & Bostater C. (2019). Remote Sensing of the Ocean, Sea Ice, Coastal Waters, and Large Water Regions. *SPIE International Society for Optics and Photonics, Vol 11150*, 70-80.
- Mijwil, M., Esen A., & Alsaadi, A. (2019) Overview of Neural Networks. *Vol. 1*.
- Cao, B., Yong, F., Jiang, Z., & Gao, L. (2019). Shallow water bathymetry from WorldView-2 stereo imagery using two-media photogrammetry. *European Journal of Remote Sensing, Vol 52(1)*, 506-521.
- Digital Globe. (2017). Data Sheet WorldView-3. https://dgv4-cms-production.s3.amazonaws.com/uploads/document/file/128/DG2017_WorldView-3_DS.pdf
- Nugent, A., DeCou, D., Russell, S., & Karamperidou C. (2022). Chapter 11: General Circulation. *Atmospheric Processes and Phenomena*.
- Fagherazzi, S. & Wiberg P. L. (2009). Importance of wind conditions, fetch, and water levels on wave-generated shear stresses in shallow intertidal basins. *Journal of Geophysical Research: Earth Surface, Vol 114(F3)*.

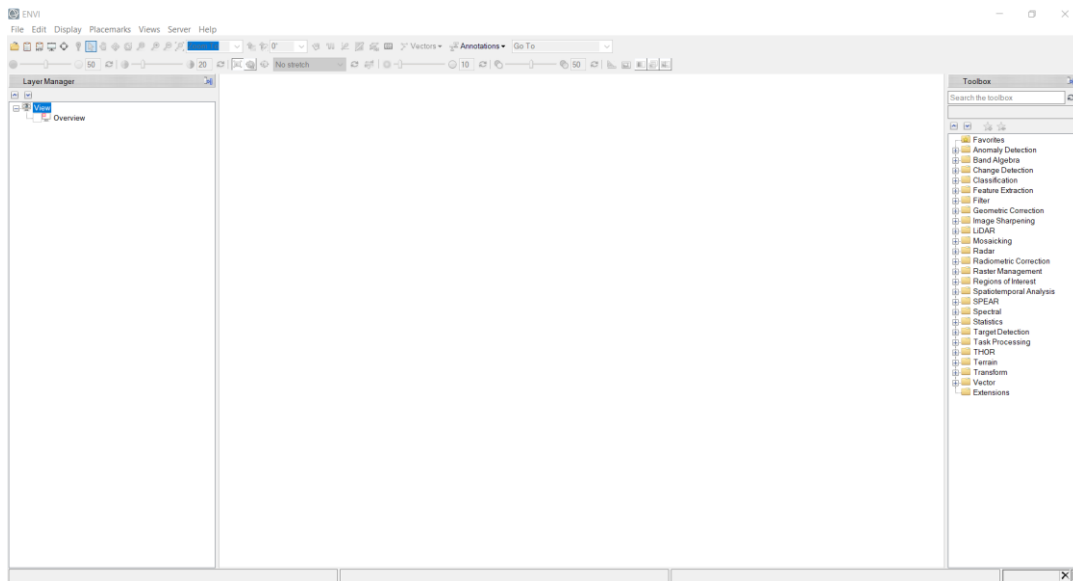
- Steinmetz, F., Deschamps, P. Y., & Ramon, D. (2011). Atmospheric correction in presence of sun glint: application to MERIS. *Optics express*, Vol 19(10), 9783–9800.
- Doerffer, R. Schiller, H. Fischer, J. Preusker, R. & Bouvet, M. The Impact of Sun Glint on the Retrieval of Water Parameters and Possibilities for the Correction of MERIS Scenes. In Proceedings of the 2nd MERIS-(A)ATSR workshop, Frascati, Italy, September 22–26, 2008.
- Singh, R. K. & Shanmugam, P. (2014) A Robust Method for Removal of Glint Effects from Satellite Ocean Colour Imagery. *Ocean Science*, Vol 11, 2791-2829.
- Chavez, Jr, P. (1988). An improved dark-object subtraction technique for atmospheric scattering correction of multispectral data. *Remote Sensing of Environment*, Vol 24, 459-479.
- Budde, W. (1976). Calibration of Reflectance Standards. *Journal of Research of the National Institute of Standards and Technology*, Vol 80A(4), 585-595.

Appendix A

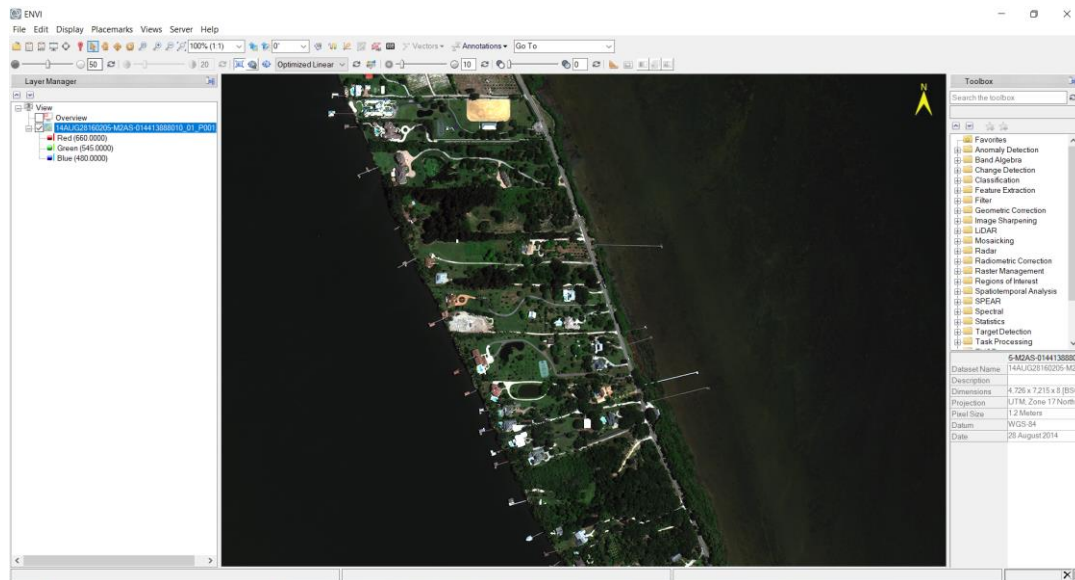
Performing Radiometric Calibration on Raw Imagery in ENVI

In order to begin working with the raw imagery from WorldView-3, a radiometric calibration had to be performed on the data using ENVI 5.6.3. Below are the documented steps taken to transform the raw imagery from counts to radiance and reflectance values.

First ENVI 5.6.3 was started up, which should look as follows.



Select “File”, then “Open”, and navigate to the image folder. Select the file for the image that has a .til extension and open it. That should open up the image to appear as follows.



Next, from the “Toolbox” menu on the right hand side of the window, select “Radiometric Correction” to expand the drop down list.

Toolbox

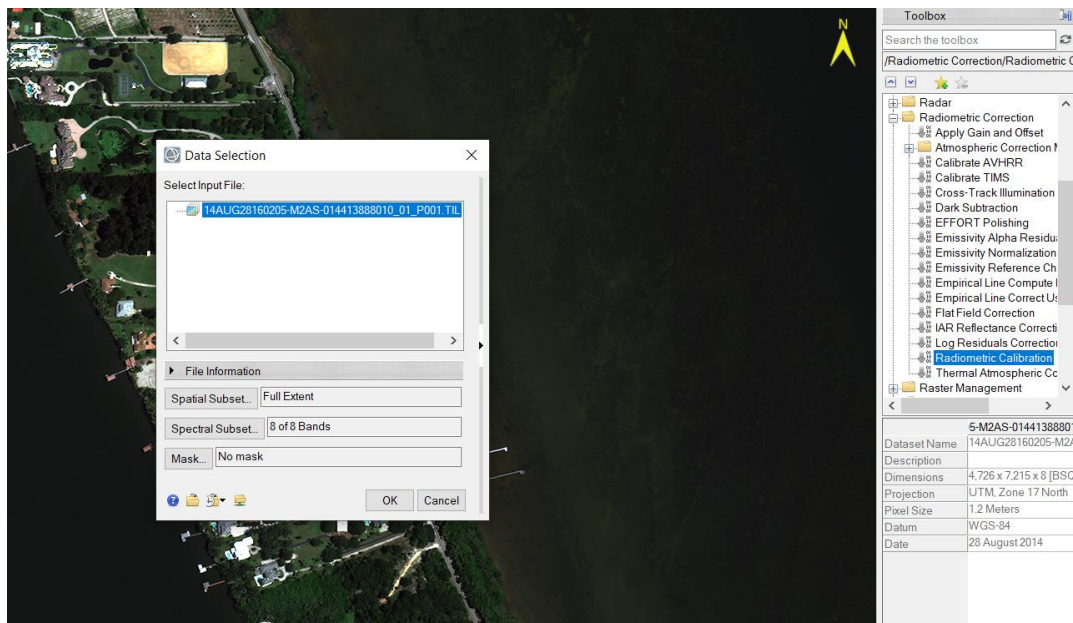
Search the toolbox

/Radiometric Correction

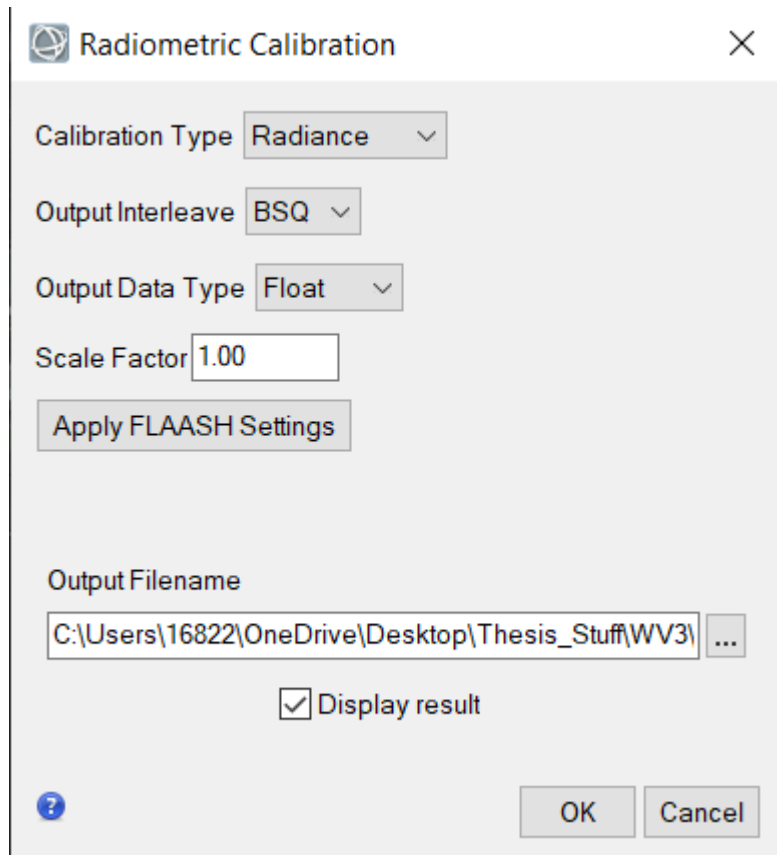
- [-] Mosaicking
- [-] Radar
- [+] Radiometric Correction
 - Apply Gain and Offset
 - [+] Atmospheric Correction
 - Calibrate AVHRR
 - Calibrate TIMS
 - Cross-Track Illumination
 - Dark Subtraction
 - EFFORT Polishing
 - Emissivity Alpha Residu:
 - Emissivity Normalization
 - Emissivity Reference Ch
 - Empirical Line Compute I
 - Empirical Line Correct U
 - Flat Field Correction
 - IAR Reflectance Correcti
 - Log Residuals Correction
 - Radiometric Calibration
 - Thermal Atmospheric Co

	5-M2AS-01441388801
Dataset Name	14AUG28160205-M2A
Description	
Dimensions	4,726 x 7,215 x 8 [BSQ]
Projection	UTM, Zone 17 North
Pixel Size	1.2 Meters
Datum	WGS-84
Date	28 August 2014

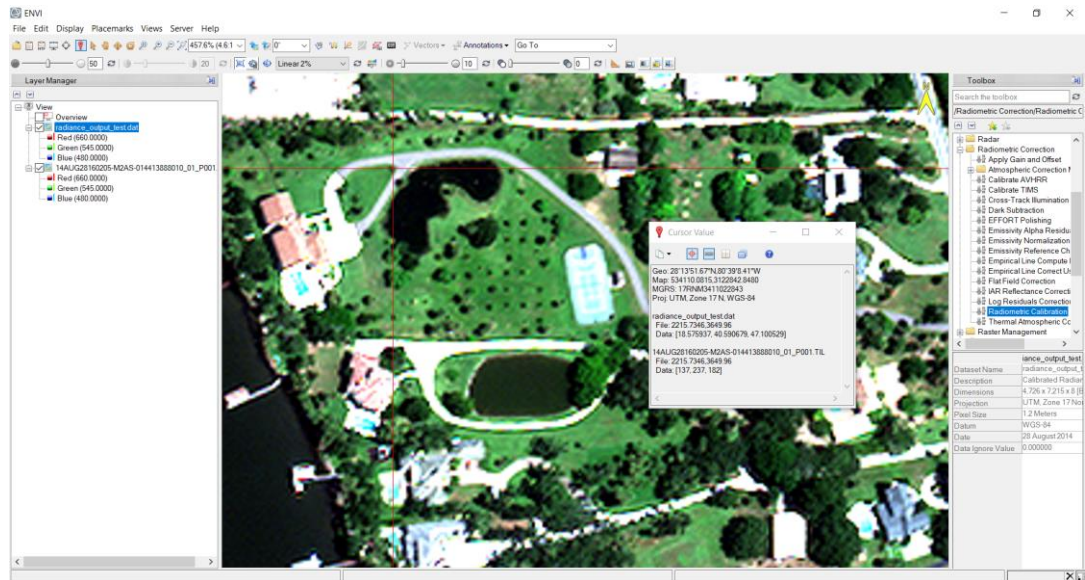
From the dropdown menu under radiometric correction, double click radiometric calibration and data selection window pops up.



Select the .til file and click OK. A new pop up window should appear with preset values filled in as follows.

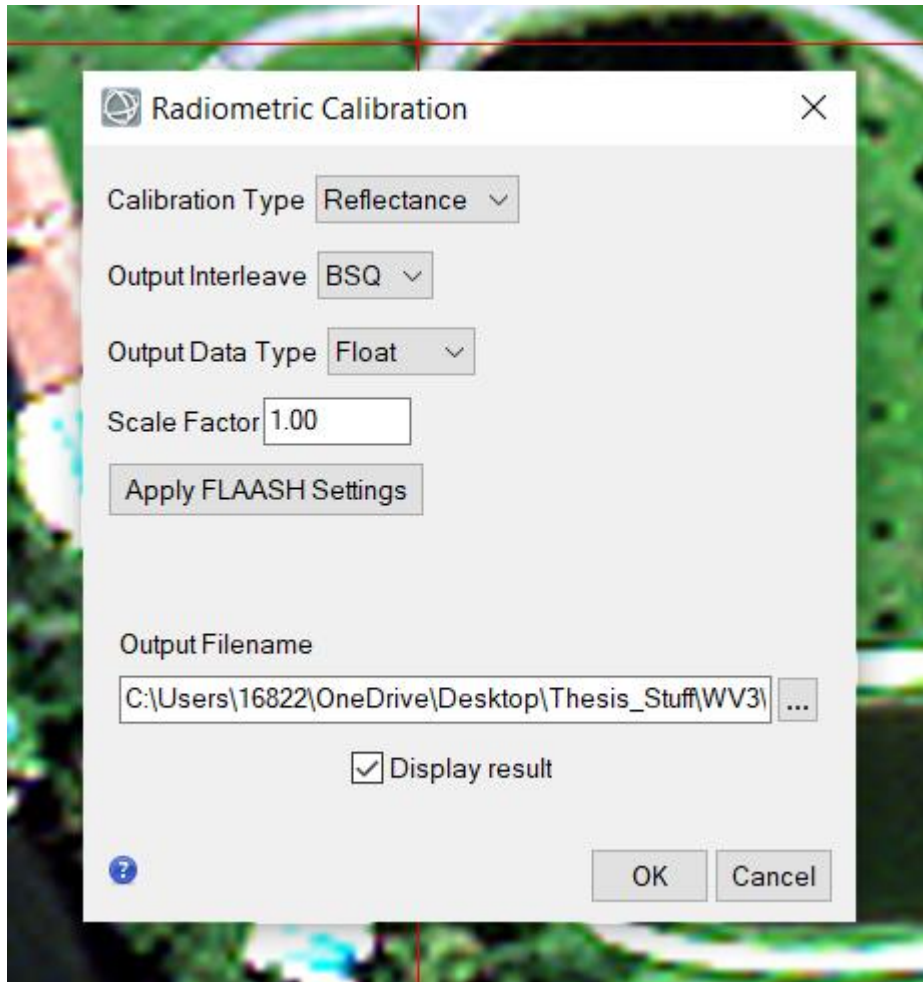


Make sure it is set to “Radiance” for “Calibration Type” and select a location and name for the output, click OK. The new radiance file should now be ready for use and appears on the screen.



An example of what the new radiance values look like in comparison to their original raw counts is shown above using the cursor value tool.

Now to create the reflectance value image, double click Radiometric Calibration once again and select the .til file.

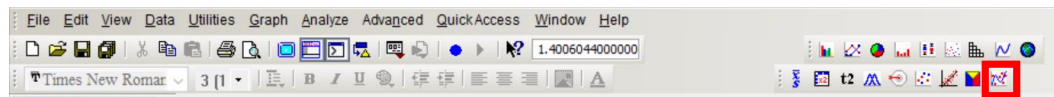


Change the Calibration Type to “Reflectance” from “Radiance”, and select the location and name to save. The cursor value box automatically updates to show the new image. Moving forward, all work done to the image uses the reflectance output file created.

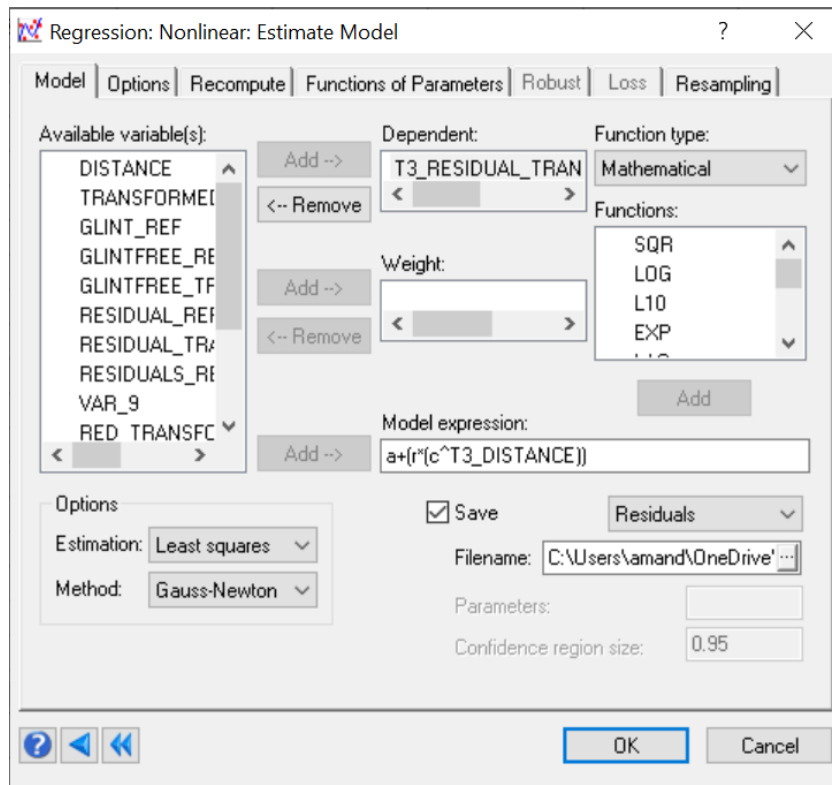
Appendix B

Performing Nonlinear Regression Using Systat

With the necessary distance and transformed y columns pasted into Systat from Excel where they are created, The Regression: Nonlinear: Estimate Model is opened from Systat's quick menu (Outlined by red box).



Once the pop up box opens as follows, the transformed y data is added to the “dependent” box. An initial guess for the model expression is entered into the respective box, adding the distance column into the expression made. To save the residuals, the “Save” box to the left of the drop down menu labeled “Residuals” is selected and a filename and location can be entered below this box.



Click OK, and the estimate model will run. It will then produce a list of information including the number of iterations that were necessary to produce the estimates, R-squared values, best guesses for the parameters input to the “Model expression” box, and a plot of the data with the resulting fit line.

▼ Nonlinear Models

Iteration History

No.	Loss	A	R
0	73.023	-0.101	1.020
1	37.154	-0.650	2.047
2	37.154	-0.650	2.047
3	37.154	-0.650	2.047

Dependent Variable : T3_RESIDUAL_TRANSY
 Zero weights, missing data or estimates reduced degrees of freedom

Sum of Squares and Mean Squares

Source	SS	df	Mean Squares
Regression	56.502	2	28.251
Residual	37.154	198	0.188
Total	93.656	200	
Mean corrected	80.016	199	

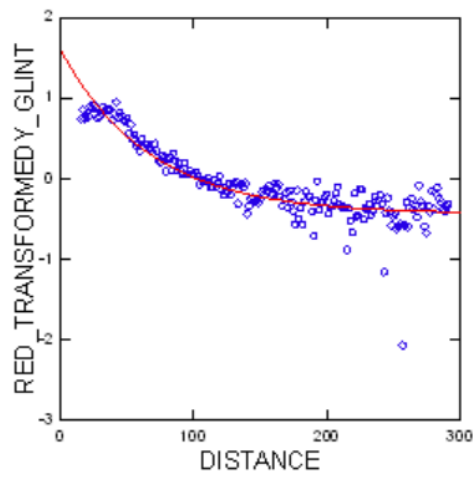
R-squares

Raw R-square (1-Residual/Total) : 0.827
 Mean Corrected R-square (1-Residual/Corrected) : 0.824
 R-square(Observed vs Predicted) : 0.824

Parameter Estimates

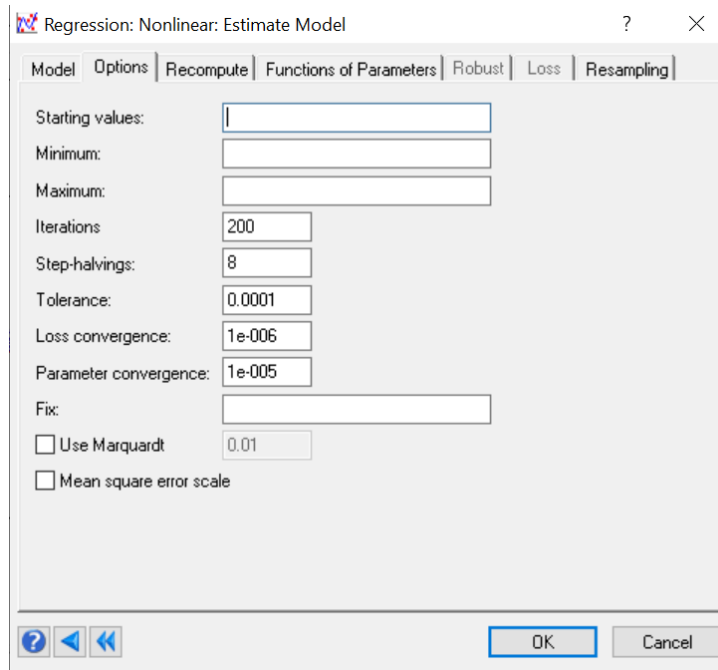
Parameter	Estimate	ASE	Parameter/ASE	Wald 95% Confidence Interval	
				Lower	Upper
A	-0.438	0.018	-23.781	-0.475	-0.402
R	2.054	0.067	30.447	1.921	2.187

Scatter Plot



Residuals have been saved.

Following this, according to the accuracy of the fit, new parameter estimated can be used, new parameters to be estimated can be added, or more iterations can be specified under the options menu as shown below.



Increasing this value will generally lead to a better fit up to a limit.